Probing Magic-Angle Twisted Bilayer Graphene with Monolithic Gate-Defined Josephson Junctions

Jaime Díez Mérida

Supervisor:
Prof. Dr. Dmitri K. Efetov
Co-supervisor:
Prof. Dr. Maciej Lewenstein

ICFO - Institute of Photonic Sciences
UPC - Universitat Politècnica de Catalunya

2024

Table of Contents

List of Figures

Acknowledgments

Abstract

In 2018, following a theoretical prediction from 2011, it was found that stacking two layers of graphene with a relative twist angle of 1.1° between them leads to multiple new properties. At this so-called magic angle, the electronic band structure of the material reconstructs, creating a narrow flat band at the Fermi level. The formation of a flat band enhances electron-electron interactions, resulting in the emergence of distinct states of matter not present in the original graphene layers, including correlated insulators, superconductivity, ferromagnetism and non-trivial topological states. The understanding of the origin of these correlated states could help unravel the physics of highly correlated flat band systems which could potentially provide key technological developments.

The main objective of this thesis is to study magic-angle twisted bilayer graphene (MATBG) by creating monolithic gate-defined Josephson junctions. By exploiting the rich phase space of the material, we can create a Josephson junction by independently tuning the superconductor and the weak link state. Studying the Josephson effect is a first step towards understanding fundamental properties of a superconductor, such as its order parameter.

First, we have optimized the fabrication of these gate-defined junctions made of all van der Waals materials. We have made double-graphite-gated hBN encapsulated MATBG devices where the top gate is split into two parts via nanolithography techniques, in order to independently control the three regions of the Josephson junction (superconductor, weak-link and superconductor). Then, we have studied the gate-defined Josephson junctions via low-temperature transport measurements.

We have observed an unconventional behavior when the weak link of the junction is set close to the correlated insulator at half filling of the hole-side flatband. We have observed a phase shifted Fraunhofer pattern with a pronounced magnetic hysteresis, characteristic of magnetic Josephson junctions. To understand the origin of the signals, we have performed a critical current distribution Fourier analysis as well as a tight binding calculation of a MATBG Josephson junction. Our theoretical calculations with a valley polarized state as the weak link can explain the key signatures observed in the experiment. Lastly, the combination of magnetization and its current-induced magnetization switching has allowed us to realize a programmable zero-field superconducting diode.

Finally, we have shown the flexibility of these devices by studying a MATBG p-n junction under light illumination. We have studied the relaxation dynamics of hot electrons using time and frequency-resolved photovoltage measurements. The measurements have revealed an ultrafast cooling in MATBG compared to Bernal-bilayer at low temperatures, which can be explained by the presence of the mini-Brillouin zone.

In summary, we have demonstrated that by integrating various MATBG states within a single device, we can gain a deeper insight into the system's properties and can engineer innovative, complex hybrid structures, such as magnetic Josephson junctions and superconducting diodes.

Resum

Catalan Abstract

xiv

Resumen

Spanish Abstract

List of publications

J. Díez-Mérida, ... & D. K. Efetov. “Towards a reproducible fabrication of Magic-Angle Twisted Bilayer Graphene devices”. *In preparation.*
Contributions: Sample fabrication, measurements, data analysis, paper writing.

R. Luque-Merino, P. Seifer, D. Calugaru, **J. Díez-Mérida**, A. Diez-Carlon, T. Taniguchi, K. Watanabe, A. B. Bernevig & D. K. Efetov. “Heavy fermion thermoelectricity in magic angle twisted bilayer graphene pn-junctions”. *In preparation.*
Contributions: Sample fabrication, transport measurements.

J. D. Mehew, R. Luque-Merino, H. Ishizuka, A. Block, **J. Díez-Mérida**, A. Díez-Carlón, K. Watanabe, T. Taniguchi, L. S. Levitov, D. K. Efetov & K.-J. Tielrooij. “Ultrafast Umklapp-assisted electron-phonon cooling in magic-angle twisted bilayer graphene”. *Science Advances, Accepted* (2023).
Contributions: Sample fabrication, transport measurements.

S. Y. Yang, A. Díez-Carlón, **J. Díez-Mérida**, A. Jaoui, I. Das, G. Di Battista, R. Luque-Merino, R. Mech & Dmitri K. Efetov. “Plethora of many body ground states in magic angle twisted bilayer graphene”. Low Temp. Phys. 1 49 (6) 631–639 (2023). https://doi.org/10.1063/10.0019420
Contributions: Sample fabrication, measurements and discussion.

J. Díez-Mérida, A. Díez-Carlón, S.Y. Yang, Y.-M. Xie, X.-J. Gao, J. Senior, K. Watanabe, T. Taniguchi, X. Lu, A. P. Higginbotham, K. T. Law & D. K. Efetov. “Symmetry-broken Josephson junctions and superconducting diodes in magic-angle twisted bilayer graphene”. *Nat. Commun.* 14, 2396 (2023). https://doi.org/10.1038/s41467-023-38005-7.
Contributions: Sample fabrication, measurements, data analysis, paper writing.

A. Jaoui, I. Das, G. Di Battista, **J. Díez-Mérida**, X. Lu, K. Watanabe, T. Taniguchi, H. Ishizuka, L. Levitov & D. K. Efetov. “Quantum critical behaviour in magic-angle twisted bilayer graphene”, *Nat. Phys.* 18, 633–638 (2022). https://doi.org/10.1038/s41567-022-01556-5.
Contributions: Sample fabrication.

1 Introduction

The discovery of new materials pushes the boundaries of physics and opens up opportunities for unexpected new technological developments. For the last two decades, so-called 2-dimensional (2D) materials have emerged as a very interesting platform. The idea is simple, take materials which can be thinned down to a single or very few atomic layers and study their properties. Interestingly, many materials experience a drastic change in the properties as the dimensionality is reduced. Furthermore, it is found that when the 2D materials are combined, they not only inherit the properties of the parent materials, but new properties emerge, such that this can act as a relatively simple way to engineer new materials.

One of the most recent approaches to engineer the properties of 2D materials is to change the twist angle between adjacent layers. In this thesis, we will focus on the study of magic-angle twisted bilayer graphene (MATBG), which consists of two layers of graphene rotated by a small angle of $\sim 1.1°$. We will see how by twisting the two graphene layers with respect to each other, the band structure is dramatically changed, giving rise to completely new properties.

In this chapter I will first introduce the development of 2D materials, starting with graphene and continue to explain the field of van der Waals heterostructures, in which different 2D materials are combined. Then, I will focus on twisted bilayer graphene, specifically at the so-called magic-angle. At the end of the chapter I will introduce the objectives and outline of the thesis.

1.1 2D materials and van der Waals heterostructures

In 2004, there was a breakthrough in materials science when Geim and Novoselov used a piece of scotch tape to isolate graphene, a single layer of carbon atoms, by what is now known as mechanical exfoliation [1] (schematized in Fig. 1.1). The discovery had deep physical implications since, for a long time, it was thought that isolated 2D materials could not exist in nature due to thermodynamic instabilities [2]. Furthermore, the newly discovered graphene proved to be very different from its 3-dimensional counterpart, graphite. Not only is the band structure different, with graphite being a metal and graphene a semimetal, but it has different both mechanical and electronic properties. Graphene is one of the strongest materials [3] (with a

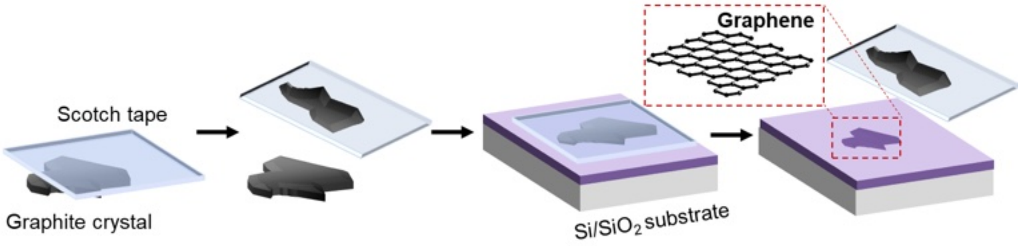

Figure 1.1: Mechanical exfoliation of graphene. A piece of scotch tape is used to isolated the monolayer graphene from the bulk graphite crystal. The exfoliation is generally performed in a Si/SiO$_2$ substrate, although other substrates can also be used.

Young's modulus $E = 1$ TPa), has a high thermal conductivity ($K \approx 5000$ W/mK) [4] and large electron mobilities ($\mu > 10^4$ cm^{2}V^{-1}s^{-1}) enabling the measurement of quantum Hall effect (QHE) at room T [5]. Furthermore, the low excitation energy electrons of graphene, those closest to the Fermi level, behave as massless Dirac fermions. This has direct consequences such as the measured anomalous integer QHE [6, 7] and the fact that graphene electrons exhibit Klein tunneling when subjected to confining potentials [8]. This immunity to localization is responsible for the large mean free paths $l_{mfp} \approx 1$µm [1].

Following the discovery of graphene, the question arose of whether other materials could be exfoliated to obtain their 2D counterpart. The key requirement is that the 3D material is composed of covalently bonded layers which are held together by weak van der Waals (vdW) forces, which enable the layers to be mechanically cleaved, isolating a single or few atomic layers of the material. In 2005, just one year after the discovery of graphene, several other 2D materials were obtained by mechanical cleavage, namely hexagonal boron nitride (hBN), molybdenum disulphide (MoS$_2$),niobium diselenide (NbSe$_2$) and the layered copper oxide Bi$_2$Sr$_2$CaCu$_2$O$_x$ [9]. Since then, many materials have been discovered [10], including many other states of matter found in condensed matter physics such as insulators [11], metals, semiconductors [12], topological insulators [13], superconductors [14] or magnets [15].

What makes the field of 2D materials even richer, is the fact that one can combine these materials relatively freely [10, 16]. The same weak vdW forces which allow 2D materials to be exfoliated are strong enough to keep these materials together if two (or more) of these layers are placed or stacked on top of each other. The first realization of a vdW heterostructure was demonstrated by Dean *et al.* in 2010 [11] when they deposited exfoliated graphene on top of an exfoliated hBN flake. One year later the fabrication techniques had already improved drastically, achieving a fully hBN encapsulated graphene structure [17], and even isolating two graphene layers from each other by using a thin hBN [18]. These works not only pioneered the fabrication of vdW heterostructures but showed how graphene properties improved drastically (achieving $\mu \approx 100,000$ cm^{2}V^{-1}s^{-1} and $l_{mfp} > 3$ µm) by isolating it from the Si/SiO$_2$ substrate typically used for devices. The main reasons why encapsulating improves the quality are that the interfaces between 2D materials self-clean, leading to atomically clean interfaces [19] and that graphene is in this way effectively isolated from the environment. By adding a metallic screening layer below the hBN to fully isolate the graphene from the SiO$_2$ [20] and avoiding contact with chemicals during the fabrication process [21], the properties of encapsulated graphene can even surpass those of suspended graphene [22], achieving $\mu \approx 10^6$ cm^{2}V^{-1}s^{-1} and $l_{mfp} \approx 15$ µm [21]. The evolution of graphene devices from plain exfoliated graphene to hBN encapsulated graphene with a bottom metal gate is shown in Fig. 1.2.

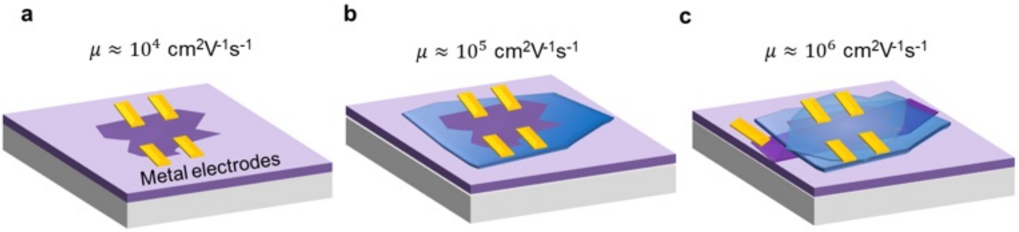

Figure 1.2: Evolution of graphene heterostructure devices. a, Graphene is measured on a Si/SiO$_2$ by using metal electrodes. **b,** The graphene is isolated from the substrate by an hBN flake. The properties are significantly improved. **c,** The graphene is fully encapsulated by hBN and isolated from the substrate by a metal electrode which acts as a global gate. The properties are further improved.

The close proximity between the atoms of the two layers in a vdW heterostructure allows to easily proximitize one material with the properties of another. This has been used for example to induce spin-orbit coupling or superconductivity in graphene by putting it in contact with WS$_2$ [23] or NbSe$_2$ [24], respectively. The fact that any two materials can be combined without having to match their lattice constant, makes the field of vdW materials extremely interesting, serving as the perfect playground to explore the engineering of new materials. As Richard Feynman asked already in

1959 [25]: “What could we do with layered structures with just the right layers? What would the properties of materials be if we could really arrange the atoms the way we want them?”.

1.2 Twistronics: rotating 2D materials

An extra degree of freedom of vdW materials, is the addition of rotation between the layers, which can further modify the properties of the formed heterostructure [26]. When two materials with the same lattice structure are stacked on top of each other, this can lead to the appearance of interference patterns, called moiré patterns. Moiré patterns can emerge when two equal lattices are rotated with respect to each other and/or when the two lattices have different lattice parameters, as shown in Fig. 1.3. The former naturally occurs in graphite, where a defect in the form of a local rotation of a crystal lattice can lead to some layers being rotated w.r.t. each other. The newly created superlattice creates a periodic potential, which can directly influence the band structure, giving rise to van Hove singularities whose position in energy depend on the twist angle [27, 28]. In the case of two rotated graphene layers, the moiré superlattice has a real space wavelength given by:

$$\lambda_M = \frac{a}{2\sin(\theta/2)}, \tag{1.1}$$

where $a = 0.246$ nm is the graphene lattice constant. Another way to engineer band structure with moiré patterns is by combining hBN and graphene. The hBN lattice parameter is 1.8% larger than that of graphene [29], giving rise to a moiré wavelength of:

$$\lambda_M = \frac{(1+\delta)a}{\sqrt{2(1+\delta)(1-\cos\theta)+\delta^2}}, \tag{1.2}$$

where δ is the lattice mismatch and θ the rotation angle between the lattices. In this case, the superlattice moiré potential creates a set of extra Dirac cones with their own set of Landau levels [30]. As the moiré superlattice has a long wavelength ($\sim$14 nm for $\theta = 0$), it allows to perform long sought experiments such as measuring the fractal structure of a Hofstadter butterfly [20, 31, 32]. The improvement of the rotational alignment between the different layers is what eventually led to the discovery of MATBG.

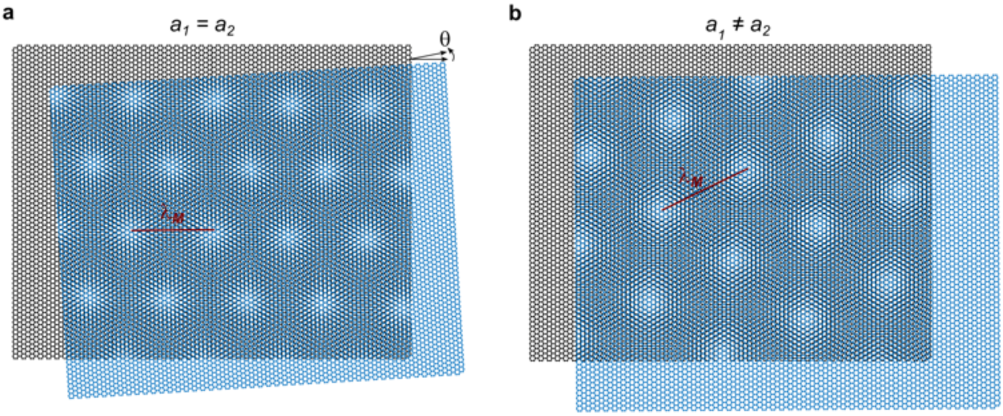

Figure 1.3: Moiré patterns in an hexagonal lattice. a, Both lattices have the same size $a = a_1 = a_2$. A moiré pattern emerges upon rotating the layers. **b,** The lattices have a small lattice mismatch, creating a moiré pattern at $\theta = 0°$.

1.3 Magic-angle twisted bilayer graphene

When two graphene layers are twisted with respect to each other at low angles $\theta < 3°$, their bands hybridize [33] giving rise to a re-normalized velocity given by [34]:

$$v^* = v_0(\frac{1 - 3\alpha^2}{1 + 6\alpha^2}) \tag{1.3}$$

where $v_0 \approx 10^6$ m/s is the Fermi velocity of graphene and α represents the competition between the hybridization of the Dirac cones and the kinetic energy of the electrons. The re-normalized velocity tends to 0 for the so called magic angles θ=1.05°, 0.5°, 0.35°, 0.24° and 0.2° [34] (shown in Fig. 1.4a). Specifically, at the first magic-angle of 1.05° the low energy bands become flat, having a bandwidth of ∼10 meV, with a high density of states (DOS) and being separated from the high energy bands by an energy band gap of ∼50 meV (inset of Fig. 1.4a). The combination of having $v_F \to 0$ and high DOS can lead to having localized electrons with strong electron-electron interactions. Having strong electron-electron interactions can give rise to ordered states of matter such as Mott insulators, ferromagnetism or superconductivity [35, 36, 34]. This possibility makes magic-angle twisted bilayer graphene a very interesting platform to study.

After the original prediction of the magic-angle condition by Bistritzer and MacDonald in 2011 [34], it took several years until the first twisted bilayer graphene below 2° was studied [37]. The main limiting factor was to accu-

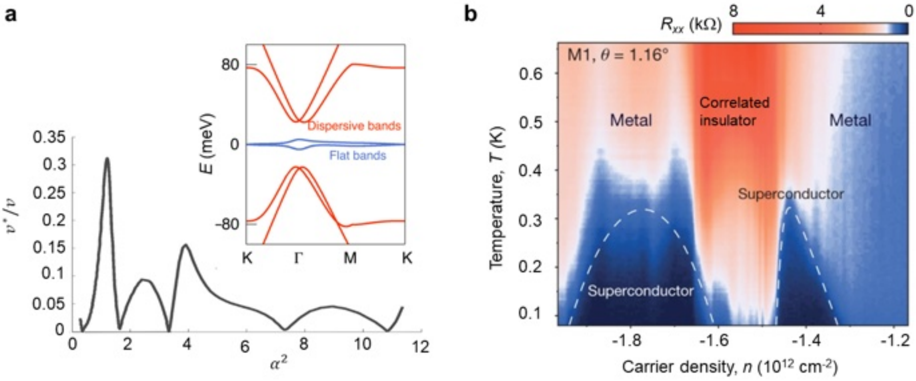

Figure 1.4: MATBG band structure and correlated states. a, Renormalized velocity in MATBG vanishing for certain values of α, which correspond to the magic-angle conditions. Figure is reproduced from [34]. The inset is a calculation of the band structure of MATBG at $\theta \approx 1.05°$, adapted from [41]. **b,** Temperature dependence of a magic angle device $\theta = 1.16°$, showing the appearance of a correlated insulator states and two superconducting domes near half filling of the hole flatband. Figure is adapted from [40]. **c** Measurement of magnetic hysteresis in a device with $\theta \approx 1.17°$ near three-quarter filling of the electron flat band. Adapted from [42]. **d,** Field evolution of Chern insulating states developing from integer fillings of the electron-side flatband. Reproduced from [41].

rately control the stacking of the 2D materials to obtain small angles and clean devices. Advancements in the fabrication techniques [38, 37] finally led to the observation of correlated states in MATBG in 2018 by Cao *et al.* [39, 40]. The first exciting finding was the appearance of insulating states not predicted by theory (correlated insulators) at half filling of both the electron and hole side of the moiré band [39]. The second, and most important finding, was the presence of superconductivity next to the correlated insulating states [40], shown in Fig. 1.4b. The revolutionary discovery of this work is the fact that superconductivity could be achieved in a non-superconducting system just by changing the relative alignment between the neighboring layers.

Following this discovery, it was found that the system was even richer, including correlated insulators [39, 43, 44, 45, 46, 47] and superconductors [40, 43, 44, 45, 48, 49] at different fillings of the band, showing orbital magnetism (OM) [50, 44] even leading to quantized anomalous Hall effect [51], interaction induced correlated Chern insulators (CCI) [52, 53, 54, 41] and strange metal phases [55, 56, 57]. The beauty of MATBG is that all these phases are found within the same flat band and they can be tuned between each other by changing the Fermi energy by a few meV. From an experimental point of view, this means that they can be all be accessed by using gate electrodes to dope the MATBG to different filling factors of the bands.

The rich phase space of MATBG and its wide gate tunability led to the **research question** at the start of this thesis: can we use gate voltages to combine these different phases into a single device? In particular, we are interested in creating a Josephson junction (JJ), a device in which two superconducting materials are connected via a weak link or non-superconducting state [58]. Creating a JJ would be a definite proof of the superconducting phase coherence in MATBG and an essential step towards understanding its origin, which is still one of the main questions in the field [59]. Additionally, the JJs in MATBG could also be used to probe the other states found within the flat band. JJs are extremely sensitive probes, such that they can be useful to study the non-trivial states found in MATBG. Combining superconductors with other states, such as magnets or non-trivial topological states, can lead to the formation of exotic phases, which can give rise to spin-triplet supercurrents [60, 61, 62], magnetic π junctions [63, 64, 65] or topologically non-trivial 4π junctions [66, 67, 68]. These exotic JJs can have applications in superconducting spintronics [69] or quantum computing [70]. One major difficulty in the creation of these complex JJs lies in the engineering of ultra-clean interfaces between the different materials, which is needed for an efficient coupling between the different phases. This could be solved in the case of MATBG, since all the states of the JJ can be obtained within the same material using gate electrodes to define the different regions of the junction.

Therefore, the **main objective** of this thesis is to develop gate-defined JJs in MATBG to study the correlated physics of the flatband. The first aim is to develop and optimize the fabrication steps required to create the gate-defined JJs. The second aim is to study the behavior of the gate-defined JJs by means of low T transport techniques. The device architecture to achieve the gate-defined junctions consists of a double-graphite-gated hBN encapsulated MATBG device as shown in Fig. 1.5a. By splitting the top graphite gate in two, we can effectively tune the region inside the junction (affected only by the back gate) independently from the region outside the junction (controlled by both the top and bottom gates) as shown in Fig. 1.5b. By setting the outer region into the SC state and changing the carrier density in the junction region we can create a JJ, as schematically displayed in the inset of Fig. 1.5a.

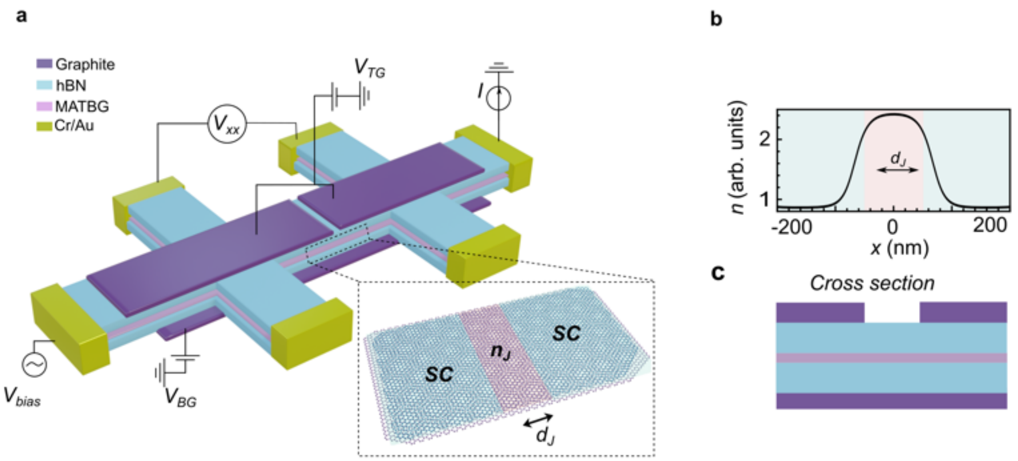

Figure 1.5: Gate-defined JJ architecture in MATBG a, Double-graphite-gated hBN encapsulated MATBG Hall bar, in which the graphite top gate is split in two. (Inset) Schematic of the MATBG forming a JJ: being superconducting (SC) on the sides while having a different carrier density (n_J) in the weak link area. **b,** (Top) Carrier density profile corresponding to having a different carrier density inside and outside the junction area. d_J corresponds to the size of the junction. (Bottom) Cross section around the junction area.

1.4 Outline of the thesis

In this introductory chapter we have introduced the state-of-the-art of the MATBG field and the main concepts that will be mentioned throughout the thesis. We have finished stating the main objective of the thesis.

In Ch. 2 we introduce the main theoretical concepts used in the thesis: introducing the band structure of MATBG, discussing the main physics of JJs and focusing on their behavior under magnetic fields.

In Ch. 3 we introduce all the methods used in the thesis, namely sample fabrication and electrical measurements at low T. In the fabrication section we discuss all the details needed to create high quality MATBG devices and how these can be shaped to create a JJ.

In Ch. 4 we discuss the optimization process which was done in order to successfully create the JJs. Due to the complexity of the system, several parameters need to be taken into account to ensure a successful fabrication process.

In Ch. 5 we show the measurements performed to characterize the fabricated gate-defined JJs. This starts by characterizing the superconducting state of MATBG, then detailing how the gate electrodes are used to create the junction and finally proving the appearance of a JJ by measuring their Fraunhofer patterns [71].

In Ch. 6 we focus on the measurements of the JJ when the weak link is set close to the CI at half-filling of the hole band. We show how this JJ breaks both inversion and time reversal symmetry, leading to the creation of a magnetic JJ and a superconducting diode. We discuss the possible origins of the measured unconventional JJ. We show how most of the signals can be explained by considering the state at $\nu = -2$ to be a valley polarized state with Chern number $C = -2$ [71].

Ch. 7 shows how the same devices used to create JJs can be used to create a gate-defined pn-junction. After characterizing the pn-junctions in transport, we probe the junction under light illumination to study the cooling dynamics of the electrons. We show how electrons in devices close to magic-angle have very fast cooling dynamics at low T when compared to Bernal bilayer graphene [72].

Finally, Ch. 8 gives the main conclusions found in the thesis. It also discusses possible directions of research following the results found in this thesis and the current state of the MATBG field.

2 Theoretical Background

In this chapter we introduce the basic theoretical concepts which will be used throughout the thesis. The main parts are the understanding of twisted bilayer graphene, specifically at the magic angle, and the basic theory of Josephson junctions. However, in order to properly introduce magic-angle graphene, we will build from its basic components: graphene and bilayer graphene.

2.1 Graphene

Graphene is a monolayer of carbon atoms organized in a honeycomb lattice. It was first discovered by Novoselov and Geim *et al.* in 2004 by mechanical exfoliation of a graphite crystal [1] and has since then widely studied in all areas of science [73]. The theoretical study of graphene dates back to 1947, when Wallace first studied its band structure [74]. Graphite contains four valence electrons in the $2s$ and $2p$ orbitals, which in the graphene configuration, organize having 3 electrons in a sp^2 hybridization leaving one free p electron. The three hybridized electrons, form covalent σ bonds in plane and do not contribute to the conductivity. The final $2p_z$ electron forms weaker π bonds out-of-plane and is the one that contributes to the conductivity. Therefore, the band structure is calculated only taking into account this $2p_z$ electron.

The honeycomb hexagonal lattice contains two inequivalent atoms A and B, which translates to the fact that the structure can be studied as two triangular lattices with two atoms per unit cell, and lattice vectors $\boldsymbol{a_1}$ and $\boldsymbol{a_2}$ (see Fig. 2.1):

$$\boldsymbol{a_1} = \frac{a}{2}(3, \sqrt{3}), \; \boldsymbol{a_2} = \frac{a}{2}(3, -\sqrt{3}), \tag{2.1}$$

.

with the reciprocal lattice vectors defined by $\boldsymbol{a_i} \cdot \boldsymbol{b_j} = 2\pi\delta_{ij}$ (δ_{ij} refers to the Kronecker delta while $\boldsymbol{\delta_i}$ represents the lattice vectors of graphene). Each atom has three nearest neighbors, which form part of the other sublattice, such that an A atom is surrounded by 3 B atoms and vice versa, which are separated in real space by the vectors:

$$\boldsymbol{\delta_1} = \frac{a}{2}(1, \sqrt{3}), \; \boldsymbol{\delta_2} = \frac{a}{2}(1, -\sqrt{3}), \; \boldsymbol{\delta_3} = -a(1, 0), \tag{2.2}$$

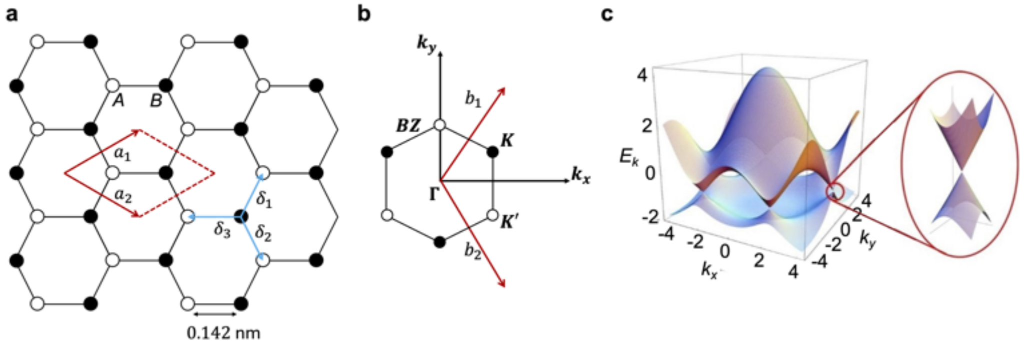

Figure 2.1: Graphene lattice and band structure. **a,** Real space graphene honeycomb lattice, where A and B denote the two inequivalent atoms. **b,** Reciprocal space lattice, showing the K and K' points in the 1st Brillouin zone. **c,** Graphene´s band structure, also with a close up near the K point, showing the linear dispersion. Fig. **c** is adapted from [75].

.

The corners of the Brillouin zone K and K' are what we call the Dirac points (the reason for this is explained below) and are given by reciprocal lattice coordinates:

$$\boldsymbol{K} = (\frac{2\pi}{3a}, \frac{2\pi}{3\sqrt{3}a}),\ \boldsymbol{K'} = (\frac{2\pi}{3a}, -\frac{2\pi}{3\sqrt{3}a}), \tag{2.3}$$

The tight binding Hamiltonian for graphene, considering only the nearest neighbor hopping is [75]:

$$\hat{H} = -\,t \sum_{<i,j>,\sigma} (a^\dagger_{\sigma,i} b_{\sigma,j} + H.c.). \tag{2.4}$$

Where $a^\dagger_{\sigma,j}, a_{\sigma,j} (b^\dagger_{\sigma,j}, b_{\sigma,j})$ create/annihilate an electron of sublattice A (B), on site $\boldsymbol{R}_j$ with spin $\sigma =\uparrow, \downarrow$ and $H.c.$ the hermitian conjugate. The nearest neighbor ($A-B$) hopping given by the overlap of the π orbital is $t \approx 2.8$ eV, while the next nearest neighbor ($A-A$) hopping value is not exactly known, and, in many cases, can be neglected [76]. We can write the Hamiltonian in reciprocal space by applying the Fourier transform:

$$a^\dagger_i = \frac{1}{\sqrt{N}} \sum_{\boldsymbol{k}} e^{i\boldsymbol{k}\cdot r_i} a^\dagger_{\boldsymbol{k}},\ b^\dagger_j = \frac{1}{\sqrt{N}} \sum_{\boldsymbol{k}} e^{i\boldsymbol{k}\cdot r_j} b^\dagger_{\boldsymbol{k}}, \tag{2.5}$$

where N is the number of A and/or B sites. The Hamiltonian is then written (ignoring the spin, taking it as a degeneracy of the system):

$$\hat{H}(\boldsymbol{k}) = -t\sum_{\boldsymbol{k},\delta_j}(e^{-i\boldsymbol{k}\cdot\boldsymbol{\delta}}a^\dagger_{\boldsymbol{k}}b_{\boldsymbol{k}} + H.c.), \tag{2.6}$$

where $\sum_\delta$ sums over the nearest-neighbor vectors $\boldsymbol{\delta_1}$, $\boldsymbol{\delta_2}$ and $\boldsymbol{\delta_3}$.

The Hamiltonian can then be represented in matrix form as:

$$\begin{gathered}\hat{H}(\boldsymbol{k}) = \sum_{\boldsymbol{k}} \boldsymbol{\Psi}^\dagger h(\boldsymbol{k})\boldsymbol{\Psi}, \\ \text{having } \boldsymbol{\Psi} = \begin{pmatrix} a_{\boldsymbol{k}} \\ b_{\boldsymbol{k}} \end{pmatrix},\ h(\boldsymbol{k}) = -t\begin{pmatrix} 0 & \Delta_{\boldsymbol{k}} \\ \Delta^*_{\boldsymbol{k}} & 0 \end{pmatrix} \text{ and } \Delta_{\boldsymbol{k}} = \sum_\delta e^{i\boldsymbol{k}\cdot\delta},\end{gathered} \tag{2.7}$$

having eigenvalues [74]:

$$\begin{gathered}E_\pm(\boldsymbol{k}) = \pm t\sqrt{3 + f(\boldsymbol{k})}), \\ \text{with } f(\boldsymbol{k}) = 2\cos\Big(\sqrt{3}k_y a\Big) + 4\cos\left(\frac{\sqrt{3}}{2}k_y a\right)\cos\Big(\frac{3}{2}k_x a\Big).\end{gathered} \tag{2.8}$$

The equation shows how the spectrum has electron-hole symmetry and the bands touch at the Dirac points $\boldsymbol{K}$ and $\boldsymbol{K'}$ (see Fig. 2.1c). It is interesting then, to solve the band structure at small momentum $\boldsymbol{q}$ relative to the Dirac points such that $\boldsymbol{k} = \boldsymbol{K} + \boldsymbol{q}$, with $|\boldsymbol{q}| << |\boldsymbol{K}|$. In this case $\Delta_{\boldsymbol{k}} = \Delta_{\boldsymbol{K}+\boldsymbol{q}}$, which leads to:

$$h(\boldsymbol{K} + \boldsymbol{q}) = \hbar v_F \begin{pmatrix} 0 & q_x + iq_y \\ q_x - iq_y & 0 \end{pmatrix} = \hbar v_F \boldsymbol{q}\cdot\boldsymbol{\sigma}, \tag{2.9}$$

with $v_F = -t\frac{3a}{2} = 10^6$ m/s the Fermi velocity and $\boldsymbol{\sigma} = (\sigma_x, \sigma_y)$ the vector Pauli matrices. This is simply the equation for massless Dirac fermions, with the key difference that the spinor corresponds to the valley pseudospin of graphene, instead of a real spin. This pseudospin, generally referred to as valley, comes from the presence of the two inequivalent A and B points in the graphene lattice. The valley pseudospin quantum number adds an extra chirality to the system (on top of spin). Considering both spin and valley means that graphene bands are 4-fold degenerate unless a symmetry of the system is lifted. Finally, solving the Dirac Hamiltonian leads to graphene's linear dispersion at the Dirac points:

$$E_{\pm}(\boldsymbol{q}) = \pm\hbar v_F|\boldsymbol{q}|. \tag{2.10}$$

A key concept of the graphene Hamiltonian and which will become important when explaining TBG, is the role of inversion and time reversal symmetry. In general, intervalley hopping in graphene is negligible [75], such that one can consider the Hamiltonian in just one valley (as solved above around the K valley), and take the other valley as a degeneracy. These two valleys are related both by inversion C_2 symmetry $(x, y) \to (-x, -y)$ and time reversal $\mathcal{T}$ operator (which conjugates the Hamiltonian). However, when looking inside one Dirac cone, i.e. $k = K + q$, these symmetries cannot be taken individually and the Hamiltonian is invariant under the combined $C_2\mathcal{T}$ operation, which takes it into itself. A consequence of the $C_2\mathcal{T}$ symmetry is that as long as this symmetry is not broken, the Dirac cones are not gapped. However, a broken C_2 or $\mathcal{T}$ symmetry will gap the Dirac cone. Inversion symmetry is for example broken by having two different atoms in the $A - B$ sites, (which explains the band gaps of hBN or of TMDs), while time reversal symmetry can be broken by external magnetic fields [77]. These symmetries play an important role in the band structure of MATBG, as is explained below.

2.2 Bilayer graphene

Bilayer graphene is formed when two carbon monolayers are stacked on top of each other. It appears naturally in an AB or Bernal configuration, in which the second layer is displaced from the first layer such that its B atoms (B_2, where the 2 signals the second layer) are placed at the center of the first layer's hexagon while its A atoms (A_2) lie directly on top of the B atoms of the bottom layer (B_1) (see Fig. 2.2a). This configuration has a high interlayer hopping component for $A_2 - B_1$ sites given by $\gamma_{A2B1} = \gamma_1 = t_\perp \approx 0.4eV$, while the weaker interlayer hoppings $\gamma_{A1B2} = \gamma_3$ and $\gamma_{A1A2} = \gamma_{B1B2} = \gamma_4$ can be ignored [75]. We can then easily extend the tight binding Hamiltonian of graphene to account for the second layer, by adding the new layer elements [75, 78]:

$$\begin{aligned}\hat{H} =& - t \sum_{<i,j>\sigma} (a^{\dagger}_{(1,i,\sigma)} b_{(1,j,\sigma)} + H.c.)\\ &- t \sum_{<i,j>\sigma} (a^{\dagger}_{(2,i,\sigma)} b_{(2,j,\sigma)} + H.c.)\\ &- t_{\perp} \sum_{i,\sigma} (a^{\dagger}_{(2,i,\sigma)} b_{(1,i,\sigma)} + H.c.),\end{aligned} \tag{2.11}$$

where $a_{m,i,\sigma}(b_{m,i,\sigma})$ annihilates an electron with spin σ, in layer $m = 1, 2$ on sublattice $A(B)$ at site $\boldsymbol{R}_i$, such that the first two terms describe each individual layer and the third term describes the interlayer hopping. If we repeat the procedure used for graphene, we can write the Hamiltonian in the low-momentum approximation $\boldsymbol{k} = \boldsymbol{K} + \boldsymbol{q}$ as:

$$\hat{H} = \sum_{\boldsymbol{k}} \boldsymbol{\Psi}^{\dagger} h(\boldsymbol{k}) \boldsymbol{\Psi}; \text{ now having } \boldsymbol{\Psi} = \begin{pmatrix} a_{1,\boldsymbol{k}} \\ b_{1,\boldsymbol{k}} \\ a_{2,\boldsymbol{k}} \\ b_{2,\boldsymbol{k}} \end{pmatrix} \text{ and}$$

$$h(\boldsymbol{K}+\boldsymbol{q}) = \begin{pmatrix} -V & \hbar v_F(q_x + iq_y) & 0 & 0 \\ \hbar v_F(q_x - iq_y) & -V & -t_{\perp} & 0 \\ 0 & -t_{\perp} & V & \hbar v_F(q_x + iq_y) \\ 0 & 0 & \hbar v_F(q_x - iq_y) & V \end{pmatrix}, \tag{2.12}$$

where $V = (V_1 - V_2)/2$ is the difference in the electrochemical potential between the two layers. The energy eigenvalues are then given by:

$$E^2_{\pm}(\boldsymbol{q}) = V^2 + \hbar^2 v_F^2 q^2 + t_{\perp}^2/2 \pm \sqrt{4V^2 \hbar_2 v_F^2 q^2 + t_{\perp}^2 \hbar^2 v_F^2 q^2 + t_{\perp}^4/4}. \tag{2.13}$$

When the two layers are in equilibrium ($V = 0$) bilayer graphene is a semimetal with parabolic bands. However, different to graphene, a gap can be opened upon the application of a perpendicular electric field, generally referred to as displacement field. The displacement field breaks the inversion symmetry between the layers by modifying their respective electrochemical potentials. The ability to open up a gap with an electric field [79], combined with the valley and spin degrees of freedom makes bilayer graphene very attractive to some applications, such as for creating quantum dots which can be used as spin qubits [80].

2.3 Twisted bilayer graphene

After having visited the lattices and band structure of monolayer and bilayer graphene, we can now move to the case of twisted bilayer graphene, in which the top layer is rotated w.r.t. to the original Bernal configuration by a certain angle θ. Before studying the band structure of the system, it is convenient to explain the physics of moiré patterns in an hexagonal lattice.

2.3.1 Understanding moiré patterns

2.3.1.1 Moiré patterns in real space. We consider two graphene lattices with primitive vectors $\boldsymbol{a_1}^{(1)}$, $\boldsymbol{a_2}^{(1)}$, $\boldsymbol{a_1}^{(2)}$ and $\boldsymbol{a_2}^{(2)}$, where the super index indicates the layer. We then assume that the second layer rotates over the 1st layer, such that when $\theta = 0$, $\boldsymbol{a_{1,2}}^{(1)} = \boldsymbol{a_{1,2}}^{(2)}$ (Fig. 2.2a). Then as the second layer rotates, one can generally write $\boldsymbol{a_{1,2}}^{(2)}$ considering the rotation matrix in 2D $\boldsymbol{R}(\theta)$, such that:

$$\boldsymbol{a_{1,2}}^{(2)}(\theta) = \boldsymbol{R}(\theta) \cdot \boldsymbol{a_{1,2}}^{(2)} \quad \text{with} \quad \boldsymbol{R}(\theta) = \begin{pmatrix} \cos(\theta) & -\sin(\theta) \\ \sin(\theta) & \cos(\theta). \end{pmatrix} \tag{2.14}$$

As the layers are rotated, it is important to understand the difference between commensurate and incommensurate rotations, since a properly defined superlattice will only exist for commensurate rotations. Although it is found that for very small angles (the ones we are interested in), this distinction losses its importance as all angles have well defined band structures in the continuum model [81, 82], it is important to understand the concept. A commensurate rotation is that in which there is translational symmetry in the superlattice, such that an $A_2 - B_1$ site is found at any other position in the superlattice primitive cell [83], as shown in Fig. 2.2b. This means that there exists a superlattice vector ($\boldsymbol{L}$) which brings a point in the structure onto itself such that:

$$L_1 = n\boldsymbol{a_1}^{(1)} + m\boldsymbol{a_2}^{(1)} = p\boldsymbol{a_1}^{(2)} + q\boldsymbol{a_2}^{(2)}, \tag{2.15}$$

with $n, m, p, q = 0, 1, 2...$ L_2 is obtained by rotating L_1 by $\pi/3$. In the case of the graphene lattice it can be proven that the condition is fulfilled for $n = q$ and $m = p$ leading to the condition for commensurability: [84]:

$$\cos(\theta) = \frac{n^2 + 4nm + m^2}{2(n^2 + nm + m^2)}, \tag{2.16}$$

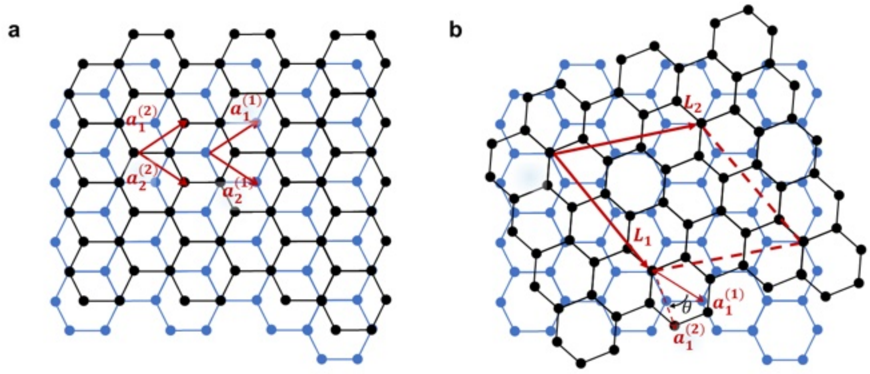

Figure 2.2: Twisting bilayer graphene. a, Two graphene sheets in an AB-Bernal configuration, showing the lattice vectors of each layer. **b,** The top graphene layer is rotated by an angle θ, showing a commensurate rotation. The new superlattice vectors are defined by L_1 and L_2, which take an A_2B_1 position onto itself.

In general we focus on structures given by $|m-n|=1$, in which there is one moiré pattern per unit cell, and are therefore the most fundamental structures [85]. In that case we obtain the simplified equations [33]:

$$\cos(\theta)=\frac{3n^2+3n+1/2}{3n^2+3n+1} \text{ and } L_1=n\boldsymbol{a_1}+(n+1)\boldsymbol{a_2}, \tag{2.17}$$

where n is now a general integer and $\lambda_M=|\boldsymbol{L}|$. The area ($A_s$) and number of atoms per moiré unit cell (N) is given by [86]:

$$\begin{gathered} A_s=\frac{\sqrt{3}}{2}\lambda_M^2=\frac{\sqrt{3}}{8}\frac{a^2}{\sin^2(\theta/2)}, \\ N=4(3n^2+3n+1). \end{gathered} \tag{2.18}$$

As the moiré area increases with decreasing twist angle, it is clear how for small twist angles the number of atoms per moiré unit area increases enormously. Indeed, for angles around the magic angle condition ($\theta\approx 1.1°$, $n\approx 30$), $N\sim 10^4$ atoms. This very large number of atoms per unit cell (exemplified in Fig. 2.3a), compared to monolayer and Bernal bilayer graphene , makes the calculations with tight binding very computationally demanding. A simplified description at low energies and low momentum values is the continuum model [33, 34], which is the main focus of the the following section.

2.3.1.2 Moiré patterns in $k-$space It is convenient to also look at the reciprocal space representation of the moiré pattern. When the two real space lattices are rotated, the reciprocal lattices will also rotate (see Fig. 2.3b). If we consider the rotation to happen around the Γ point, we see how the moiré wave vector will be given by the difference in position between the K points of the original lattices, such that:

$$k_\theta = 2\sin(\theta/2)k_D, \tag{2.19}$$

where $k_D = 4\pi/3a$ is the magnitude of the Dirac point wavevector. Using k_θ we can define a new mini-Brillouin superlattice, which corresponds to the moiré superlattice in real space. As there will be one superlattice created for K and K' points of the original lattices, the valley degeneracy of graphene is also inherited by the twisted bilayer system. Although the superlattice K_s points, are a combination of K and K' points of opposite layers, the valley is preserved due to the large momentum difference between these points in the original graphene Brillouin zone [37]. Considering then the 4-fold degeneracy, the carrier density needed to have a full mini-Brillouin zone is the superlattice carrier density:

$$n_s = 4/A_s = 4\frac{8\sin^2(\theta/2)}{\sqrt{3}a^2} \approx \frac{8\theta^2}{\sqrt{3}a} \text{ for small } \theta, \tag{2.20}$$

where A_s is the unit cell area and the four comes from the 4-fold degeneracy of valley and spin. This relation can be used to extract the twist angle of the experimental samples as is explained later in Ch. 3.

2.3.2 Flat bands in MATBG

We now turn to the band structure description of MATBG. Due to the large number of atoms present in the moiré super cell, the tight binding Hamiltonian becomes very computationally demanding as the angle gets reduced. As we are interested in studying the conditions at very low angles $\theta \approx 1.1°$, we will focus on the continuum description of the Hamiltonian [33]. Furthermore, the continuum model can be used to predict the presence of flatbands at the magic angle conditions [34, 86]. Due to the complexity of the system in this section we will not write the derivation of the Hamiltonian, but just comment on the main aspects that it entails.

The initial point of the continuum model is to consider the TBG band spectrum as two sets of monolayer Dirac cones which rotate around the Γ point (as in Fig. 2.3c). As just explained, this rotation creates a moiré superlattice

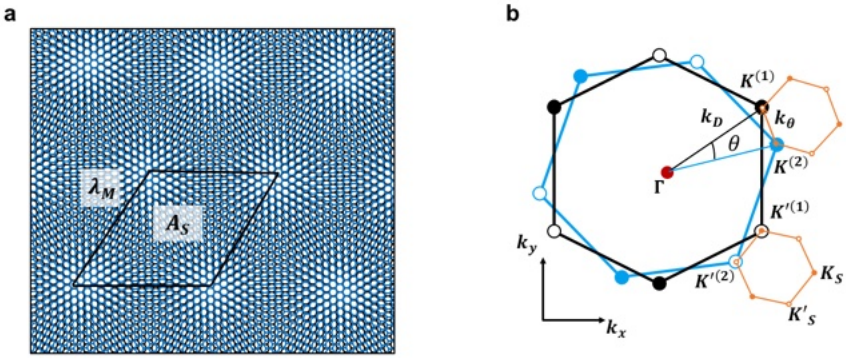

Figure 2.3: MATBG moiré pattern and mini-Brillouin zone. a, Commensurate structure showing the moiré pattern in real space with moiré wavelength λ_M. From the figure it is already clear the large amount of atoms which sit inside one moiré lattice (even though this is a much larger angle than 1.1°). **c,** Reciprocal space representation of the moiré pattern, dictated by the moiré wavevector k_θ. The figure is inspired by [37].

with wavelength λ_M and wavevector k_θ. As the layers rotate, the cones at each valley, $K_1 - K_2$ and $K_1' - K_2'$ hybridize, such that the Hamiltonian can be expressed as the sum of two intralayer terms H_1 and H_2 and an interlayer hopping term H_T. The important parameter to consider during the twisting is the evolution of the hopping term H_T. Interestingly, it is found [34] that the bands of the moiré graphene depend mostly on a single factor:

$$\alpha = \frac{w}{\hbar v_F k_\theta}, \tag{2.21}$$

where w is the hopping energy between the layers and k_θ is the already mentioned moiré wavevector. The parameter α can be understood as a parameter showing the competition between the hybridization of the Dirac cones, expressed with w, and the kinetic energy of the electrons, expressed by $\hbar v_F k_\theta$. As $k_D \propto \theta$, we can expect that as the angle becomes smaller, the bands not only hybridize further as the tunneling probability increases (the Dirac cones are closer together), but the kinetic energy also decreases (k_θ becomes smaller). As this happens, the Fermi velocity is strongly renormalized [34]:

$$v^* = v_0 \frac{1 - 3\alpha^2}{1 + \alpha^2}, \tag{2.22}$$

with v_0 the Fermi velocity of graphene. Following this relation we see how for large twist angles, α is small and the low-energy dispersion of the the twisted graphene is barely affected. However, as the twist angles get reduced, α increases and the Fermi velocity is heavily renormalized (see Fig. 2.4). In particular, for certain α values, the renormalized Fermi velocity vanishes ($v^* \to 0$). These values correspond to the so-called magic-angles. As α increases from 0, the first magic-angle condition is found for $\alpha = 1/\sqrt{3}$, which gives the first magic-angle value of:

$$\theta = \arcsin\left(\frac{\sqrt{3}w}{\hbar v_0 k_D}\right) \cdot 2 \approx 1.1^\circ. \tag{2.23}$$

Most interestingly, the Fermi velocity renormalization is accompanied by the flattening of the bands, such that at the first magic-angle $\theta \approx 1.1^\circ$, the low energy bands sit a few meV around the Fermi energy [39]. The flattening of the band is accompanied by several key points: 1. The density of states in the flat band is enhanced due to the appearance of van Hove singularities (VHS) with the twist angle. As the angle gets reduced and the band gets flatter the VHSs come closer together making the density of states peak around the flat band energy range [28, 87]. 2. At the same time, a gap is opened around the Γ_S point, near the intersection of the two Dirac cones, due to the band hybridization (transition from Fig. 2.4b and c), such that the low energy flat bands are isolated from the higher energy dispersive bands by a band gap of ~ 50 meV [37]. 3. The interactions do not gap out the Dirac points at the K and K' points. This way the band structure of MATBG consists (generally speaking) of a 4-fold degenerate flatband, separated by an energy gap from the higher dispersive bands (as shown in Fig. 2.5a). 4. Each flat band (4 for electron and 4 for hole side) of MATBG is characterized by a Chern number of $C = \pm 1$ [88, 89]. The Chern numbers will be relevant when the $C_2\mathcal{T}$ symmetry is broken, such as breaking C_2 symmetry when aligning to hBN [51, 50] or breaking $\mathcal{T}$ by applying magnetic fields or, most interestingly, when strong interactions are present [52]. The latter will play a key role in MATBG as it allows to stabilize Chern insulating phases even at zero magnetic fields [50, 90]. As breaking C_2 or $\mathcal{T}$ have a different effect on the Chern numbers at each valley, it is possible (in some cases) to infer which symmetry is broken from the measured Chern number (see Fig. 2.5b, d.)

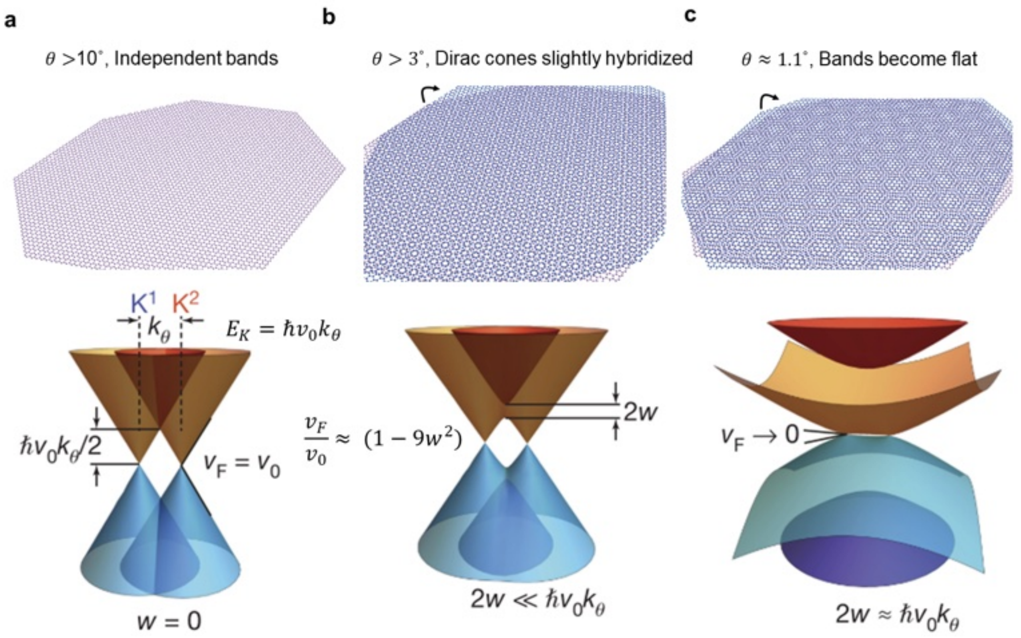

Figure 2.4: Flat band formation with twist angle. a, The twist angle between the layers is high. The material behaves as two independent graphene sheets. **b,** As the angle gets reduced 3°$< \theta < 10$°, the bands start to hybridize. The correction to the Fermi velocity is still small. **c,** At the magic-angle condition $\theta \approx 1.1$° the strong hybridization makes the bands flat and $v_F \to 0$. The bottom panel of the figure is adapted from [39].

It is interesting to look at the internal structure of the flat band and what happens as it is filled (or emptied) from CNP towards the flat band edge. A relevant concept is the filling factor of the flat band ν, which represents the number of electrons per moiré lattice, such that the flat band is full/empty for $\nu = \pm 4$. In principle the band structure is 4-fold degenerate such that the 4 bands should be filled simultaneously. However, as the carrier density reaches integer filling factors of the flatband, that is, every time $\nu = \pm 1, 2, 3$ electrons per moiré unit cell, the bands undergo a transition which breaks the degeneracy. This behavior was observed via STM [47], local compressibility [46] and capacitance [91] measurements, pointing to the appearance of broken flavor symmetry states at every integer filling of the flat band. Here, flavor is used as an umbrella term including both spin and valley degrees of freedom. When the band is empty $\nu = 0$ (CNP), initially all the bands are filled simultaneously showing a 4-fold degenerate Dirac-like behavior. However, every time time an integer filling is being reached, there is a symmetry breaking transition in which one band gets filled while the

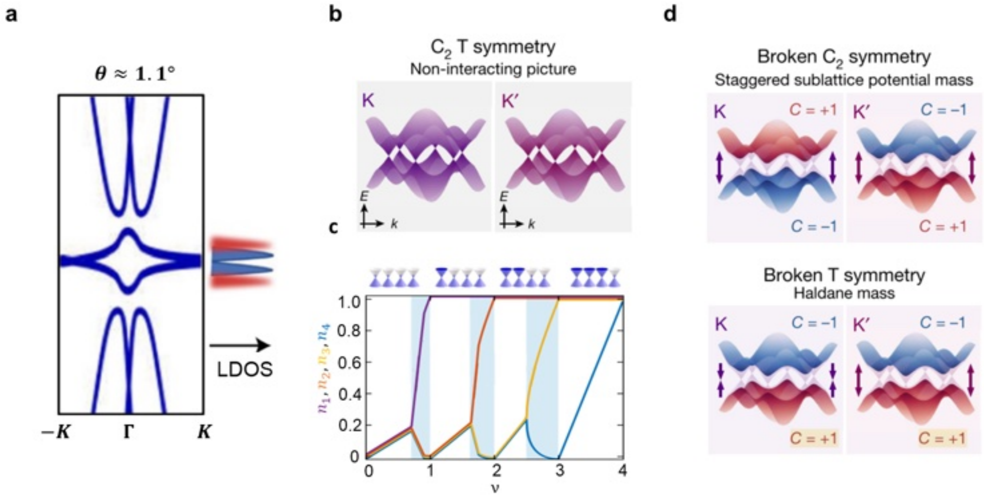

Figure 2.5: Band structure of MATBG and its broken symmetries. **a,** MATBG band structure schematic and its corresponding DOS showing the VHS peaks. **b,** Schematic of non-interacting band structure of MATBG, showing the 4-fold band degeneracy for the hole and electron band. **c,** Schematic showing the flavor breaking as the band is filled, showing the density of individual flavors $n_i (i = 1, 2, 3, 4)$ vs. band filling ν. **d,** Schematic showing the two possible scenarios of $C_2\mathcal{T}$ symmetry breaking and their different Chern numbers in each valley. The vertical arrows signal the sign of the opened mass gap, being the same for the C_2-breaking case and opposite for the $\mathcal{T}$-breaking case. The bands preserve their spin degeneracy in this picture. Figure is adapted combining **a** from [87], **b** and **d** from [52] and **c** from [46].

other three bands empty themselves. This behavior is repeated every time an integer ν is reached until all the bands are filled (see Fig. 2.5c). These transitions should change the degeneracy at different fillings, corresponding to 4, 3, 2, 1 at fillings ν =0, 1, 2 and 3. Such behavior is indeed measured when breaking time-reversal symmetry by applying a magnetic field and measuring the Landau fan, where there is a Chern number (C) correspondence with ν following $(C, \nu) \rightarrow (\pm 4, 0), (\pm 3, \pm 1), (\pm 2, \pm 2)$ and $(\pm 1, \pm 3)$ [91, 52, 54, 41]. This symmetry breaking is accompanied by spin/valley polarizations, as these are the broken degeneracies. However, the developed spin/valley texture depends on many factors, such as interaction strength, angle, etc. such that one cannot know a priori the formed state.

2.4 Superconductivity and Josephson junctions

Superconductors are materials that exhibit zero resistance when cooled down below a critical temperature T_c, such that an electrical current can flow in them with no electrical resistance [58]. Since its discovery in mercury in 1911 by Onnes and collaborators, it has been a great topic of research due to its potential high impact in technology. The zero-resistance state of superconductors lead to perfect diamagnetism when exposed to magnetic fields, as a current opposing the field can be spontaneously generated with no energy cost. So-called type-I superconductors expel the field this way until superconductivity is lost at a critical field H_c. At the value of H_c, the SC is not able to create a strong enough current to screen it. The maximum current that the SC can create before turning normal is the critical current I_c. Other superconducting materials (type-II SC) screen the field below a critical field H_{c1} but, as the field increases further, they allow field lines to penetrate in the material in the form of vortices, making part of the material normal (inside the vortex). Each vortex encloses a flux $\Phi_0 = \frac{h^2}{2e}$, the superconducting flux quantum. As the field and density of vortices increases further, the whole material eventually becomes normal at the second critical field H_{c2}. Importantly, although the material expels the magnetic field, there will always be a length scale in which the magnetic field still penetrates the material. This is called the London penetration depth λ. Whether a SC is type-I or type-II is related to the ratio between the London penetration depth and the coherence length, which is explained below.

The most successful theory to explain superconductivity is the BCS theory, named after its developers Cooper, Bardeen and Schrieffer [92]. It is based in the main ideas that superconductors have a band gap and that the supercurrent is carried by pairs of electrons which lie inside this band gap. The supercurrent is carried by Cooper pairs, which are pairs of electrons (with charge $2e$) having opposite momenta and spin (at least in conventional SC). Cooper pairs form due to an attractive electron-electron interaction mediated by phonons which below T_c makes it energetically favorable for electrons to form pairs rather than stay apart. The pairing energy Δ will yield the value of the band gap (2Δ), which corresponds to the energy needed to break these Cooper pairs. Importantly, as Cooper pairs are effectively bosons, they create a condensate, in which the SC is defined by a global wave function $\psi \sim |\psi| e^{i\phi}$, where ϕ is a phase component which gets locked during the SC transition of the material. The length scale of the pairing potential Δ is given by the coherence length ξ, a magnitude that defines the size of the Cooper pairs. The coherence length plays a key role when putting a SC in contact with a non-SC material. In this case, the non-SC material will be affected by the SC condensate in a length scale in the order of ξ. Specifically, ξ will have an exponentially decaying behavior at the interface, which will induce superconductivity in the non-SC material in that region. This induced SC behavior is called the proximity effect, and is essential to understand the formation of Josephson junctions. In this framework, we can define the T_c and ξ in terms of the gap as:

$$\Delta \approx 1.764 k_B T_c \text{ and } \xi = \frac{\hbar v_F}{\pi \Delta}, \tag{2.24}$$

where v_F is the Fermi velocity of the proximitized material and k_B is the Boltzmann constant.

It is important to note that not all SCs can be explained by the BCS theory. For more complex materials, the attractive potential might not be a simple electron-phonon coupling, but it can be coming from enhanced electron-electron interactions [93, 94]. Materials which do not follow BCS theory, are generally called unconventional superconductors, and they typically have a SC wave function or order parameter which is anisotropic either in magnitude or phase [95]. The names of the symmetries are given by the shape of the wave function inspired by the nomenclature used for atomic orbitals, such that there are s-wave, d-wave, p-wave and f-wave superconductors, among others. BCS superconductors usually have an s-wave symmetry, having an isotropic magnitude and single phase. Some of the most important family of unconventional superconductors are the high temperature cuprate superconductors (with $T_c > 70$ K). These have d-wave symmetries, having an anisotropic magnitude and a phase which changes sign with momentum: $\mathrm{sgn}(\phi(\boldsymbol{k}^+)) = -\mathrm{sgn}(\phi(\boldsymbol{k}^-)$ [96, 97]. Although some of these materials were discovered ca. 40 years ago [98], there is yet no theoretical consensus of their unusual properties [99]. That is one of the reasons why understanding the SC in MATBG could be very interesting. MATBG is in principle a simple material (it is all carbon atoms) which has very strong electron-electron interactions, has magnetic ordering, a strange metal phase above the superconducting T_c and presents superconductivity next to correlated insulator states. These features are generally found in unconventional SCs with high T_c, not just in cuprate based, but also in Fe-based SC or heavy fermion systems [100]. It is then natural to think that if the origin of the SC in MATBG was understood, this could help understand other SC materials, or even engineer new ones [101].

2.4.1 Josephson junctions

A Josephson junction (JJ) is a device in which a non-superconducting material or weak link is intercalated between two superconductors. As the two superconductors are not directly connected, each of them will have a global wave function ψ, which will have a different phase ϕ in each superconductor, having $\psi_1 \sim |\psi|e^{i\phi_1}$ and $\psi_2 \sim |\psi|e^{i\phi_2}$ (considering the same SC material for both sides of the junction). The behavior of Josephson junction are characterized by the two Josephson equations: [102]:

- **DC Josephson effect**: a current is spontaneously driven across the junction when there is a phase difference between two superconductors:

  $$I(\phi) = I_c \sin\phi, \tag{2.25}$$

  where $\phi = |\phi_1 - \phi_2|$ is the phase difference across the junction and I_c is the critical current of the junction. This equation implies that the current will oscillate modulo 2π with ϕ.

- **AC Josephson effect**: as a DC voltage is driven through the junction, the phase will vary on time:

  $$\frac{\mathrm{d}\phi}{\mathrm{d}t} = \frac{2e}{\hbar}V. \tag{2.26}$$

  When combined with the first Josephson equation, this implies that an externally applied DC voltage will produce an alternating current in the junction:

  $$I = I_c \sin\left(\frac{2eV}{\hbar}t\right). \tag{2.27}$$

  The inverse is also true, such that when the JJ is irradiated with a radio frequency ω, a DC voltage is produced every time $V = \frac{n\hbar\omega}{2e}$, with n an being an integer. This response produces a set of steps in the IV curve which are called Shapiro steps.

The length of the JJs are limited by the coherence length of the SC materials. To a first approximation, to properly define a junction, the length of the junction (L in Fig. 2.6a) needs to be in the same order of magnitude as the ξ of the SC, such that there is an overlap between the ξ of both SC electrodes. This will be important later in the fabrication of the junctions.

2.4.2 Josephson junction under a $B-$field

When a Josephson junction is placed under an external perpendicular magnetic field B the I_c will decay in an exponentially oscillatory manner, creating what is called a Fraunhofer pattern. The reason lies in the fact that the global wavefunction $\psi = |\psi|e^{i\phi}$ needs to be single valued across the junction. This can be seen by taking a contour integral along the junction and studying how the phase evolves with the external flux [58]:

$$\Phi = \oint \boldsymbol{A} \cdot dl = (\Phi_0/2\pi) \int_{electrodes} \nabla\phi \cdot dl + \int_{link} \boldsymbol{A} dl, \tag{2.28}$$

where $\boldsymbol{A}$ is the vector potential. Since the phase ϕ must be single valued, the sum of the phase integrals must be equal to $mod\ 2\pi$. This means that the phase difference between the electrodes is given by:

$$\phi_1 - \phi_2 = 2\pi \frac{\Phi}{\Phi_0}\ (mod\ 2\pi). \tag{2.29}$$

This relation implies that ϕ_1 and ϕ_2 cannot be simultaneously equal to $\pi/2$ unless $\Phi = BA = n\Phi_0$ with A the area of the junction and $n = 0, 1, 2....$ Therefore, in order to have the maximal supercurrent flowing through the junction, the phase across the junction will periodically oscillate with position x (see Fig. 2.6b), This way, every time time $\Phi = n\Phi_0$, there will be a full number of oscillations of the phase across the junction. Each oscillation effectively acts as a vortex inside the junction area, and these can therefore be referred to as Josephson vortices. Following this structure, the maximum current (I_m) inside the junction at any given magnetic flux is given by:

$$I_m(B) = I_c(B = 0) \left| \frac{\sin(\pi\Phi/\Phi_0)}{\pi\Phi/\Phi_0} \right|. \tag{2.30}$$

This oscillatory decaying pattern is similar to the single-slid experiment in optics and is thus referred to as Fraunhofer pattern. If the current inside the junction is not homogeneous, this simple solution is modified by a more general Fourier transform. That will be explained more in detail in Ch. 6.

2.4.3 2D Superconductors

As MATBG is a 2-atom thick SC, it is convenient to look briefly at the theory of 2D superconductors. In a 2D superconductor, the film thickness is smaller than the London penetration depth λ and the coherence length ξ. In this case, the ruling length scale is the Pearl screening length $\Lambda =$

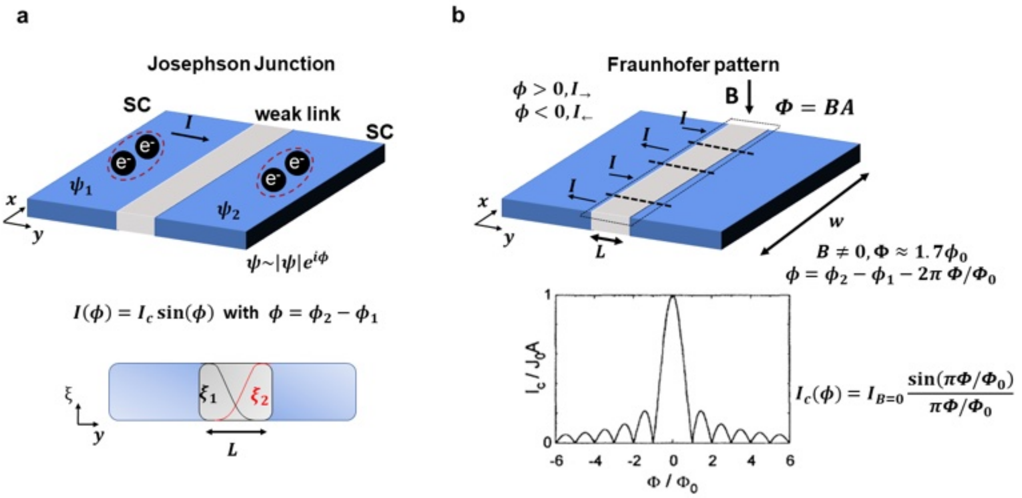

Figure 2.6: Properties of a Josephson junction. **a,** Schematic of a Josephson junction and the decay of coherence length across the junction (bottom). **b,** Josephson junction under a magnetic field. As the field increases the current oscillates along the x direction (signaled by the current direction in the figure) to keep the single valued condition of the phase across the junction. The right plot is an example of a Fraunhofer pattern.

$2\lambda^2/t$, where t is the film thickness [103] and the long-range order of the SC state is dictated by a Berezinskii–Kosterlitz–Thouless (BKT) transition [104, 105]. The BKT theory explains how a 2-dimensional system undergoes a phase transition to an ordered phase with an order parameter having both a magnitude and a phase (such as the SC state). Below the BKT temperature T_{BKT} the thermal excitations of the superconductor form vortex–antivortex pairs which bind together through an attractive 2D Coulomb force. The BKT theory predicts a non-linear $I-V$ characteristics for $T \geq T_{BKT}$ which scales as $V \propto I^3$ [106]. This dependence will be used in the experiments to extract T_{BKT} in MATBG experiments.

Finally, we look at the behavior of a JJ made with 2D SC materials, specifically at its behavior with magnetic field. In the 2D limit, as the thickness is smaller than λ, the magnetic flux can penetrate into the superconductor (thus not displaying Meissner) and the spatial distribution of magnetic field in the material is governed by the above mentioned Pearl length. It has been previously shown [107, 108, 109] that in this case the critical current of a 2D JJ under a perpendicular magnetic follows the relation $\Delta B_{2D} \approx 1.8\Phi_0/w^2$, where w is the lateral size of the junction. This is different from a 3D bulk JJ [58], where the period of the oscillations follows $\Delta B_{3D} \approx \Phi_0/wL$ where

L is the length of the junction. Considering a JJ with a realistic Hall bar geometry of $w \approx 1.2 \pm 0.1$ µm and $L \approx 100$ nm), ΔB_{3D} is estimated to be $\sim 16 \pm 1$ mT, while $\Delta B_{2D} \sim 2.5 \pm 0.5$ mT. Calculations for both cases are shown in Fig. 2.7 to display the clear difference of the behavior. The equation for the 2D superconductors will be later used in the analysis of our JJ devices in Ch. 6.

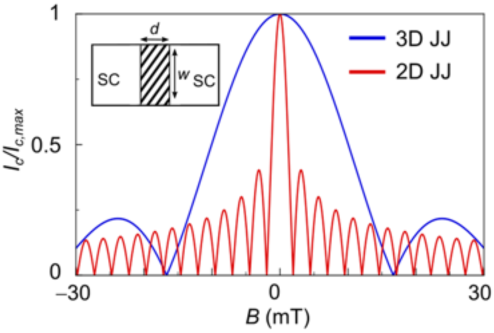

Figure 2.7: Fraunhofer pattern of a 2D vs. 3D superconductors. The 2D JJ oscillate at a much higher frequency than the 3D counterpart.

3 Materials and Methods

This chapter is divided in two main sections: sample fabrication and transport measurements. The section on sample fabrication discusses the protocol for the fabrication of MATBG in great detail. We start by explaining the process for the assembly of the van der Waals heterostructure and then explain the nanofabrication steps to create the devices. Apart from the technical details of the process, an emphasis is made to explain the little details which can make a big difference in the success of the fabrication process. The remainder of this chapter deals with the instrumentation and the basics of lock-in transport measurements, ending with some details about measuring MATBG. These include pre-screening devices at room temperature and extracting the twist angle at low temperature.

3.1 Sample fabrication: stacking and nanofabrication

The first step in the experimental process is the creation of the magic angle graphene heterostructures. The final devices will consist of a double graphite-gated Hall bar geometry of MATBG encapsulated in hBN as shown in Fig. 1.5. The two-dimensional (2D-) materials are assembled together using a modified dry-transfer technique [110, 21, 111, 38], referred to as the stacking process, in which a polymer stamp is used to assemble 2D materials in a layer by layer fashion. The process is designed with a focus in achieving the cleanest and most stable heterostructure which is important to avoid the relaxation of the twist angle away from the magic angle and reduce angle inhomogeneity. The explanation of the process highlights the details in careful flake selection, meticulous stack planning and precise control throughout the stacking process. First, we discuss the details of the exfoliation and flake selection, followed by a comprehensive explanation of the stacking procedure, emphasizing key points that can significantly impact the yield of the twisted devices. Finally, the stack is fabricated into a measurable electronic device via nanofabrication techniques, namely e-beam lithography, dry etching and metal deposition.

3.1.1 Stamp making

For the dry-transfer process we use a so-called stamp, a polymer heterostructure consisting of a small square of ca. 2×2 mm of 1 mm^2 thick commercially available polydimethylsiloxane (PDMS) covered by a polycarbonate (PC) film mounted on a glass slide, which is made following the work of Zomer *et al.* [111]. The PDMS is used to act as a soft viscoelastic cushion when approaching to pick up the flakes and the small size is chosen such that the contact point of the PC (which we generally refer to as the wavefront) with the Si surface can be easily controlled. The decision to use PC as the adhesive layer is motivated mainly by its high adhesion properties to the used materials and because it permits to perform the stacking process at higher T than other materials such as polypropylene carbonate (PPC) [112]. As is explained in detail later, the higher temperatures enhance the quality of the transfer process.

To make the PC film first a a 6% (w/w) solution of polycarbonate dissolved in chloroform is made by introducing PC pellets in a beaker with chloroform and magnetically stirring overnight at room T. Once the PC is fully dissolved the solution is kept tightly closed and can be used for several weeks. As the chloroform will evaporate over time, the concentration will change making the solution no longer usable. The PC film is then made by transferring a few drops of the PC film onto a glass slide. To have a homogeneous film a second glass slide is pressed onto the first one and they are slid on top of each other leaving a homogeneous film on both glass slides (process shown in Fig. 3.1). We have found that films which give the best results are 2 – 3 µm thick. Finally the glass slides with the PC film are put in a hot plate at $\sim$ 100 °C for 2 min to evaporate the excess chloroform and improve the homogeneity of the PC film.

The procedure to make the stamps is shown in Fig. 3.2 and is as follows:

- A small square of PDMS of $\sim 2 \times 2$ mm^2 is placed on top of a clean glass slide.
- The PC film is cut into squares of about 1 × 1 cm.
- A hole larger than the PDMS square is made in a piece of scotch tape. The hole is used to expose the PC only in the region where there is PDMS below.
- A square of PC is picked up with the scotch tape and transferred on top of the PDMS. When transferring the PC film on top of the PDMS it should remain flat, without visible wrinkles.
- The extra scotch tape is cut. The stamp is now finished.
- After finishing the stamp, it is heated to 120 °C for about 5 min. This will soften the PC as it approaches its glass transition temperature

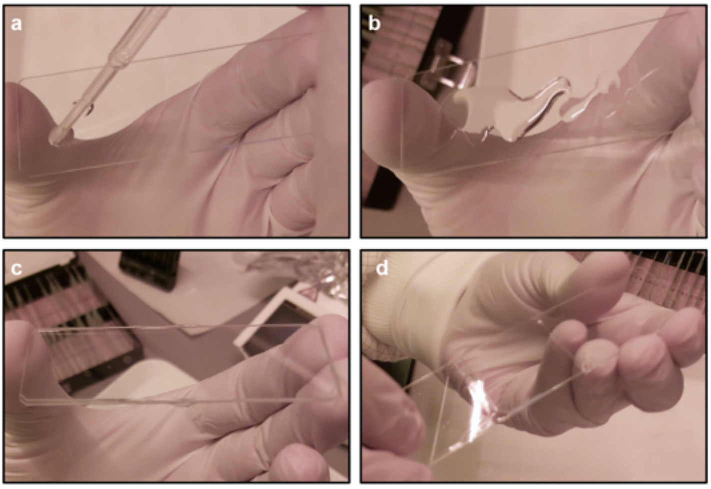

Figure 3.1: PC film making process. **a,** A syringe is used to pour a few drops of PC solution on a glass slide. **b,** The PC solution poured on the glass slide. **c,** A second glass slide is placed on top of the one with the PC solution. **d,** The second glass slide is slowly released leaving a homogeneous PC film on both surfaces.

$T_g \approx 147$ °C, making it conform better to the PDMS and thus improving its adhesion to it.

3.1.2 Exfoliation

The 2D materials which will be used during the fabrication process are obtained by mechanical exfoliation onto a Si substrate with a capping layer of 285 nm SiO_2. The 285 nm SiO_2 substrate is used for its optical contrast, which allows to easily see monolayer graphene flakes [113]. The exfoliation process for graphene, hBN and graphite is similar, following mainly the process developed by Huang *et al.*: pre-cleaning the chips in O_2 plasma and heating up the substrate to $\sim$ 100 °C for $\sim$2 min to increase the exfoliation yield [114]. First, I will describe the process to exfoliate graphene and then explain the differences for hBN.

3.1.2.1 Graphene exfoliation The procedure to exfoliate graphene is shown in Fig. 3.3 and is as follows:

- The Si/SiO_2 chips are cleaned with O_2 plasma for 3-5 min. The O_2 plasma removes ambient adsorbates from the surfaces of the chips, increasing its adhesive properties. This increases the yield of usable

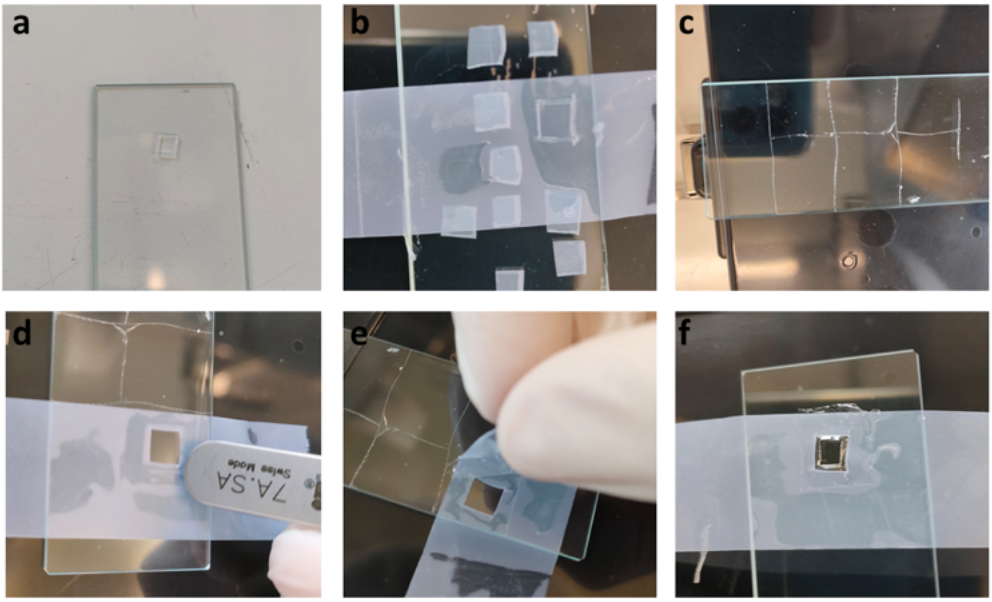

Figure 3.2: Stamp making process. a, A PDMS square is placed on top of a clean glass slide. **b,** A hole larger than the PDMS square is cut on a scotch tape piece. **c,** The PC film is cut into small pieces to be picked up. **d,** The cut scotch tape is used to pick up the PC film. The back of the tweezers is used to ensure good contact between the tape and the PC film. **e,** The tape with the PC film is slowly released to avoid breaking it. **f** The PC film is placed on top of the PDMS. After cutting the excess tape the stamp is finished.

flakes which will be attached to the surface during the exfoliation process.

- A crystal of graphite is placed on a scotch tape. The crystal is then removed, leaving a large piece of graphite on the tape.
- The tape is folded several times (∼ 7-8 times) until most of it is covered in graphite flakes. The aim is to cover as much tape as possible with the minimum number of folds, as each fold will reduce the size of the potential graphene flakes.
- Once the tape is homogeneously covered in graphite flakes, it is pressed against the cleaned Si/SiO_2 chips to attach the flakes to the surface of the chips.
- The chips are then placed in a hot plate at ∼ 105 °C for 2 min. The heating increases the contact between the flake and the SiO_2 by removing gas from the interface, and thus increasing the van der Waals

forces between them. However during heating the glue in the tape will also adhere to the SiO_2 surface, leaving unwanted residues around the graphene flakes. The longer the heating time the more residues there will be. In general, heating for 2 - 3 min gives a good equilibrium between a high exfoliation yield and few residues, while heating for longer will give too many tape residues, therefore being detrimental for the process.

- After removing the tape from the hot plate, it is left to cool down for ~10 - 20 sec. Then the tape is peeled off from the chips very slowly. The slow motion is very important to avoid flakes from breaking, obtaining larger flakes. The waiting time before peeling the tape allows to remove the tape more slowly, as otherwise the glue will be too soft and the peeling off will be less controlled.

The exfoliation works such that the graphene flakes experience van der Waals forces both to the tape and the SiO_2 chips. When the tape is removed, the interaction between graphene and SiO_2 overcomes the vdW forces between the layers, making the flakes cleave leaving atomically clean surfaces exposed on the SiO_2 flakes. In this way, flakes of many different thicknesses are obtained on the SiO_2 chips. We are interested both in large monolayer graphene flakes which can be used for the MATBG, and thicker smaller graphite flakes which can be used for metallic gates. These can be distinguished by their optical contrast on the 285 nm SiO_2 chips. Monolayer graphene looks very similar to the light purple background color of the SiO_2 (see Fig. 3.4), while thicker graphite flakes will have a darker purple color. Once the color becomes blue, the flakes are too thick for our purposes.

3.1.2.2 hBN The hBN crystals are exfoliated in a very similar manner, with a few key differences:

- The original hBN crystals are much smaller than graphite, such that instead of starting with a single large crystal (as in the case of graphene), we start using several smaller hBN crystals.
- "Daughter" tape. The folding of the tape is done in a similar manner until the tape is heavily covered in smaller hBN crystals. However, in this case, the crystals are usually too thick to directly exfoliate in Si chips. Therefore in general a "daughter" tape is obtained by using a second tape and exfoliating from the first "mother" tape (see Fig. 3.5 for an example). The "mother" tape can be used for several "daughter" tapes. In general if the crystals on the tape are very bright, this will lead to very thick hBN crystals which are not useful for stacking.

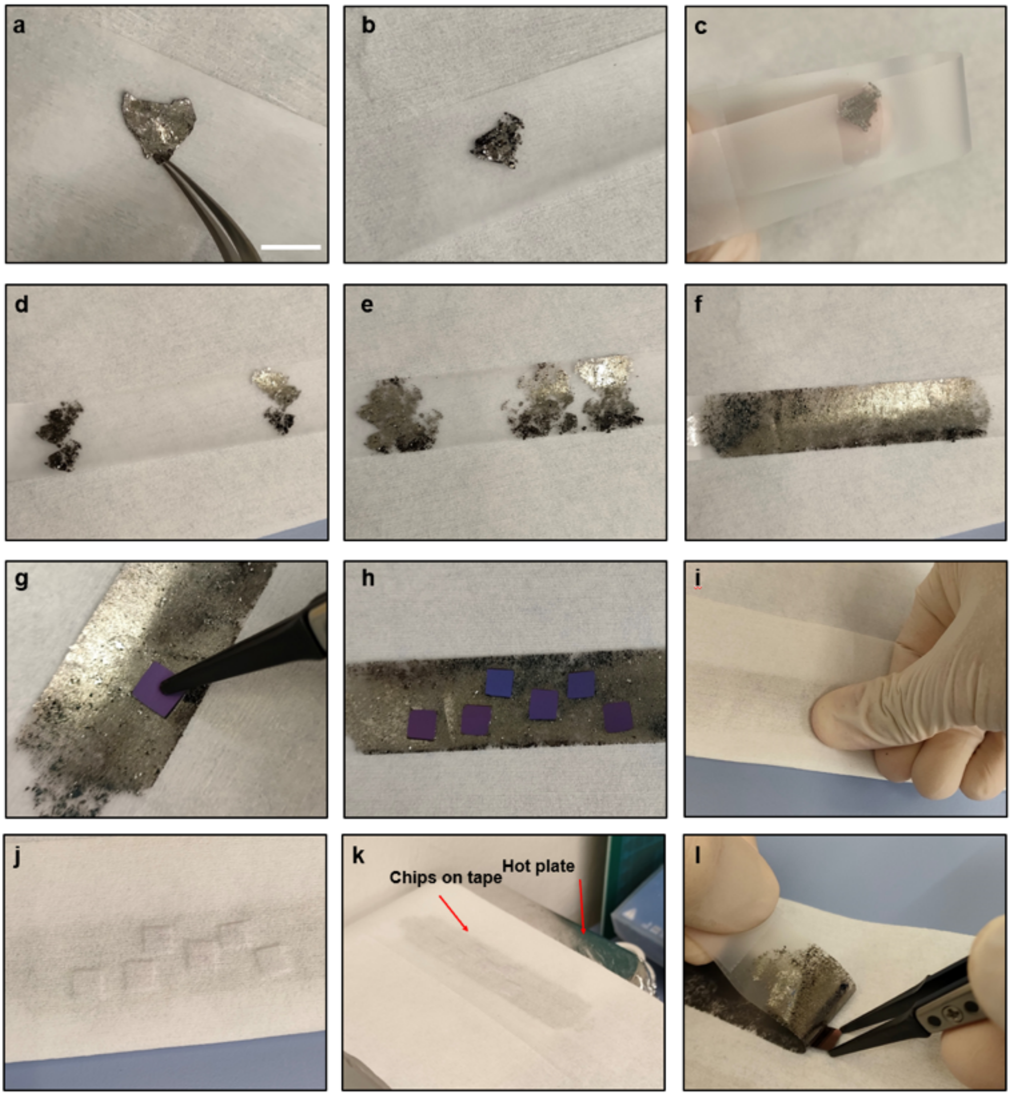

Figure 3.3: Graphene exfoliation. **a,** A graphite crystal is placed on top of the scotch tape. **b,** The crystal is removed, leaving the exfoliated crystals on the tape. **c,** The tape is folded to exfoliate the crystal, filling the tape with several thinner graphite crystals. **d-f** The crystals are exfoliated until covering the whole tape. **g,** A chip is placed on the tape region with graphite and gently pushed on the back. **h,** Several chips are placed on the tape. **i,** A soft tissue is used to press the chips on the graphite crystals to increase the exfoliation yield. **j,** After pressing, the chips are properly attached to the tape with the graphite crystals. **k,** The chips are placed on a hot plate at ~105 °C for 2 min. **l,** Finally the chips are slowly peeled off from the tape. The scale bar in **a** is 5 mm.

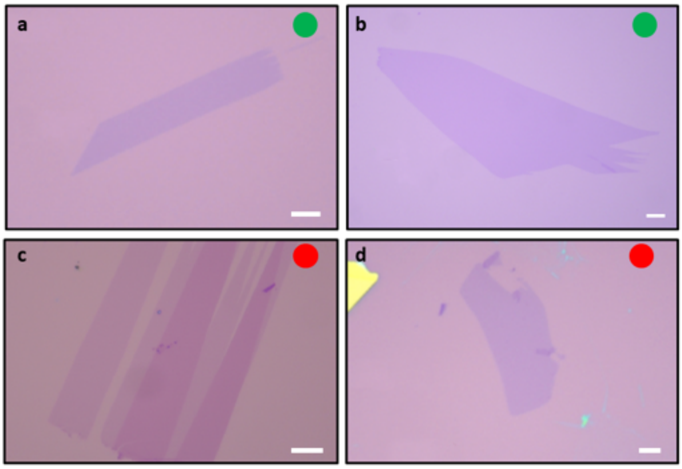

Figure 3.4: Graphene exfoliation results. a-b, Good graphene flakes:**a,** shows an elongated flake while **b,** shows a larger flake . Both of these could be used for making TBG samples. **c-d,** Not usable flakes: **c,** Good graphene flakes, but too close to a larger graphite flake, making it very hard to use them. **d,** Small flake and with several defects. Upon cutting it in two, it would be too small to use it for fabrication. Scale bar is 10 µm.

Once the crystals in the tape have a more grayish, not-so-bright color, the crystals are too thin and they cannot be used anymore to create “daughter” tapes. Once the “daughter” tape is made, it is directly used to exfoliate on the Si/SiO$_2$ chips. Making the “daughter” tape more dense by folding it again with itself is likely to break the crystals into very small pieces which are not useful for the stacking process.

- The chips are not heated prior to the exfoliation process. Although using a hot plate can increase the exfoliation yield, in the case of hBN the tape is not as dense as in the case of graphite, which means that there will be too many tape residues on the final chips. However, it is still important to wait a few minutes with the chips on the tape before removing it.
- Less force is applied to the chips in comparison to the exfoliation of graphene. If the hBN is pressed too hard the flakes will break leaving much smaller flakes than desired.

3.1.2.3 Top gates A final note is made for exfoliating the graphite that will be used as top metallic gates. In general, PC adheres to hBN more strongly than to graphite. Therefore, during the stacking process, PC can

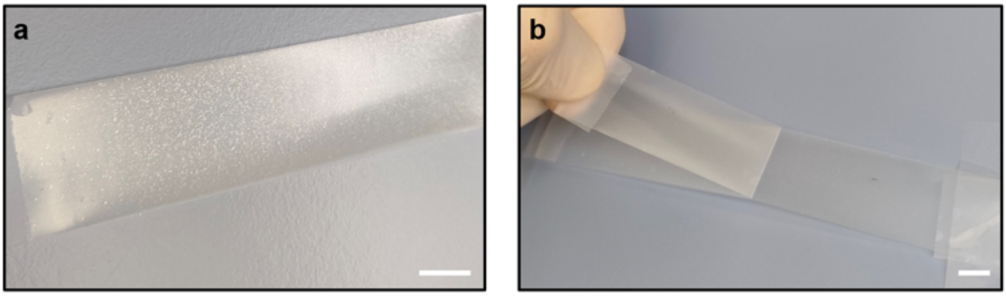

Figure 3.5: hBN exfoliation with "daughter" tape. a, Original tape with the hBN exfoliated crystals. The tape is full of bright crystals. **b,** A "daughter" tape is exfoliated from the original tape.

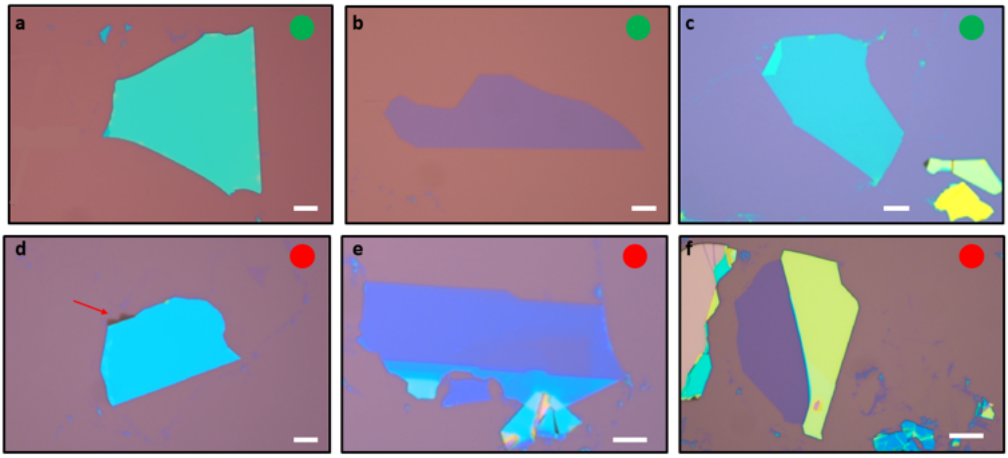

Figure 3.6: hBN exfoliation results. a-c Good hBN flakes. All the flakes could be used for stacking. **a,** or **c** would be good example for top flakes since they have a sharp edge which we can use to align with the cut graphene edge. **d-f,** Not good flakes. **d,** Good flake but with a fold (marked by the red arrow) that could break the stamp during the stacking. **e,** Good looking flake, but having different thicknesses, this is not desired since it will give different gating profile along the device. **f,** Good flake with thicker regions attached to it. Scale bar is 10 µm.

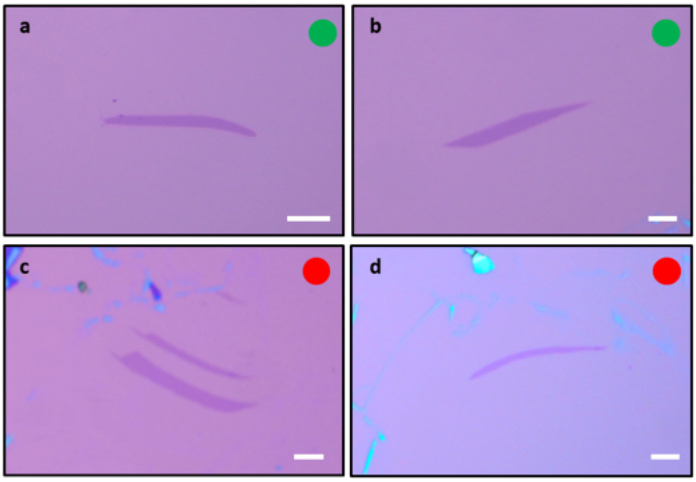

Figure 3.7: Graphite flakes. a-b, Good graphite flakes. Elongated, about 3 μm wide and not too thick. **b** shows a good bottom gate flake, having a kink, which will make it very easy to contact later on. **c-d,** Not usable graphite flakes. **c** shows two flakes together, while **d** shows a non-straight flake. Both are undesirable. Scale bar is 10μm.

be used to pick up hBN from the Si chips by using the right temperature range while picking up graphite or graphene flakes has a lower success rate, resulting in broken flakes after the pick up process or not picking up the flakes. As in the double gated devices, the graphite is the first layer which is picked up during the stacking process it is essential to have a reliable pick up of the graphite flakes. The key to achieve this reliable pick up is to exfoliate the graphite flakes which will be used for top gates without O_2 plasma cleaning of the surface of the SiO_2, as previously reported [115, 21]. Although this reduces the yield of the exfoliation, the flakes can be more reliably picked up. In this way the reduced number of flakes is compensated by the fact that most of the obtained flakes will be easily picked up during the stacking process.

3.1.3 Flake selection and stack organization

Prior to the stacking process, all the potential flakes are cataloged, and a tentative plan is made by choosing the best fitting flakes for a stack. This allows to carefully think of the size, shape and moreover compatibility of different flakes to be used and minimizes errors during the stacking process. There are several considerations for the individual flakes as well as relations between the different flakes of the stack (As shown in Figs. 3.4, 3.6 and

3.7). In general, the first order criterion in identifying viable flakes is how pristine and homogeneous they are. Selected flakes should have no tape residues, nor step-terraces and should be well isolated from nearby bulky flakes which typically causes problems during the stacking process. Then, there are certain constraints to consider regarding the different materials.

The graphene flake for MATBG should be at least twice as large as the desired device size. Flakes which are ∼10 - 15 µm × 15 - 30 µm are typically desired, such that the final devices are ∼ 10 µm long. The hBN flakes should fully encapsulate the graphene and are chosen to be 10 - 20 nm thick for several reasons. Firstly, thinner hBN flakes make the stacking smoother, aiding to avoid unexpected rapid movements or “jumps” in the stamp during the stacking which can give rise to bubble formation [110]. In general, we aim to minimize bubble formation as much as possible since it significantly contributes to angle inhomogeneity [116]. However, if the flakes are too thin (i.e. below 5 nm), they tend to tear during the stacking. Secondly, spotting dirt or defects in the optical microscope is easier in thinner flakes. Finally, a thin top hBN allows to see through during the stacking, which is helpful when making multilayered stacks: for flakes thicker than 20 nm, seeing the graphene layers and/or the bottom graphite flake can be challenging. Graphite gates are chosen to be ∼2 - 4 nm thick, 3 - 6 µm wide and 10 - 15 µm long. The width is chosen such that the arms of the Hall bar which extend beyond the width of the device can be gated away from the charge neutrality point using the highly doped Si substrate, which helps minimize the contact resistance. Flakes below four layers are avoided due to their complex properties, including magnetism in rhombohedral trilayer graphene [99], and their insufficient screening of the charge puddles in the SiO_2 substrate [117], while thicker flakes are also avoided since they would induce more strain to the final stack, i.e. as they are narrower than the twisted graphene regions, they would produce a larger curvature the thicker they are [118]. The bottom gate needs to be longer than both the graphene and the top gate, such that the part that extends beyond them can be easily contacted during the lithography process. Finally, the top gate should be wider than the back gate. This way the region gated only by the top gate, can be also gated with the Si gate. This is very important in MATBG due to the existence of highly resistive states which can completely dominate the measured signatures otherwise, as is explained in detail in the next chapter.

3.1.4 Transfer stage

The dry transfer stacking technique is done using a so-called “transfer stage” or “stamping setup”. The transfer stage consists of a modified microscope in which the van der Waals heterostructure assembly can be performed. The main components of the transfer stage are (see Fig. 3.8 for reference of the different parts):

(a) Heavy table for vibration stability and screw holes to hold the different pieces.

(b) Sample stage platform with X-Y and rotation control. In order to accurately rotate the two graphene sheets by an angle of 1.1°, the sample stage (b1) is placed on top of a goniometer (b2). The goniometer used in this thesis had a precision of 0.0016°, giving a sufficiently precise angle control for the fabrication of MATBG.

(c) Micromanipulator stage. A metallic "arm" (c4) which extends towards the sample stage where a glass slide with the stamp can be held during the assembly process. The X-Y manipulators (c1) are used to move the stamp around the sample to choose the right region and the Z manipulator (c2) is used to control the height and therefore make contact or retract the contact from the sample. An important feature of this stage is to have control over the tilt angle on the X-Y plane (c3). By setting the right tilt, the angle at which the stamps will make the contact with the sample can be controlled. This allows to control the stacking direction and the smoothness of the contact between the stamp and the sample. Having a very large tilt angle a large force will be put on the PC film, while having a low angle will not allow to control the point of contact, nor the wavefront of the PC film.

(d) Vacuum pump and valves. Vacuum is used to keep the sample, the stamp arm and the stamp in place during the stacking procedure.

(e) Long working distance objectives. The microscope used for the transfer stage needs to have long working distance objectives in order to focus on the sample while looking through the stamp.

(f) Temperature control. A heater and thermometer are enclosed in the sample stage to control the temperature. The temperature control is used to change the properties of the PC film during the stacking procedure.

(g) Binoculars to search for flakes and follow the stacking procedure.

(h) Aperture diaphragm control lever. During most of the stacking process the sample will be focused through the glass slide having the PDMS/PC stamp and it will be key to be able to properly focus on the stamp itself. This will affect the resolution of the microscope, making it hard to focus correctly. In order to avoid this issue the aperture control feature of the microscope is frequently used. This setting closes the aperture of the light path, having a two-fold effect: increasing the focal length and reducing the scattered light from the sample. These combined effects allows to properly focus on the sample and/or see the flakes on the stamp. The aperture control can also be used to increase the visibility in defects on flakes. Examples of its use are shown in Fig. 3.9.

(i) Camera and imaging software. Most of the stacking is done with the image acquired by the camera and using the imaging software of the microscope. This is specially important for the stacking procedure for three main reasons. Firstly, changing the contrast and color saturation of the camera will allow to see defects in flakes which are not visible with the naked eye. Secondly, it allows to outline the shapes of the different flakes. For double gated stacks this is very important for the last step, in which the top and bottom gates will be aligned. As more layers are picked up with the PC stamp, visibility through the layers decreases. That means that depending on the thickness of the chosen graphite gate and mainly hBN flakes, it is possible that when picking up the bottom graphite gate, the top graphite gate is no longer visible. In this case, having outlined where the top gate is positioned with respect to the other flakes enables a proper alignment with the bottom gate. The same applies to the graphene, which will not be visible once the bottom hBN is picked up. Finally, saving the images of the stacking process is necessary to make the device design for the nanofabrication. Since the graphene and the gates might not be visible once the stack is finally dropped on a SiO_2 chip, having pictures with the position of the different flakes is essential to design the final device.

(j) Fan. A fan is added to cool down the stage faster. This can be useful after dropping the stack for example, since the stage will be at 180 °C.

(k) Filters. Using filters can help detect defects in the flakes which are not visible otherwise.

(l) White light source.

3.1.5 Stacking: Graphene cutting

The MATBG devices are always fabricated using a cut-and-stack technique[48], where a single flake of graphene is cut in two pieces using an AFM cantilever. This approach induces less tension in the original graphene flake, thus reducing the chance of relaxing the twist angle compared to the original

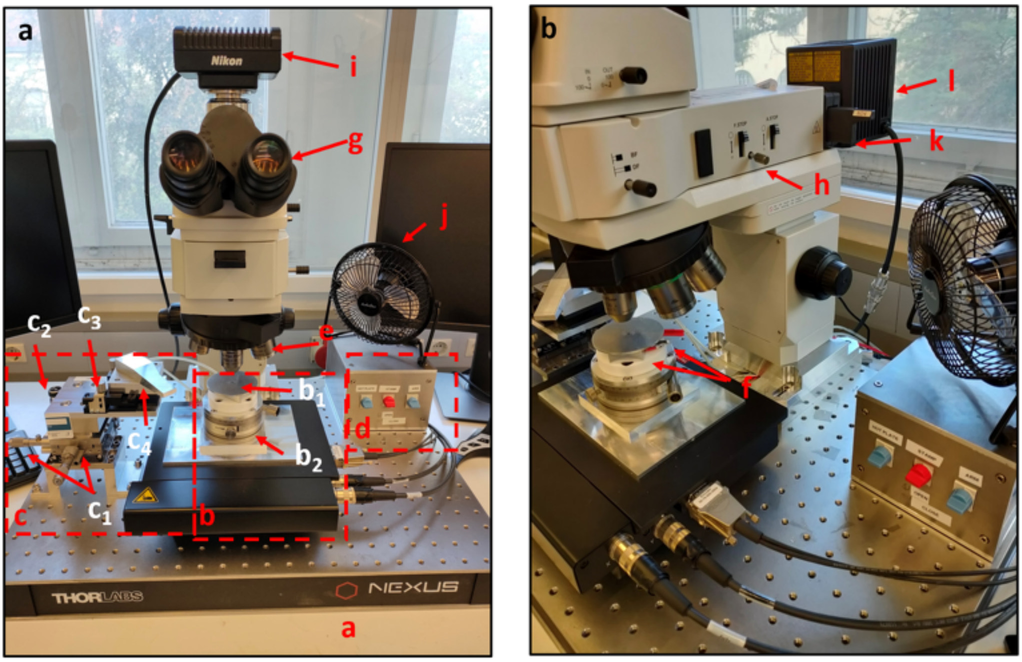

Figure 3.8: Transfer stage from the front and side view. The letters correspond to the different parts explained above.

tear-and-stack [21, 37]. The devices are always made starting from a single graphene flake to ensure relative crystal orientation matching prior to the layer rotation. Graphene is cut at room temperature in the transfer stage by using a glass slide with an AFM cantilever mounted on a PDMS platform. The set-up is very similar to the PC stamps: a small PDMS square is placed on a glass slide and an AFM cantilever is placed on the edge of the PDMS and secured with scotch tape (Fig. 3.10a). To cut the graphene, the glass slide with the AFM cantilever is placed on the micromanipulator of the transfer stage and lowered towards the chip with the desired graphene flake until contact is made. The point of contact can be seen as the cantilever deflects changing its reflectance. Once the cantilever is in contact with the Si chip close to the desired graphene flake, the sample stage is moved over the flake, which results in a clean-cut ca. 1 µm wide (Fig. 3.10b and c.). The cut is performed at room temperature to avoid sudden relaxation of the graphene flake, as at higher temperatures it tends to fold onto itself.

The AFM cantilever set-up can also be used to move flakes [119, 120]. This is especially useful when a flake is very close to the desired flake, such that it might negatively affect the pick-up process. By precisely controlling the AFM cantilever with the micromanipulators, one can fully remove a flake

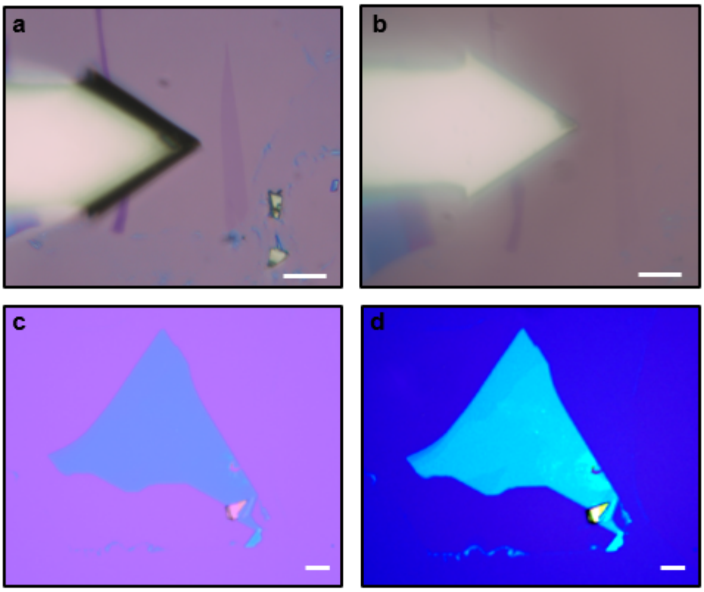

Figure 3.9: Using the aperture diaphragm control of the microscope. **a,** The aperture diaphragm is closed, allowing to focus on the graphene flake and seeing clearly the AFM cantilever during cutting as described in 3.1.5. **b,** The aperture diaphragm is open. The graphene flake is now barely visible. **c,** Apparent clean hBN flake. **d,** Upon closing the aperture and changing the colors and contrast of the came is possible to see defects in the hBN flake. Scale bar is 10 µm in all figures.

from the area as shown in Fig. 3.10d - f. The example shows the removal of an hBN flake, but the same process can be used for graphite flakes, and even for other residues present in the chip surface, such as Si residues from the dicing. This is useful to get a cleaner surface around the desired flakes, which helps to ensure that the lamination (the process of fully covering a flake with the stamp) over the flakes is done slowly in a controlled manner. This avoids the appearance of bubbles, helps squeeze any present bubbles out and lowers the chance of relaxing the twist angle.

3.1.6 Stacking process

After cutting the graphene and pre-selecting all the flakes, the stacking process may begin. The entire pick-up process is done at a $T \sim 100$ - 120 °C. The lamination on the flakes is done at constant T, approaching by hand using the z-micromanipulator on the transfer stage. The high T used throughout the process serves to improve self-cleaning by enhancing bubble mobility in all the pick-up steps [115, 112]. The overarching theme is for

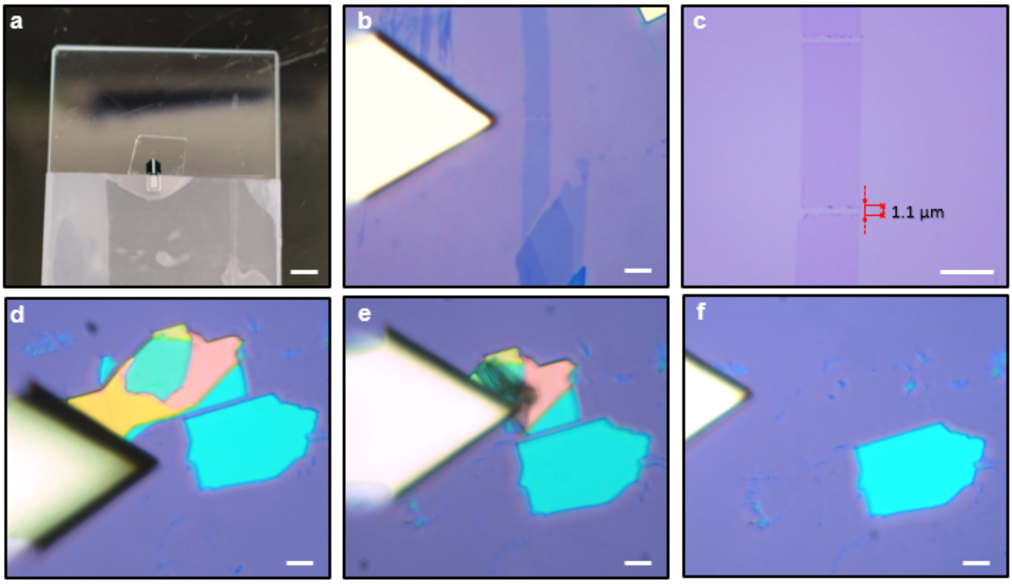

Figure 3.10: AFM cantilever cutting and deterministic cleaning. a, AFM cantilever on PDMS placed on a glass slide to be used in the transfer stage. **b,** The AFM cantilever is used to cut the graphene in-situ in the transfer stage. **c,** Zoom-in of the cut made in the flake in **b**. **d,** The AFM cantilever is used to remove the thicker flake besides the flake of interest. **e,** The second flake is being folded onto itself using the cantilever. **f,** The undesired flake is completely removed from the area while the good flake remains in place. The scale bar in **a** is 3 mm and 10 µm in the rest of the figures.

the stacking process to be as smooth as possible, which involves having full control of the stamp wavefront and avoiding bubble formation. In the following the fabrication of a double gated MATBG device is explained, which can be extended to more layers or to single gated devices following the same recipe. A schematic and a real stacking process are shown in Fig. 3.11 and Fig. 3.12, respectively. The steps are as follows:

1. **Selecting a clean region of the PC/PDMS**. In order to achieve the cleanest 2D interfaces possible, we want to avoid bubbles from forming during the stacking process as explained above. Typically, bubbles form during the stacking process mainly because of dirt on the surfaces of the different 2D materials [115, 112] or as a result of approaching too fast, which can trap air along the interface [121]. If the stacking process is done in an area of the PC film which already has some dust particles, bubbles, etc. this could hinder the pick-up process and introduce bubbles into the whole stack. Therefore, the first step is to locate a clean

region on the PC film which is larger than the largest flake to be used. Once this is chosen, the top graphite gate is picked up.

2. **Top graphite gate**. The direction with which the PC is approached in every step is important since it marks the relative orientation between the flakes. The approach to pick up the graphite flake, as well as all the consequent flakes, is as follows: The chip with the desired flake is placed in the heated sample stage and kept stable by applying vacuum on its back side. The stamp is lowered until contact is made with the heated SiO_2 surface. The point of contact is evident from the change in the deeper apparent color of the contact area, which is surrounded by Newton's rings. (see Fig. 3.12a, d and g). In general, the tilt angle of the stamp micromanipulator is set such that the stamps make contact in a corner, which allows for a better control of the wavefront. A sudden "jump" or fast movement of the PC film can tear, move or induce bubbles in the heterostructure. Once the PC has fully laminated over the flake, the stamp is pushed slightly further and then retracted slowly. When the flake is picked up, the PDMS/PC film will acquire a dark shadow in the shape of the flake, unlike the characteristic purple color it has on the SiO_2 surface.

3. **Top hBN**. The top hBN is generally chosen to have at least one sharp edge. This facilitates to fully laminate over the 1st graphene flake while avoiding any contact between the PC or the hBN with the 2nd graphene flake. The top hBN should be larger than the top graphite, to prevent the graphite and graphene layers from shorting.

4. **First graphene**. When picking up the graphene, the chip is arranged such that the cut in the graphene is aligned to the sharp edge of the top hBN (Fig. 3.12b). The wavefront is approached very slowly to avoid any unintended movement of the graphene, as any movement of either the top or bottom graphene sheet can cause a distortion in the twist angle. Once the hBN is in contact with the graphene, the wavefront is further moved until the entire first graphene sheet is covered with hBN, while ensuring that the PC does not touch the second graphene. As soon as the first graphene sheet is in full contact, the stamp is slowly retracted and then moved a few mm above the Si chip. During this pick-up step the graphene flake is "clamped" with the top hBN layer. This means that an edge or a corner matches between the two flakes. When the "clamping" is done correctly, part of the graphene flake edge ($\sim$ 1 µm) effectively folds over the edge of the hBN, which is visible in the optical images (see Fig. 3.12b-d). This process effectively re-

stricts the movement of the graphene sheets, preventing the twist-angle relaxation thus significantly increasing the yield of the devices with the desired twist-angle. Importantly, the “clamping” has to be done in non-crystallographic axis of the graphene and/or hBN to avoid unintentional alignment between the layers, which would induce an additional moiré pattern and influence the electronic properties of the stack [51, 122]. Therefore the “clamping” is not done between perfectly straight edges (which point to possible crystallographic axes) but rather asymmetric edges of similar size. Using the cut edge of the first graphene is an ideal “clamping” point because the rippled graphene provides more roughness. Therefore, one strategy is to cut the graphene not just in two pieces, but rather in three, giving a cut edge also for the second graphene layer, as is done in Fig. 3.12b-d.

5. **Second graphene**. While the stamp and the top half of the stack is hovering over the chip, the sample stage is rotated by 1.1 - 1.2°. As the twisted graphene tends to relax towards $\theta = 0°$ when making contact, the sample stage is rotated at a slightly higher angle than the desired twist-angle. After rotating, the second layer of graphene is overlapped with the first graphene layer and the pick-up procedure is repeated. The second graphene is also “clamped” with the hBN.
6. **Bottom hBN**. The bottom hBN pick up has to be done in such a way that it fully encapsulates all the previous flakes and that it will cover the bottom graphite gate. This means it should be larger than all the previous flakes.
7. **Bottom graphite gate**. The bottom graphite gate should be entirely covered by hBN. If not entirely covered, it will have different adhesive behaviors between the hBN-covered region and the polymer-covered region, consequently inducing tension or strain during the pick-up process This tension can relax the twist angle, and/or even displace the position of the graphite gate, destroying the whole stack. In double gated devices this pick-up step is even more crucial since both of the gates need to be perfectly aligned in order to have a working device.

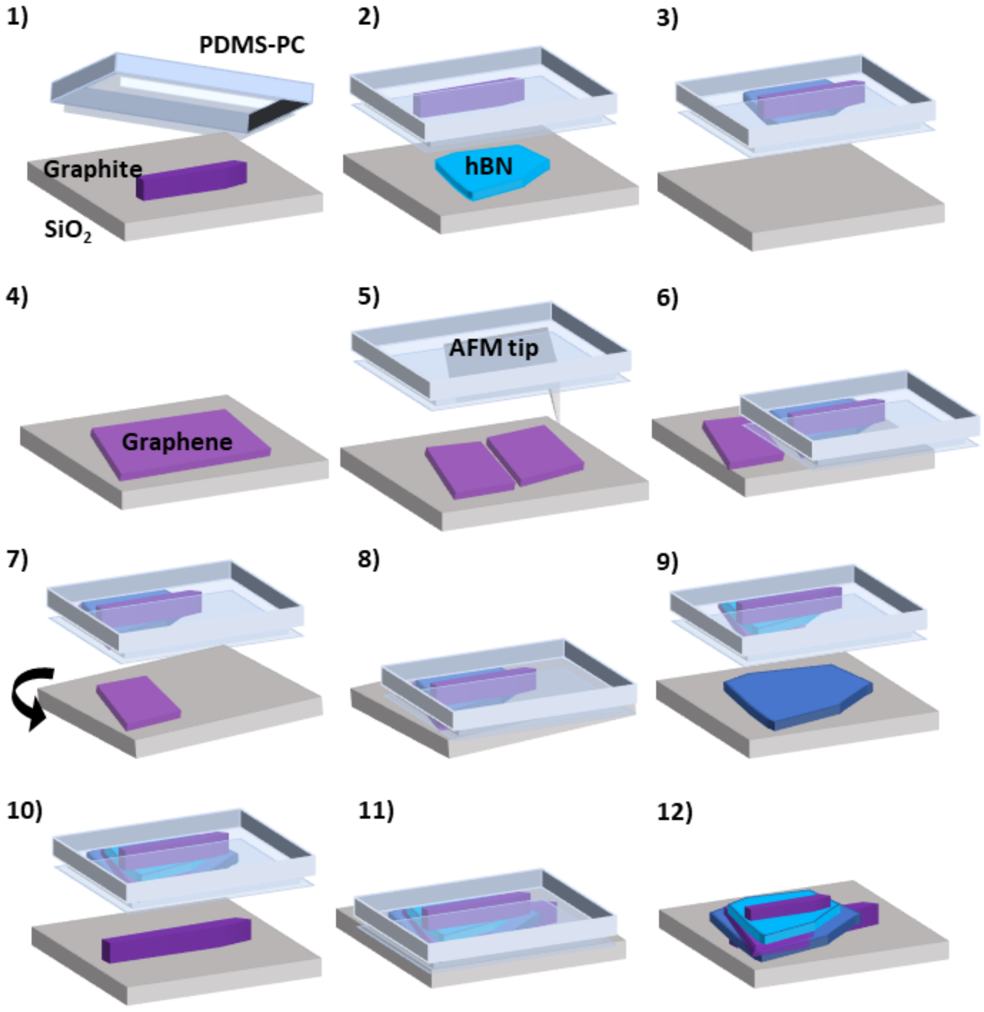

Figure 3.11: Diagram of the stacking process. The numbers follow the order of the steps described above. The gray rectangle represents the Si/SiO2 substrate. The narrow elongated purple shapes are the graphite flakes, the blue shapes are the hBN flakes and the thin purple shape represents graphene. The semi-transparent feature represents the PDMS/PC stamps.

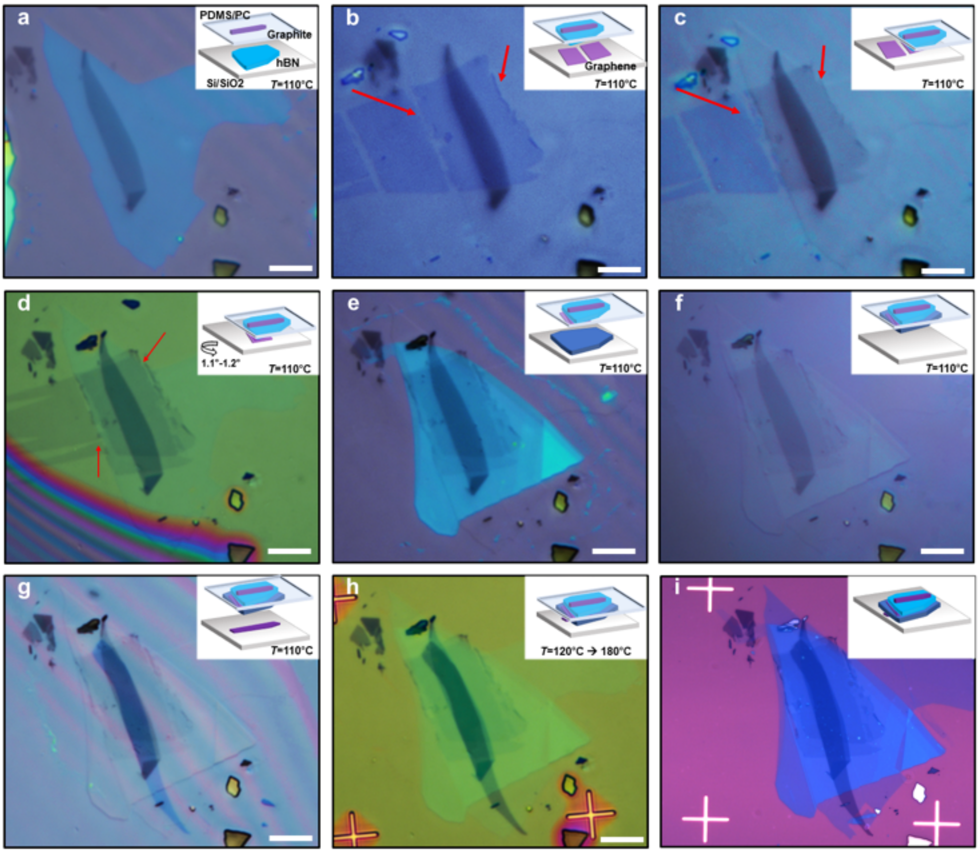

Figure 3.12: Stacking process. a, Picking up the top hBN, top graphite is already picked up. **b,** Aligning the top hBN with the 1st graphene flake. **c,** 1st graphene is picked up. The change of color signals that the pick up was successful. The red arrows point to the edge having "clamped" over the hBN. **d,** Stamp is passed over the 2nd graphene after rotating the stage 1.1°. Red arrows points to the places where the 2nd graphene "clamps" over the 1st graphene. **e,** Both graphene flakes are now picked up. **f,** Picking up the bottom hBN. **g,** Aligning the stack over the bottom graphite gate. **h,** The stack is dropped on a pre-patterned chip with markers. **i,** Clean stack after removing the PC. The final stack had an angle of 1.08°.

8. **Dropping the stack**. Finally, the complete stack is dropped in a prepatterned Si/SiO_2 chip with alignment markers to facilitate the subsequent nanofabrication process. The chips are cleaned with O_2 plasma to improve the adhesion with the 2D layers. The contact between the PC film and the chip is now made at $T \sim$ 120-150 °C to enhance bubble mobility. The wavefront is moved very slowly over the stack to push away all the remaining bubbles [112]. Once the full stack is in contact with the Si, the wave front is moved ca. 200 µm further from the stack. Now the T is raised slowly up to 180 °C. As the T approaches the glass transition temperature T_g of the PC of $\sim$147 °C [112] the PC detaches from the PDMS film and at T far beyond the glass transition $\sim$180 °C, the PC completely melts. For our PC/PDMS stamps and transfer setup the detaching happens at $T \approx$130 °C. At this point the z-micromanipulator is moved up slightly to detach the entire PC film from the PDMS. During this process (130 °C $< T <$ 180 °C), we make sure that the PDMS is not in contact with the PC film by moving the stamp slightly up every time the Newton's rings reappear. Once the $T \sim$ 180 °C, the stamp is fully retracted. At this point the PC in contact with the chip is melted and it will detach from the remaining PC on the glass slide. The T ranges in the step are very important. Retracting too far at a low T can break the stack, while if the T is raised without detaching the PC from the PDMS, the expansion of the latter can put pressure on the stack. During the entire process, the x-y micromanipulator of the stamp and the sample stage should not be moved since this will may the stack. Once the stack is dropped, the T of the stage is lowered to room temperature. The stacking process is now finished.

9. **Cleaning the PC**. The final step prior to the lithography is to clean the PC. The chip is left in chloroform for 2 min, followed by rinsing in acetone for 1 min, isopropanol for 1 min, and blow dried with N_2.

3.1.7 Lithography: etching and evaporation

In order to convert the heterostructures of van der Waals materials into electronic devices, nanolitography techniques are used. We will use mainly three techniques: electron beam lithography (EBL), reactive ion etching (RIE) and metal evaporation (see Fig. 3.13), which are briefly explained below. For further discussion the reader is referred to materials such as Ref. [123].

3.1.7.1 Electron beam lithography Lithography is the process used in micro-/nano-fabrication to create structures in materials. In this process the material to be used is covered with a photoactive polymer, called a resist, whose properties change when exposed to light. After dissolving away the exposed (unexposed) regions of a positive (negative) resist, the remaining structure can now be used as a mask for the treatment of the underlying material of interest. For example, if now a metal is evaporated into the structure, the polymer can later be cleaned such that the metal only remains on the previously exposed (for positive resist) or unexposed (for negative resist) areas. This process is called lift-off (see Fig. 3.13).

One of the common techniques used for creating nano-scale structures (<1 µm) is electron beam lithography, in which a beam of electrons is used instead of light to expose the resist. For electron beam lithography (EBL) processes we use polymethyl methacrylate (PMMA), a positive resist.

To write the desired structure the dose of the EBL needs to be calibrated. The dose is given in $\mu C/m^2$, and is calculated taking into account the current and the size of the electron beam. A parameter which is important for the processes at hand is the concept of proximity effect. When writing the structure with the EBL, the backscattered and secondary electrons will also contribute to the final structure. While when writing structures of a large enough size the effect is barely noticeable, there are two opposing cases when it becomes important: exposing a large area leaving a structure inside that area or writing a very small feature. In the former, the dose needs to be reduced since the backscattering electrons will make the effective remaining area smaller than it should. This will be important when writing the etching mask, as explained below. Oppositely, when writing a very small feature, the dose needs to be increased, as the backscattering electrons will barely contribute and the area will be smaller than desired. This will be relevant when etching the top gate to create the narrow junctions.

After exposure to an adequate dose of the electron beam, the sample is developed, a process in which the exposed polymer is dissolved. After developing, the structure is clearly defined and the next fabrication step can be done. The used PMMA is developed using a solution 1:3 of MIBK:IPA (Methyl isobutyl ketone and Isopropanol, respectively).

3.1.7.2 Reactive ion etching In order to shape the stacks into the final shape reactive ion etching (RIE) is used. In this technique the material is both chemically and physically etched. The material is inserted into a vacuum chamber and the chamber is filled with certain gases which chemically react with the material to be etched upon being ionized. An RF voltage is applied to the wafer plate (where the sample is sitting), which ionizes the gas and creates a plasma. In each cycle of the RF oscillation the electrons are moved up and down the chamber. Due to the different weight of the electrons and the ions, eventually a voltage difference is created between the plasma (positively charged) and the wafer (which gets negatively charged by the crashing electrons). This voltage difference will direct the plasma towards the sample, obtaining the desired etched structure.

3.1.7.3 Evaporation Metal evaporation can be done in two different ways: thermal evaporation and electron-beam evaporation. In both cases the material is heated up until it sublimates and the sublimated metal is slowly deposited on the surface of the sample. Whether a material is evaporated with thermal or e-beam evaporation depends on its properties, mainly its melting point. Some materials can be evaporated with both techniques. For the devices used in this thesis the electrical contacts always consist of a combination of chromium and gold. Chromium is evaporated via e-beam evaporation and gold using thermal evaporation.

3.1.7.4 MATBG fabrication process The typical MATBG devices consist of 2 lithography steps: etching the stack into a Hall bar structure and evaporation of the contacts. In order to create the Josephson junction architecture two more steps are needed: evaporation of the top gates and top graphite gate etching to define the weak link between the superconductors. All the steps are shown in Fig. 3.14 and are described next:

1. **Top gate evaporation**. The contacts are usually ∼300 - 500 nm wide and consist of 5 nm of Cr and 50 nm of Au. Chromium is used as an adhesion layer to the SiO_2 and because of its low contact resistance to graphene/graphite, compared to other metals as Ti for example [21]. After the evaporation process the samples are immersed in acetone at 50 °C for a few hours to remove the PMMA and lift-off the undesired metal. Once most of the metal has been lifted, a syringe is used inside the acetone to add extra force which aids the remaining pieces of undesired Au which might still be connected to the sample to break. Finally, the sample is rinsed in IPA and blow-dried with N_2.
2. **Hall bar etching**. The hBN/graphene heterostructures are etched using fluorine gases. We use 40 sccm CHF_3 / 4 sccm O_2 [21] at 30 W, which gives an hBN etching rate of ca. 20 nm/min. In this step the sample is etched all the way down to the SiO_2, leaving only the heterostructure in the shape of the final Hall bar. The Hall bars are

usually defined to be 2-3 µm width with 1-2 µm distance between the contacts. The Hall bar “arms” are usually 1 µm wide. For this process the EBL dose needs to be lower than for the contact writing. If the dose is not calibrated properly, the “arms” become overexposed due to the large exposed area and the final structure will be smaller than desired, which can be detrimental for the contact deposition.

3. **1-D electrical contact to graphene**. In order to get the best contact possible we use the 1D contact technique [21]. This combines an step of RIE followed by metal evaporation, such that the evaporated metal contacts the freshly exposed graphene. By having a specific ratio of hBN/graphene etching rates, a tilted structure is obtained, ensuring the 1D contact to the graphene. Specifically, an etching rate ratio between hBN/graphene of ∼3:1 gives the best results. Then graphene is contacted by depositing 5 nm of Cr and 50 nm of Au. After the evaporation the samples are immersed in acetone at 50 °C for a few hours for the lift off process, as in the top gates case.

4. **Etching the top gate graphite**. Graphite is etched using 50 sccm O_2 plasma at relatively high power (100 W) for a very short time (3-5 seconds) to avoid widening of the features [124]. We have found that this recipe gives a very sharp and clean vertical profile to the etched channel, as previously reported [125]. The obtained channels are ∼ 100 nm long. After etching the samples are put in hot acetone for a few hours. After several hours the samples are moved into a new beaker with fresh acetone and left overnight. Finally, the sample is cleaned in IPA and then blow-dried with N_2. The long acetone cleaning is used to minimize the residues of PMMA left in the etched channel. Opposite to the etching mask, in this case a higher dose in the EBL is used.

3.2 Transport measurements

The main probe used in this thesis for the characterization of the MATBG devices is electrical transport. The idea is simple: current is sent to two contacts of the device and the voltage drop is measured. This voltage measurement is then converted to electrical resistance by dividing the signal by the current. The properties of the material can be mapped by performing these simple resistance measurements changing other external parameters, mainly: current, gate voltage, temperature and magnetic field. From the results of the different measurements one indirectly access the band dispersion, the electronic properties and possible phase transitions in the material.

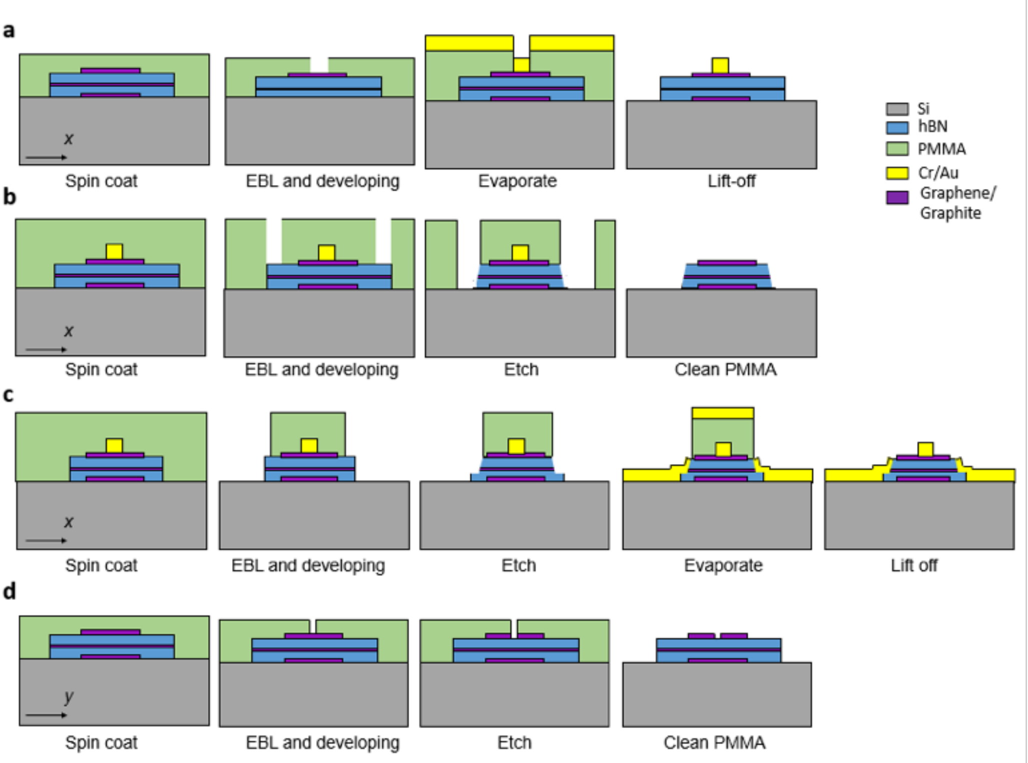

Figure 3.13: Diagram of the nanolithography steps. a Top gate evaporation. **b,** Etching the stack into a Hall bar **c,** Evaporation of 1D contacts. **d,** Etching the top graphite gate. The schematics show the cross section following the axis direction shown in the bottom left of each figure, which refers to the reference frame displayed in Fig. 3.14d.

3.2.1 Low-frequency lock-in techniques

The measurement scheme used in this thesis is what is generally known as the standard low frequency lock-in techniques. The measurements are done exciting the sample with an AC current at a low frequency (below 100 Hz). The response is then measured with a lock-in amplifier which improves the signal to noise ratio by using phase-sensitive detection [126, 127]. The excitation signal is sent at a fixed frequency and the measured response is locked at that frequency by multiplying the input signal with a reference signal at that given frequency and passing it through a series of low-pass filters. This process, called demodulation or phase-sensitive detection, is used to isolate the signal at that given frequency, allowing the measurement of small signals with reduced noise. In the lock-in amplifiers typically used in this thesis (Stanford Research SR860 (or SR830) Amplifiers), the input signal is multiplied by the reference signal plus a copy of it phase shifted

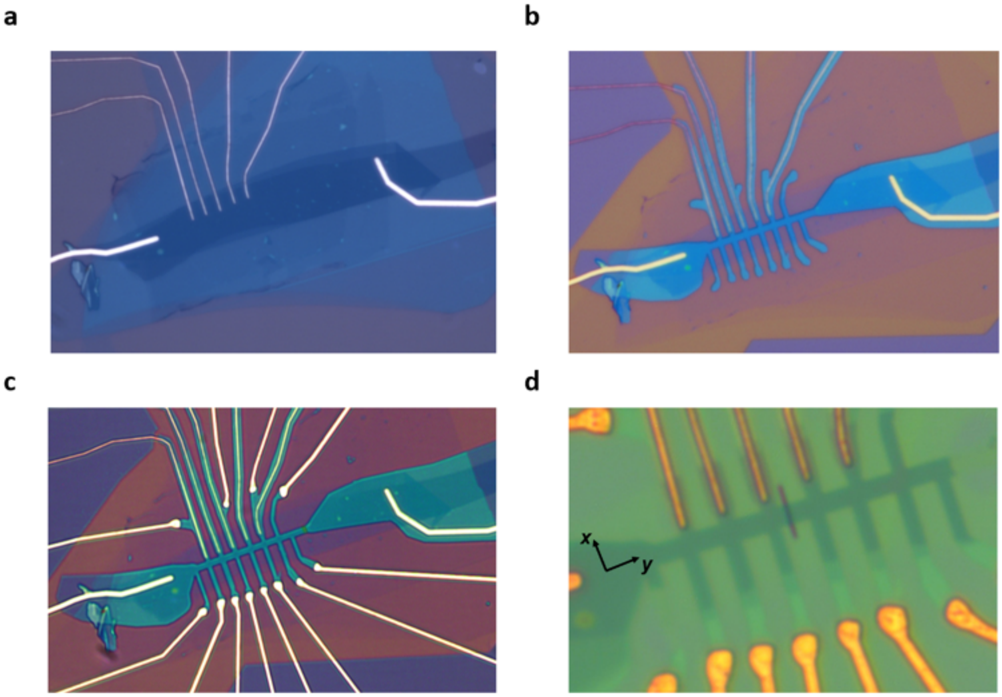

Figure 3.14: Optical images of the different nanolithography steps. a, First the top gates are evaporated. **b,** The stack is then shaped into a Hall bar structure by reactive ion etching. **c,** The 1D contacts are made. **d,** Finally the top gate is etched to create the junction. The green color comes from the PMMA used in the lithography. The dark line is the etched region. The picture is shown with PMMA, to highlight the position and shape of the etched region, which is otherwise not visible. The reference frame marks the direction from which the cross sections shown in Fig. 3.13 are taken.

by 90°, making a dual-phase demodulation. The output signal has then two channels: X and Y, corresponding to the in-phase and out-of-phase response. The total amplitude R and the phase θ are then obtained as:

$$\begin{aligned} R &= \sqrt{X^2 + Y^2} \\ \theta &= \arctan(Y/X) \end{aligned} \tag{3.1}$$

3.2.2 Cryostats and filtering

To measure the exotic properties of MATBG the material needs to be cooled down to cryogenic temperatures. The energy scale of the effects one can measure is limited by the thermal noise $\propto k_B T$, which is on the order of 25 meV at room temperature ($T \approx 300$ K). Both the band width of the flatbands of MATBG and the energy gaps separating it from the dispersive bands, are on the order of tens of meV. That implies that to access the isolated flat bands the material needs to be cooled down enough such that thermally excited transitions from the flatbands to the dispersive bands are suppressed. Furthermore the states inside of the flatband have smaller energy scales, which can go down to the order of ~ 1 meV. The lower the T the sharper the states will become, since the thermal noise is reduced and spontaneous transitions between states, which average out the signals, are further suppressed. Finally, some of the correlated states we are looking for have a very low transition T, for example, the superconductivity is suppressed for $T > 1$ K or lower depending on the device. Therefore, performing the measurements at the lowest possible T will result in the best quality data which reflects the nature of the ground state of the system, ultimately leading to a better understanding of the phenomena.

Cryostats can be classified as “wet” or “dry”, depending whether they use liquid cryogens (like He) or not. In our case, the fridges are dry, using compressed He to cool down. We will distinguish between two types of dry fridges: variable temperature instrument (VTI) and dilution fridge. In both cases the T down to 4 K is achieved in the same manner, a cold head is used to pump He through a circulation line, in which the system can cool down without liquefying the He by reducing the He pressure. In order to isolate the coldest part from the room temperature ambient, the fridge have stages at different T, separated from each other by radiation shields. In the VTI these stages are 50 K and 4 K, while in the dilution fridge they are 50 K, 4 K and 1 K. The main difference between the two fridges is the way they achieve their lowest T and, of course, the value of this lowest T, as is explained below.

3.2.2.1 Variable Temperature Insert (VTI) In this type of system the sample is introduced with a loading stick inside a chamber filled with He gas. This chamber is then surrounded by a second chamber through which He is flushed, by pumping it from one end to the other. The sample sits at the bottom of the first cavity, just above where the second cavity has a needle valve, which will control the flow of pumped He. By using a cold head the system can cool down to 4 K without using liquid He. Then, by reducing the pressure of He down to few mbar, the T can be further lowered down to 1.4 K (see Fig. 3.15a). The minimum T is achieved by ensuring that the pumping and the needle valve value maximizes the ratio between the liquid phase that forms at the bottom of the needle valve and the evaporation of it caused by cooling down the sample stage. If too much or too little flow comes in, the thermal exchange is reduced and the minimal T is not achieved.

3.2.2.2 Dilution fridge A dilution refrigerator is used to achieve T in the mK range. In our case the base T of the fridge is ca. 35 mK. These extremely low T are achieved by having a phase mixing of He-3 and He-4. The dilution refrigerator takes advantage of the phase separation that occurs between He-3 and He-4 at very low T. The phase separation arises because He-4 obeys bosonic statistics, while He-3 follows fermionic statistics (unless cooled down to much lower T). As the system is cooled down and the two isotopes are together, below a $T \approx 0.8$ K, the two isotopes will separate creating a He-3 rich phase and a mixed phase (see Fig. 3.15b). Since He-3 is lighter, the separation also occurs in space, leaving the He-3 rich phase on top and the dilute phase on the bottom. When cooling further the allowed concentration of the mix changes continuously, reducing the concentration of He-4, until a minimum point of 6.4 %. If once the mix is made, one can selectively remove the He-3 isotope, the He-4 will be forced to create more dilute phase. This is the key parameter, since the cooling power of the dilution fridge is then given by the enthalpy difference of the He-3 in its diluted or pure phase, multiplied by the flow.

The separation of the phases can be achieved by having two chambers, the mixing chamber and the still chamber, which take advantage of the spatial separation of the two phases to selectively remove He-3 atoms. This is shown in Fig. 3.15c. A pump is used to circulate the gases between the two chambers, which are built in such a way that in the mixing chamber only the He-4 can escape and in the still chamber only the He-3 can escape. In the mixing chamber this is achieved simply by geometry while in the still plate a heater is used to have a T in which the vapor pressure of He-3>He-4, ensuring that He-3 remains on top. By controlling the flow, the phase boundary is controlled which gives the optimal cooling power of the fridge, to achieve the lowest possible T.

3.2.2.3 Filtering: cooling down the electrons The last important component to measure electronic properties at very low T is to also cool down the electrons taking part in the electrical measurements. If this is not done, the T of the measurement will not be the T of the fridge, but rather a much higher T induced by the incoming hot electrons. The cooling is done, firstly, by physically thermally anchoring the wires to the different stages of the fridge (50 K, 4K, 1 K) and, secondly, by filtering. Since the measure-

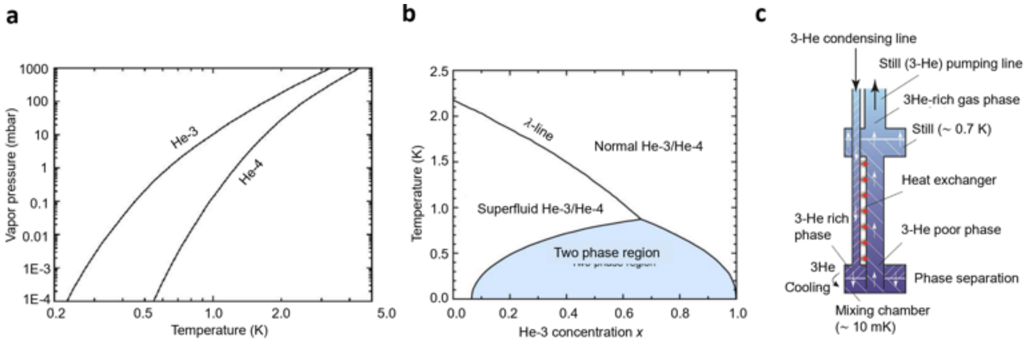

Figure 3.15: Working principle of a dilution refrigerator. a, Behavior of He-3 and He-4 with vapor pressure and T. **b,** Phase separation between He-3 and He-4. **c,** Working principle of the mixing chamber shown as a diagram (on the left) and on a real device (on the right). Figure modified from [128].

ments are performed at very low frequencies, filtering higher frequencies will effectively cool down the electrons without affecting the measured signal. The electronic T is related to the frequency ν by $h\nu = k_B T$, such that to cool down to 35 mK the frequency needs to be cut off at ca. 730 MHz. The necessary attenuation (A) to cool down to a certain T can be calculated using the following formula [129]:

$$A(\nu) = \frac{e^{\frac{h\nu}{k_B T}} - 1}{e^{\frac{h\nu}{k_B T_c}} - 1}, \tag{3.2}$$

where T_c is the objective temperature and T is the temperature of the hot reservoir. By using this equation one can calculate which kind of filtering is needed to obtain the desired electronic T for the experiment. In general a combination of low-pass RC and LC filters is used for this purpose. In our dilution fridge, commercially available filters from QDevil are used. Having a 65 MHz RC filter at the 1 K stage and a 225 MHz LC filter at the mixing chamber.

3.2.3 MATBG measurement protocol

A final note is added here to explain the protocol followed to measure the MATBG devices. Due to the fragile nature of the fabrication, the aimed angle during the stacking does not always correspond to the obtained angle. Therefore the devices are screened in order to only cool down and measure in detail the ones which are promising. The protocol consists of three parts: room T measurements, angle extraction at low T and actual measurements.

3.2.3.1 Room T measurements: vacuum probe station After the fabrication of the devices, the 4-terminal resistance (R_{xx}) as a function of back gate voltage V_g is measured at room T to distinguish close-to-magic-angle devices before loading in a cryostat. There are two main features which distinguish potentially good devices from devices which have relaxed to Bernal bilayer graphene (BBG) or to a low twist angle ($\theta < 0.7°$), as shown in Fig. 3.16: the shape of the R_{xx} vs. V_g dependence and the nominal value of the $R_x x$. Typical BBG devices have a very sharp decay after charge neutrality point (CNP), while twisted devices have a flatter dome due to the presence of band insulators. The band insulators in the electron and hole sides tend to have different resistance values, which results in a tilted dome-shaped curve at room-temperature, i.e. $R_{xx}(V_g < 0) < R_{xx}(V_g > 0)$ as in Fig. 3.16a. However, the thickness of the hBN needs to be known to properly compare the behavior. A MATBG device with a thin hBN might look like a BBG device at high enough voltages, while a BBG device with a thick hBN might look like a MATBG device if not enough voltage is applied. Finally, MATBG devices have a higher R_{xx} than BBG or low angle devices due to the flat band. A $R_{xx} > 10$ kΩ, combined with the previous measurement indicate towards a potentially good device. However, devices with a large twist angle ($1.3° < \theta < 1.8°$) or with inhomogeneities are indistinguishable from good devices at room T. This means that there will always be some devices with undesired twist angles which end up being cooled down for measurements.

3.2.3.2 Angle extraction The twist angle is one of the most distinct features of a magic-angle graphene device. The angle is extracted by the relation between the superlattice carrier density n_s and the twist angle θ which was shown in eq. 2.20:

$$n_s = 4/A \approx \frac{8\theta^2}{\sqrt{3}a^2} \tag{3.3}$$

where A is the area of one moiré cell and a is the graphene lattice constant. The first step is to extract the gate capacitance C_g, to convert the back gate V_g data to carrier density, using $n = \frac{C_g}{e}V_g$. Then an accurate definition of n_s in the data has to be given.

The capacitance is obtained by doing magnetotransport measurements. It can be obtained by two different methods: either using R_{xx} or R_{xy} data (shown in Fig. 3.17):

- **Landau level quantization**. When subjecting a 2D sample to a

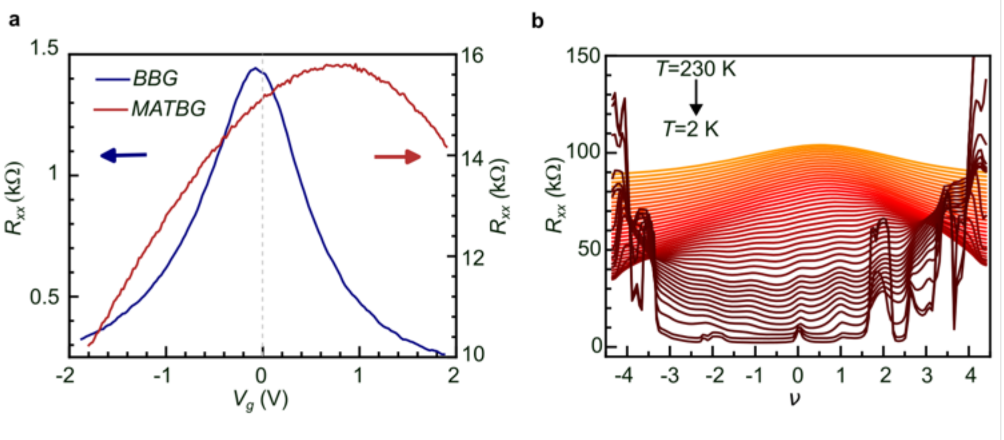

Figure 3.16: Screening the TBG devices at room T. a, Room T measurement comparing a Bernal bilayer graphene (BBG) and a magic-angle twisted bilayer graphene (MATBG) device with twist angle $\theta = 1.04 \pm 0.02°$ shown in the blue and red curves, respectively. The asymmetry of the dome, combined with the 4-terminal resistance (R_{xx}) value allows to distinguish between the two. hBN of comparable thicknesses ($d \approx 15$ nm) are used in both devices. **b,** Cool down curves of the MATBG shown in **a** from $T = 230$ K down to $T = 2$ K. The curves are shifted by 1 kΩ starting from the lowest T for clarity.

magnetic field, the electrons form quantized cyclotron orbitals (Landau quantization), which gives rise to the appearance of so-called Landau levels [130]. The density of states in the Landau levels is given by $n_{LL} = \nu eB/h$, where ν is the degeneracy of the levels, which is material dependent. In the case of graphene there is a 4-fold degeneracy, due to the spin and valley flavors [6]. In MATBG the degeneracy should in principle be doubled at CNP, showing a series of Landau levels as ±4, ±12 ±20.... However the measurements show a 4-fold degeneracy with the sequence: ±4, ±8, ±12...[122]. The degeneracy also changes when filling the flat band, as there are band-resets at certain integer fillings [131, 47, 46]. This leads for example to a two-fold degeneracy after half-filling. As the density of states in a Landau level is constant with increasing field, one can use the slope of the Landau level $\Delta B/\Delta V_g$ to obtain the capacitance of the sample:

$$\begin{aligned} \Delta n &= \Delta V_g \frac{C_g}{e} = \frac{e}{h}\nu \Delta B \\ C_g &= \frac{\Delta B}{\Delta V_g}\frac{e^2}{h}\nu \end{aligned} \tag{3.4}$$

- **Hall effect**. Another way to calibrate the carrier density is to use the Hall effect at low fields ($B < 1$ T) [44]. Close to the CNP, the Hall carrier density $n_H = -B/(eR_{xy}) \approx n$, such that the slope $\frac{\Delta n_H}{\Delta n} = 1$ or $\frac{\Delta n_H}{\Delta V_g} = \frac{e}{C_g}$. In order to calculate n_H, R_{xy} is antisymmetrized to avoid artifacts arising from R_{xx}-R_{xy} signal mixing due to geometric effects.

After obtaining the capacitance, the position of n_s needs to be determined. Since the dispersive bands in MATBG also develop Landau levels, the position of n_s can be obtained as the origin of the Landau levels emerging from the band insulator position. However, for some devices these Landau levels can be weak or the BIs can be broad, not allowing the Landau levels to be clearly seen. Another way to find this position is to use the position of an integer filling of the flat band and multiply it by the proper constant to obtain n_s. For example, one can extract $n_{1/2}$ from the position of the Landau levels of the $\nu = 2$ CI, and obtain $n_s = 2n_{1/2}$. Finally the angle is obtained using the expression of eq. 3.3. Since the Landau quantization only appears at low T, these measurements are performed either in the VTI or the dilution fridge.

In summary, the complete protocol to screen MATBG devices from the stacking to the measurements to ensure only close to magic-angle and homogeneous devices are measured would be as follows:

- **Stacking**. Only stack with pristine initial flakes and ensure the stacking process is “clean”: no jumps, folds, etc.

- **Nanofabrication**. Once the stack is finished, only fabricate the device in a bubble free area (which can be confirmed with an AFM image). Carefully design the device to optimize the number of contacts and top gates.

- **Room-T screening**. Load the device in a vacuum probe station and check the shape of the gating dome and the resistance.

- **Initial characterization**. Load the device in a cryostat (ideally a fast cooling one, a VTI in our case), measure R_{xx} vs. V_g and extract the twist angle. If the device is close to magic-angle, measuring R_{xx} vs. V_g vs. T can already indicate if the sample might become SC, depending on the T of the fridge being used. In our case, this step is used to decide in between which pairs of electrodes to perform the graphite etching to create a junction.

- **Final measurements**. Load the device in a dilution fridge and do the final measurements.

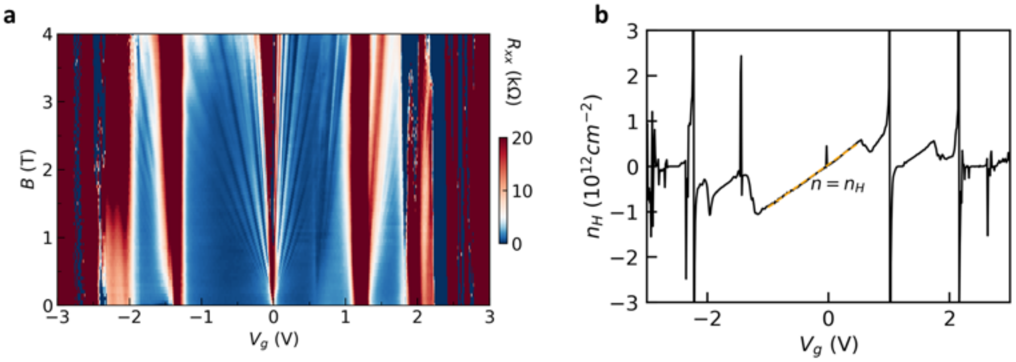

Figure 3.17: Twist angle extraction methods. a, Longitudinal resistance R_{xx} vs. back gate voltage V_g vs. perpendicular magnetic field B. By fitting the Landau levels one can extract the gate capacitance, used to calculate n and the twist angle. **b,** Calculated Hall density n_H vs. V_g. In the region around charge neutrality $n = n_H$. The measurement is taken at $B = 500$ mT.

4 Junction Design and Optimization

In this section the optimization of the gate-defined Josephson junctions fabrication is explained, highlighting the importance of certain parameters. The optimization process is mostly reflected in considerations about the stacking process as well as some design improvements for the nanofabrication. These include optimizing the designs to have as many gates a possible to increase the chances of having a superconducting region in the MATBG device and being able to have more than one junction per device and the optimization of the top graphite gate etching. The section is divided in three parts: electrostatic simulations, the optimization of stacking and fabrication of the dual gated devices and the graphite etching recipe calibration and optimization.

4.1 Electrostatic simulations

In order to gain insight on how the electrostatics of the dual gated architecture of our device works (see Fig. 1.5), we have performed electrostatic simulations by solving the Poisson equation with a finite difference method (FDM) [132]. The Poisson equation can only be solved analytically for very simple models, in order to solve a real geometry one needs to use numerical methods. A typical way to solve this is by using the FDM, in which the equations are discretized, converting the problem into a system of linear equations, such that one can solve it via matrix inversion. The approach is done following the work of [133].

The generalized Poisson equation is given by:

$$\nabla \cdot [\epsilon(\boldsymbol{r})\nabla V(\boldsymbol{r})] = \rho(\boldsymbol{r})/\epsilon_0, \tag{4.1}$$

where ϵ is the dielectric constant ($\epsilon \approx 4$ for hBN), V is the electrostatic potential, ρ is the density of electric charges and ϵ_0 is the vacuum permittivity.

To numerically solve the equation, the system to be studied (double gated MATBG encapsulated in hBN) is first discretized in the form of a 2-dimensional grid, such that $x = ih$ and $y = jh$, with h the distance between the points and i and j the discretized values of x and y (see Fig. 4.1a). The total size is given by N_x and N_y. Each of the points in the grid is assigned a potential value given by $V(i, j)$. When solving the equation we assume that the potential at each point is dependent on the potential of the 4 adjacent points plus its initial charge ρ, such that:

$$\begin{aligned}V(i,j) =& 1/4[V(i-1,j)+V(i+1,j)+V(i,j-1)\\&+V(i,j+1)+\rho(i,j)h^2/\epsilon_0].\end{aligned} \tag{4.2}$$

The discretized problem is then converted into a matrix and can be solved by matrix inversion. However, only very small dimensions can be solved by inverting the matrix, while large systems need to be solved by an iteratively: an initial guess for V is given and the problem is solved iteratively until convergence is achieved by having the difference between two iterations smaller than a given threshold:

$$error = V^{k+1}(i,j) - V^k(i,j) < \text{threshold}, \tag{4.3}$$

where k is the iteration number. In this case we use a successive over-relaxation method due to its high computational performance [134]. The successive over-relaxation method works as a Gauss-Seidel approach in which a weight is given to accelerate the convergence. An initial guess of $V^0(i,j) = 0$ is given and the problem is solved iterating the residuals $R^k(i,j)$ instead of the potentials:

$$\begin{aligned}\text{For } k=1 \rightarrow R^k(i,j) =& 1/4[V^k(i-1,j)+V^k(i+1,j)\\&+V^k(i,j-1)+V^k(i,j+1)+\rho(i,j)h^2/\epsilon].\end{aligned} \tag{4.4}$$

The potential for the next iteration is calculated by:

$$V^{k+1} = V^k(i,j) + wR^k(i,j), \tag{4.5}$$

with $0 < w < 2$, where w is the chosen weight. From the next iteration, the process is accelerated by adding the newly guessed solution:

$$\begin{aligned}\text{For } k\geq 2 \rightarrow R^k(i,j) =& 1/4[V^{k+1}(i-1,j)+V^k(i+1,j)\\&+V^k(i,j-1)+V^k(i,j+1)+\rho(i,j)h^2/\epsilon_0],\end{aligned} \tag{4.6}$$

until the problem converges such that the error is smaller than the defined threshold, as shown in eq. 4.3. For a rectangular mesh the weight is calculated as:

$$w = \frac{9-\sqrt{64-16t^2}}{t^2}, \quad \text{with} \quad t = \cos\frac{\pi}{N_x} + \sin\frac{\pi}{N_y}. \tag{4.7}$$

Once the potentials are known one can calculate the discrete electric fields:

$$
\begin{aligned}
E_x(i,j) &= -\frac{V(i+1,j)-V(i-1,j)}{h} \\
E_y(i,j) &= -\frac{V(i,j+1)-V(i,j-1)}{h},
\end{aligned}
\tag{4.8}
$$

Since the fields are calculated as a difference, the result is a staggered matrix with the fields being at different places than they should (see Fig. 4.1b). This has to be corrected for to obtain the right mesh:

$$
\begin{aligned}
E'_x(i,j) &= 0.5[E_x i, j+1 + E_x(i,j)] \\
E'_y(i,j) &= 0.5[E_y(i+1,j) + E_y(i,j)] \\
E_{total} &= \sqrt{(E'^2_x + E'^2_y)}.
\end{aligned}
\tag{4.9}
$$

All the ingredients to solve a discretized Poisson equation have now been defined. However, to solve the real problem at hand, we need to add the dielectric constant of the different materials, mainly air and hBN. The dielectric constants of the different materials are added as a staggered matrix relative to the original one such that $\epsilon(i,j) = \epsilon(x_i + h/2, y_j + h/2)$ as shown in Fig. 4.1b. Defining it this way allows to calculate potentials at the boundary of different materials with different dielectric constants. With the newly defined ϵ matrix we have to recalculate the residuals in order to calculate the potentials. In this case, the process to obtain the final equation is more complicated and the derivation is not included here (see [134] or [133] for reference). The final solution for the potentials and residuals are given as:

$$
\begin{aligned}
V(i,j) =& \frac{1}{a_0}[a_1 V(i+1,j) + a_2 V(i,j+1) \\
&+ a_3(i-1,j) + a_4(i,j-1) + \frac{Q(i,j)}{\epsilon_0}] - V(i,j) \\
R(i,j) =& \frac{1}{a_0}[a_1 V(i+1,j) + a_2 V(i,j+1) \\
&+ a_3(i-1,j) + a_4(i,j-1) + \frac{Q(i,j)}{\epsilon_0}] - V(i,j),
\end{aligned}
\tag{4.10}
$$

where $Q(i,j)$ is the charge at a given position and a_0, a_1, a_2, a_3 and a_4 as defined as:

$$\begin{aligned}
a_0 &= \epsilon(i,j) + \epsilon(i-1,j) + \epsilon(i,j-1) + \epsilon(i-1,j-1) \\
a_1 &= 1/2[\epsilon(i,j) + \epsilon(i,j-1)] \\
a_2 &= 1/2[\epsilon(i-1,j) + \epsilon(i,j)] \\
a_3 &= 1/2[\epsilon(i-1,j-1) + \epsilon(i-1,j)] \\
a_4 &= 1/2[\epsilon(i,j-1) + \epsilon(i-1,j-1)].
\end{aligned} \tag{4.11}$$

The problem can now be solved as before using eq. 4.5.

Since the problem needs to be finite in order to be solved, boundary conditions (BCs) have to be added to the system. The BCs are generally either Dirichlet or Neumann like. Dirichlet BCs give a certain value at the boundary f, defining a clear contour in which the value of the potential is set, such that:

$$V(\mathbf{r}) = f(\mathbf{r}) \text{ for } \mathbf{r} \in \Omega_C, \tag{4.12}$$

where Ω_C defines the contour at which the BCs are given. On the other hand, Neumann BCs are defined as a derivative, such that the value of the potential has a given decay, i.e.:

$$\frac{\delta V(\mathbf{r})}{\delta \mathbf{n}} = f'(r) \text{ for } \mathbf{r} \in \Omega_C, \tag{4.13}$$

where $\mathbf{n}$ is the vector normal to the surface and f' is the value of the known derivative.

4.1.1 Defining the problem

The region of interest of our simulations is the area around the junction, which consists of a back gate defined by a metal electrode, two hBN sections, the twisted bilayer graphene and two top gates separated by a narrow gap. The simulations are used to understand how the junction will behave and to optimize it in terms of hBN thickness and the width between the top gates. Since we are just interested in the shape of the potential at the MATBG position, we do not define the graphene explicitly. A more complex simulation including the graphene chemical potential could be done, but it lies beyond the scope of what is done in this work. For an example including the graphene chemical potential one can refer to the supplementary material in Rodan-Legrain *et al.* [135]. The simulations are used to find out the best architecture based on the following parameters:

- **Top and bottom hBN thickness ratio.** As the structures are made

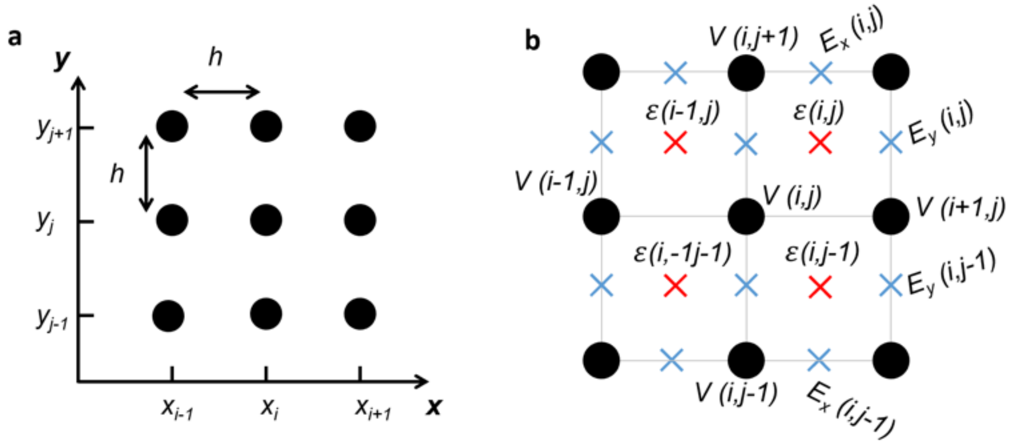

Figure 4.1: Discretizing the Poisson equation. a, The coordinates as written as discretized into a grid in x and y. **b,** Grid showing the potentials V in the same lattice as the initial positions while the electric field E (blue crosses) and the dielectric constant ϵ (red crosses) are defined as staggered lattices.

by stacking the materials, if the thickness ratio limits the efficiency of the junctions the whole device could be compromised if the hBN thicknesses are selected incorrectly.

- **Size of the junction.** In order to have a working JJ the size of the junction d_J needs to be of the same order of magnitude of the coherence length of the SC [58] of ca. 100 nm. Since the junction is gate-defined, the shape of the potential will matter, giving a real size which is not the same as the defined size.
- **Global hBN thickness.** We want to study whether having different total hBN thicknesses changes the shape of the potential.

We first define a constant spacing between the top gates, i.e. 100 nm, and do simulations having a constant bottom hBN and varying the thickness of the top hBN. Then we fix the hBN ratio and change the size of the gap between the gates. Since the resulting potential is dependent on both the hBN thickness and the size of the gap due to the shape of the stray fields [136], simulations are done changing both parameters. Finally, these two variables are kept constant and we change the overall thickness of the hBN. Apart from these two dimensions the rest of the parameters are always defined similarly. The electrodes are defined with Dirichlet BCs: $V\ (z = z_{top}) = V_{TG}$ and $V\ (z = z_{bottom}) = V_{BG}$. The sides and top regions with no gate are set with Neumann BCs, satisfying $\delta V_x = 0$ and $\delta V_y = 0$, respectively.

The value of the potentials of the different gates is set as $V_{TG} \neq V_{BG}$ to define junctions at different carrier density n.

4.1.2 Finding the right hBN thickness ratio

A junction with a separation of 100 nm is defined in the top gate and the structure is defined to have a constant bottom hBN thickness of $t_{hBN,bot} = 14$ nm (as this is generally used for the stacking). The thickness of the top hBN is varied between $t_{hBN,top}$ =7 ,14 and 21 nm. The voltage of the back gate is set to $V_{BG} = 1$ V and $V_{TG} = -1.5$ V multiplied by the ratio of the hBN thickness to correct for the different gating strength: $V_{TG} = -1.5 \times t_{top}/t_{bot}$ V. The electric potential and fields are calculated and plotted in Fig. 4.2a and b, respectively, for a configuration of $t_{top} = t_{bot}$. The results for the potential at the MATBG position are shown in Fig. 4.2c. The results show how the thinner hBN gives a potential with a sharper boundary, but with smaller contrast, i.e. the difference between the global area and the junction is smaller. This can be understood because for thinner top hBN, stray fields play a smaller role, thus defining a sharper junction, but, at the same time, the effect of the bottom gate is reduced as the graphene sits closer to the top edge and top gates.

4.1.3 Effect of the top gate gap

Now we analyze how the separation between the top gates d can be optimized to have the best gating in the junction by first setting a constant hBN thickness and changing d the size of the junction and then changing both variables together. We simulate the same hBN ratios as before, but having a gap of 200 nm between the top gates. Fig. 4.2d show how the larger d gets, the junction is better defined for different $t_{hBN,top}$ (keeping $t_{hBN,bot}$ constant).

4.1.4 Effect of the global hBN thickness

Finally we check the effect of the global hBN thickness by varying the thickness of the bottom hBN and performing again the previous comparisons. This is to study the effect of the overall hBN thickness on the shape of the electrostatic potential. We observe the junctions are much better defined independently of the hBN ratios when using thinner hBN (see Fig. 4.3).

From the simulations we conclude that to enhance the quality of the junctions we want to choose sufficiently thin hBN layers and make the junctions as wide as possible. The junction size will be limited by the superconducting

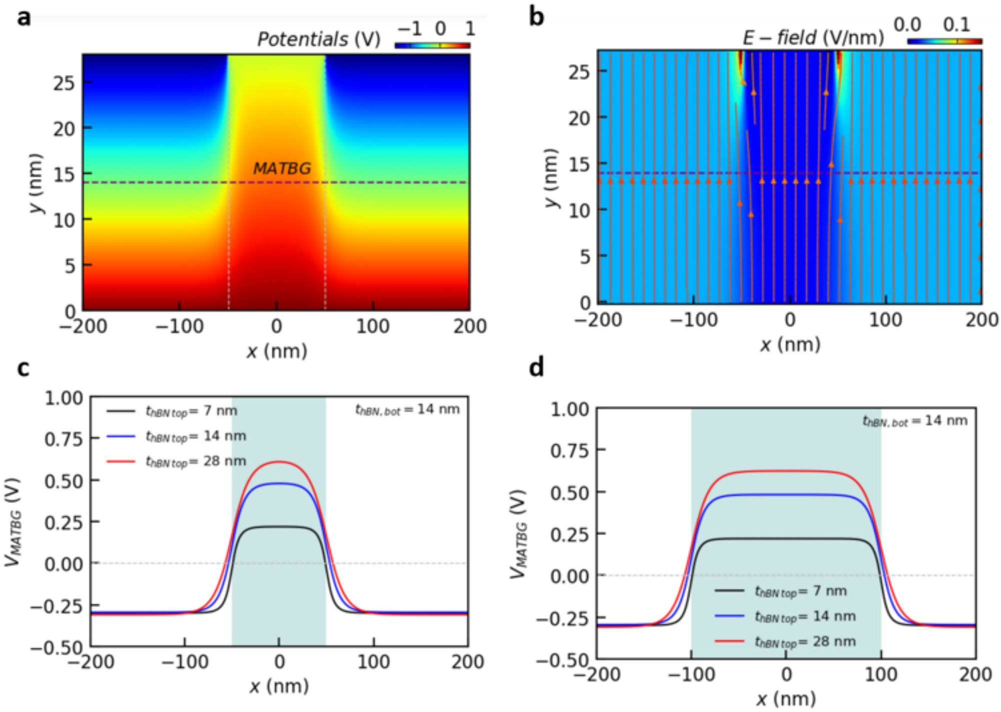

Figure 4.2: Electrostatic simulations of different hBN thickness ratio. a, An example of the solved potentials around the area of the junction. The bottom electrode (in red) is set to $V = 1$ V and set to $V = -1.5$ V. The dashed purple line corresponds to the position of the MATBG. **b,** The electric fields profile of the same simulation. The arrowed lines are the field lines. **c,** Comparing the definition of the junction for different top hBN thicknesses. The $V_{BG} = 1$ V for all, while $V_{TG} = -1.5 \times t_{top}/t_{bot}$ V. **d,** Comparing the definition of the junction for a larger junction size. The rest of the parameters are the same as in **c**.

coherence length of $\xi \approx 50 - 100$ nm, such that we will aim for junctions of ca. 100 nm, to ensure that the central part is proximitized. On the other hand we will aim to have the top and bottom hBN to have around the same thickness or the top hBN slightly thicker to improve the junction resolution. As is explained in Ch. 5, the final real junction size will depend on each device due to the gating profile. The actual junction will be defined by the carrier density of the MATBG which is SC or not.

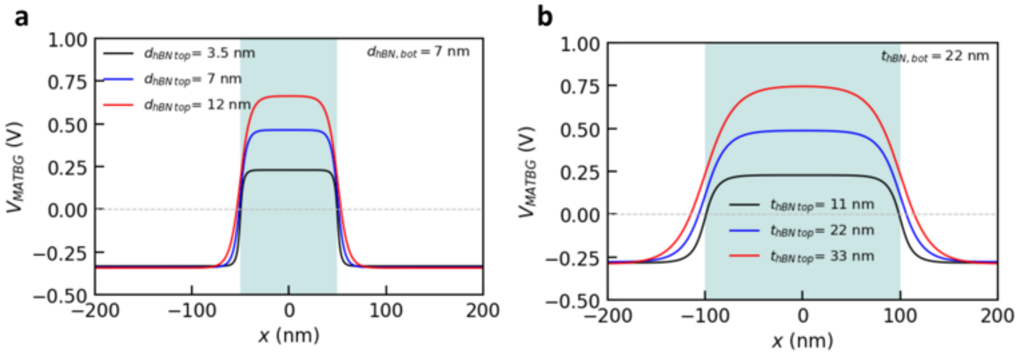

Figure 4.3: Electrostatic simulations at different global hBN thickness. a-b, Comparing the definition of the junction for thinner and thicker general hBN layers, respectively.

4.2 Optimization of the dual-gated device

Due to the nature of the stacking process, the way the materials are stacked influences the types of devices that can be made during the lithography process. In the methods section, some general considerations of the stacking process have been discussed. In this section key considerations specific to the dual-gated devices are explained. Some of the ideas were optimized from the beginning while others were realized iteratively with feedback from the fabrication of the devices. A section discussing the evolution from the initial designs to the final designs will point out exactly the limitations of the initial designs.

4.2.1 Top gate - Back gate widths

As pointed out in the previous chapter, the size of the graphite gates will never be exactly the same, which implies one has to consider both the relative length and the width of the gates. The width is specially important in the case of MATBG due to the existence of highly resistive states (BIs and CIs) in the phase space. A double gated device (in the shape of a Hall bar) can be divided into three distinct regions depending on how they are gated: gated by both gates, gated by the wider gate and gated by the *Si* gate (see Fig. 4.4). The area where the device is defined will be gated by both the graphite gates. The area gated only with the *Si* gate is the area where the contacts are made and it generally only plays a role to decrease the contact resistance at high magnetic fields. Finally, the area gated only by one graphite gate can become very critical. The resistive states (mainly the BI but also some

CI) can be quite insulating (∼MΩ), such that the current on the device can drop close to zero as the input impedance approaches the output impedance (i.e. a series load resistor used to define an effective output impedance of a lockin amplifier). This means that even when the singly gated region is small in area it can completely alter the measurements.

This is observed for example, when performing back gate vs. top gate resistance maps (see Fig. 4.4c). The figure shows two very distinct features, some that depend on both gates (diagonal features) and some that depend only on the top gate (vertical features). The vertical features come only from the region where the two gates do not overlap. It is clear that the system becomes so insulating at CNP and at the BIs positions, that no signal is recorded in those regions. Now is the interesting part: if the insulating signal comes from the top gates, the Si gate can be used to gate it into a less resistive states, allowing to measure the regions of interest. If the insulating states arise from the back gate, nothing can be done, as the electric field from the Si gate will be screened by the back gate (as illustrated in Fig. 4.4a and b). Therefore if the top gates are wider than the back gate, the signal from the arms can be gated away in order to obtain proper data.

4.2.2 Top hBN size relative to graphene

It has already been explained how the hBN flakes always need to extend beyond the gates and the graphene to avoid electrical contact between them. However, in that architecture, it is possible to have the graphene be the same size as the top hBN, being completely “clamped” by it. This is not possible when having a top gate. The top gate needs to be electrically connected with evaporated electrodes. These electrodes will go over the top hBN and if the graphene sticks out, this will short the graphene to the top graphite gate. Therefore, it is essential that at least one side of the hBN is free of any graphene. This becomes more important in the case of creating junctions, since at least two contacts are needed.

The approach we employed in this thesis was to optimize the devices by creating as many junctions as possible, i.e. one junction per set of contacts. When adding gate contacts along the whole device (as in Fig. 4.4), one needs to consider they cannot cross the actual device contacts, thus limiting the geometry of the device. The best way to solve the issue is to stack in such a way that the graphene is “clamped” at the top edge while all the other sides are fully covered by hBN. This way the gate contacts can be done alternatively on each side of the device without shorting the gate to the graphene, making the designing and fabrication easier. An example of this is

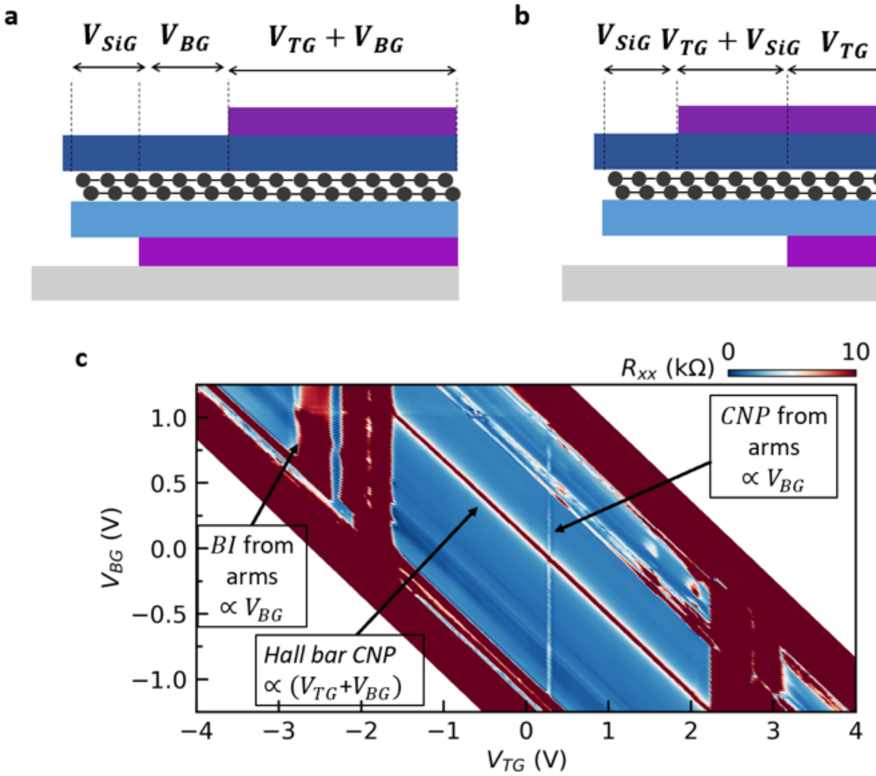

Figure 4.4: Effect of the width ratio between top and bottom gates. V_{SiG}, V_{BG} and V_{TG} represent the regions gated by the silicon gate, the back gate or the top gate, respectively. **a,** Back gate is wider than top gate. There is a region where the back gate will screen the Si gate, creating extra features which cannot be removed. **b,** Top gate is wider than back gate. The extra region could now be removed by using the Si gate. **c,** An example measurement in the case of the back gate being wider than the top gate.

shown in Fig.4.5 which compares the dropped stack and the final fabricated device for a case with gates on both sides (in b) or just one side (in d). An issue in the latter case was that due to the high density of top gates on one side, some contacts needed to be sacrificed, having all the contact pairs on only one side of the device, and thus loosing some R_{xy} signals.

4.3 Optimizing the graphite etching

The final step in the fabrication of the MATBG gate-defined junctions is to etch a narrow channel in the top graphite gate which effectively creates the junction. As we have seen in the electrostatics simulation, the shape of the

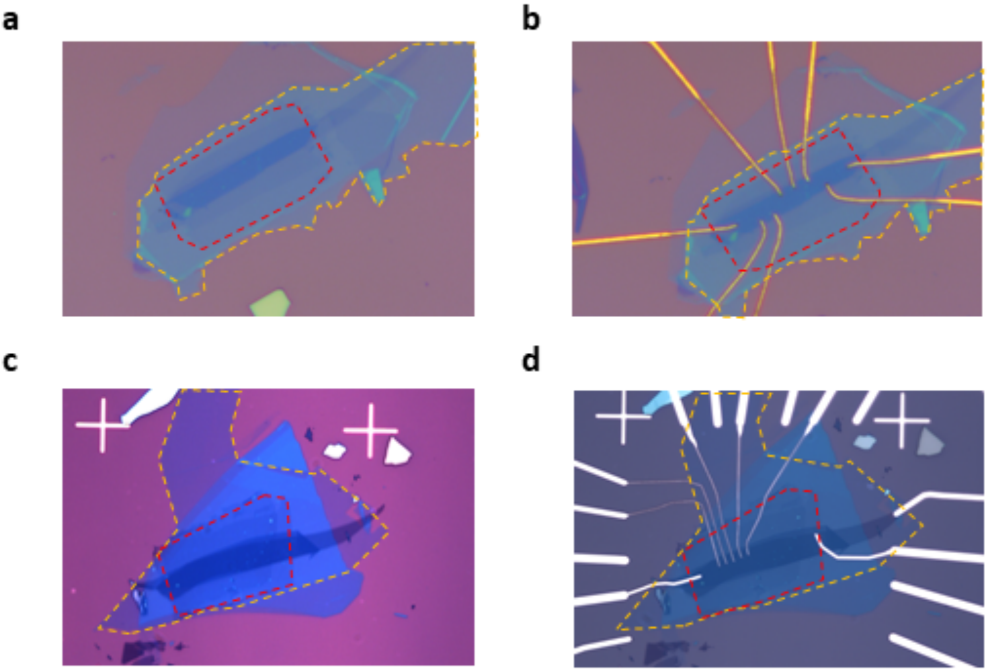

Figure 4.5: Top hBN vs. graphene sizes and encapsulation. a-b, The top hBN fully encapsulates the graphene except for a “clamp” on one corner (marked by a red arrow), which allows to deposit top gates from many different orientations without making shorts. **c-d** The edges of the graphene are “clamped” on a whole side of the hBN. This allows to deposit top gates only from one side, limiting the fabrication, since less contacts can be made.

defining potential is key to obtain a clean junction. That is also why graphite was chosen as the top gate, since it can improve the quality of the devices [137, 138]. Therefore, one of the most important steps in the fabrication is the etching of the top gate to obtain a very clean graphite junction. The channel is made using reactive ion etching. In general, graphene is etched with O_2 plasma, which chemically reacts with the C and can be combined with Ar to add a physical component to the etching [124]. Two main approaches were tried, using a combination of Ar and O_2 and using only O_2. In the end, the pure O_2 recipe proved to give the best results.

The recipes are calibrated on graphite exfoliated flakes on SiO_2. After exfoliation, an EBL design was made to emulate the actual trenches which will be made in a real device. After the EBL step, the sample is cold developed at ca. 10 °C for 50 s in MIBK:IPA (1:3), rinsed in IPA and blow dried with N_2. After the sample is etched, it is introduced in hot acetone for a few hours and then left in clean room temperature acetone overnight to increase the cleanliness inside the etched region. Afterwards, the sample is rinsed in IPA and blow dried with N_2. Finally, the sample is annealed in vacuum for 3h at 300 °C in order to remove the polymer residues. The annealing is done to have a cleaner surface which results in better contrast in the AFM images (annealing is not performed on the actual devices). As is visible in the images of Fig. 4.6, even after annealing the region inside the junction has some residues. The residues can be further improve by using higher doses in the EBL, which keeps reducing the size of the PMMA chains and ease its cleanliness. However, removing all the residues is rather challenging.

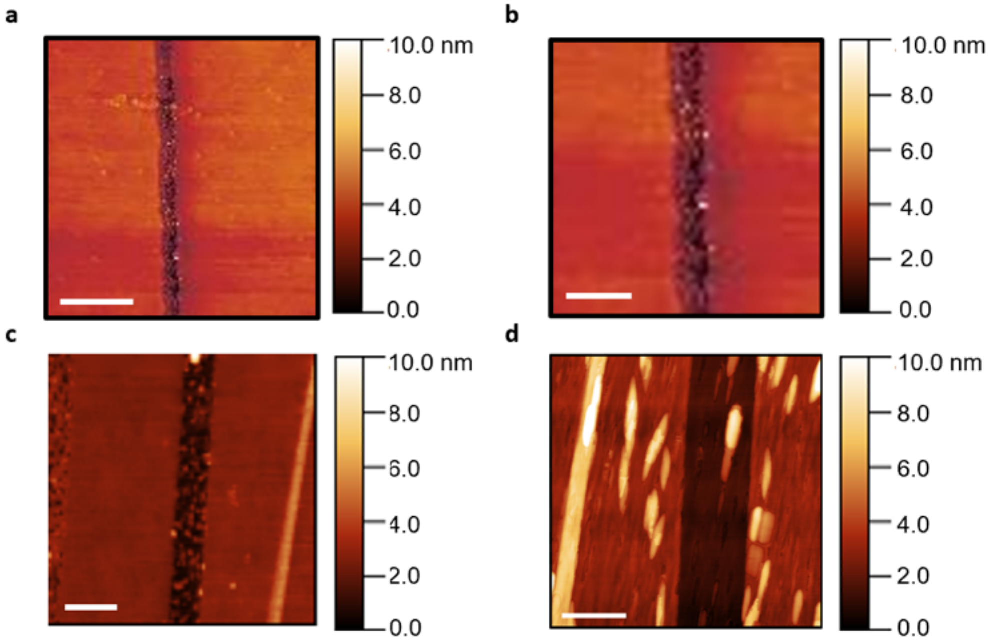

Figure 4.6: Optimizing the graphite etching. a, The graphite was etched with an Ar/O_2 for 1 min. **b,** Zoom-in of **a**. The trench has “wavy” edges, instead of a clean straight edge. **c,** Graphite etched with pure O_2 for 3 sec, leading to a trench with straight edges. **f,** Zoom-in of **d**, clearly showing the straight edges of the etched region, compared with the Ar/O_2 case. The scale bar is 300 and 200 nm for the left and right column, respectively.

The structures are measured in an atomic force microscope (AFM). The results of the etching with Ar/O_2 are shown in Fig. 4.6a-b. A gap of ca. 100 nm is clearly defined. However, there is certain roughness on the edges of the etched region leading to a “wavy” etched region instead of having clean straight edges, which would be ideal for the gating. This can happen because of the long etching times required as the etching rate is ca. 3 nm/min with this recipe [124]. In order to improve the roughness we try a different recipe in which only O_2 is used.

The idea is to make an only chemical etching by using pure O_2. In order to increase the quality of the etched structure the recipe used a high power to achieve etching rates of ca. 1 nm/sec. After the etching the same procedure as before is followed. The results of such a recipe are shown in Fig. 4.6c and d. We observe how in this case the edges of the etched region are better defined, diminishing the roughness observed in the case of the Ar etching. Based on this observation, the etching recipe containing only O_2 is used for the fabrication of the actual samples.

4.4 Final designs

To conclude this section, a summary comparing the initial and final designs is made, as shown in Fig. 4.7. The initial designs enabled to have just one junction per device. The idea was to pre-characterize the MATBG device, find the best region and make the junction there. However, we soon realized that more than one region could be magic-angle, meaning that the junction/device ratio could be improved. Since the main limiting factor of the project is getting a good MATBG device, improving this ratio could largely improve the junction yield.

Some of the other considerations such as the “clamping” direction during stacking or the width ratio between the gates were also not thought of until some devices had been made, since we did not expect the impact they could have on the final devices. The width ratio between the graphite gates for example was not realized until some devices were measured and parts of the phase space remained obscured. This was not only important for this project but it matters for any projects including double gated devices i.e. all the magic-angle family which depends on displacement field like twisted trilayer graphene.

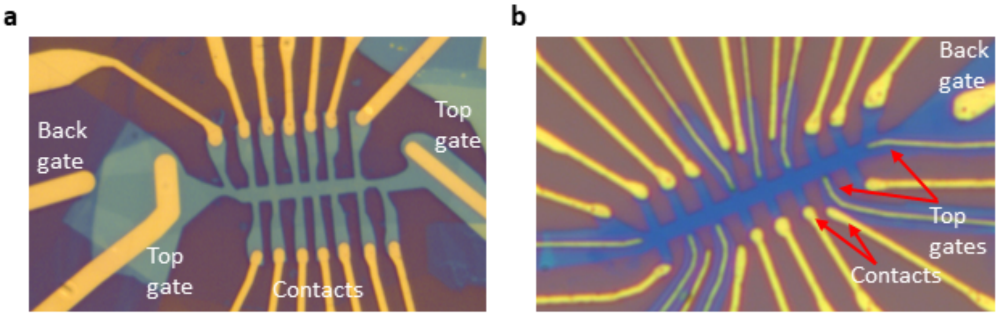

Figure 4.7: Comparison between the initial and the final designs of the MATBG junctions. a, Initial designs. The top gate has only two contacts, allowing to make one junction per device. **b,** The device has 8 contacts to the top gate while keeping all the contacts to MATBG. Junctions can be made between every pair of contacts.

5 Gate-defined Josephson junctions in MATBG

In this chapter we will discuss the basic characterization of the gate-defined Josephson junction in MABTG. First, the general properties of the MATBG device are characterized using only the back gate, while keeping $V_{TG} = 0$ V. Then, both gates will be used independently to map out the presence of the features coming from the junction. Finally, the two gates are used simultaneously to define the gate-defined JJ and characterize it.

5.1 Superconductor characterization ($V_{TG} = 0$ V)

Before measuring the gate-defined JJ, a full characterization of the SC state of the device is done. The performed measurements probe the main properties of the SC: critical current, critical field and coherence length.

5.1.1 R_{xx} vs. V_{BG} vs. T and B

First, we measure the 4-terminal resistance R_{xx} vs. back gate voltage V_{bg} at different temperatures T and magnetic fields B. Fig. 5.1a shows the R_{xx} evolution at different temperatures from $T = 35$ mK up to $T = 10$ K of a $\theta = 1.11°\pm 0.02°$device. The device displays typical features of MATBG devices, having the BIs at high doping and highly resistive states at the integer fillings of the flat band at $\nu = 0, +1, \pm 2$ and $+3$. In the left of the insulating state at $\nu = -2 - \delta$, with $\delta << 1$, the resistance drops to zero at low T, signaling the appearance of a superconducting state. To further confirm the superconducting behavior, R_{xx} is measured vs. magnetic field B in Fig. 5.1b. The figure shows how the zero-resistance state quickly disappears when subjected to magnetic fields of more than 50 mT, and is completely gone at 300 mT. At the right of $\nu = 2$ the R_{xx} vs. V_{BG} vs. B data shows a fast but small R_{xx} increase in the same B-range as the SC state. This is likely to be a developing SC at $\nu = 2 + \delta$.

As can be seen in Fig. 5.1a, the SC in MATBG has the shape of a dome with carrier density. That means that the SC state characterization can be made at different carrier densities n. However when characterizing the state, we are interested to study the SC at the optimal doping. This can in general be taken as the point where the critical temperature T_c is the

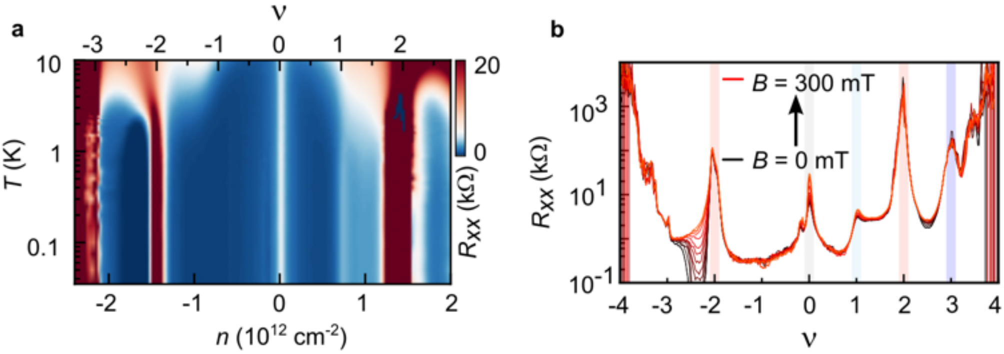

Figure 5.1: Temperature and low magnetic field evolution of the superconducting state. a, 4-terminal resistance R_{xx} vs. back gate voltage V_{BG} vs. temperature T . **b,** R_{xx} vs. V_{BG} vs. B.

highest. The critical temperature is extracted from the R_{xx} vs. T data. As the T is lowered, the resistance experiences a sudden drop to $R = 0\ \Omega$ at low T (see inset of Fig. 5.2a). The critical temperature T_c is extracted as the value of the 50% of the normal state resistance. In this case the optimal SC doping n_S is found to be $n_{SC} \approx 1.72 \times 10^{12}\ \text{cm}^{-2}$, with a $T_c = 3.5$ K.

The rest of the measurements (current-voltage (IV) characteristics, IV vs. T, extraction of coherence length and Fraunhofer pattern) are taken keeping $n = n_{SC}$. Finally, a SC dome characterization is performed.

5.1.2 $I - V$ characteristics

Superconductors are characterized by their non-linear I vs. V behavior. When the current is increased, first the device will not experience any voltage drop, due to the 0-resistance characteristic of the superconducting state. However, when the critical current I_c is reached, an abrupt jump in voltage will appear [58]. The $I - V$ characteristics of device A are shown in Fig. 5.2a. As the temperature is increased, thermal excitations also contribute to break the superconductivity, washing out the sharp $I - V$ transition observed at the lowest T. In the case of a 2-dimensional SC, the transition from the SC to the normal state, takes the form of a Berezinskii–Kosterlitz–Thouless (BKT) transition, defined by a $V \propto I^3$ power law [58]. Such a fit is shown in Fig. 5.2b, extracting a BKT transition temperature of $T_{BKT} = 2.25$ K. In this case, the data is taken as the derivative of the voltage, measuring the differential resistance dV/dI. The dV/dI can help highlight the non-linearities when the $I - V$ transition is not too sharp and as it is measured with a lockin it is cleaner than taking the derivative of the original $I - V$

curve. The data can be improved by measuring this way when measuring up to higher T, higher magnetic fields or at dopings at which the superconducting state is disappearing.

5.1.3 Critical field and coherence length

When subjecting a SC to a magnetic field B, the superconductivity is suppressed due to the depairing of the Cooper pairs. The critical field (B_c) of the device is obtained as the field value described by 50% of the normal state resistance. The coherence length of the SC can then be obtained by extracting the B_c at different T by linearly fitting $B_c = (\Phi_0/2\pi\xi_{GL}^2)(1 - T/T_c)$, where ξ_{GL} is the Ginzburg-Landau superconducting coherence length (see Fig. 5.2c). For this particular device we obtain $\xi_{GL} = 106 \pm 8$ nm at $T = 0$ K, in line with previous reports [40, 44, 48, 43].

5.1.4 Fraunhofer pattern

A final measurement to characterize the SC is the evolution of the $I - V$ characteristic vs. B. As the IV will become less sharp with increasing B field, the dV/dI is measured. A key characteristic of MATBG is its twist-angle inhomogeneity [116], which is intrinsic to the fabrication process. This implies that when the material is set to a certain doping with the V_{BG}, not the whole material will be doped homogeneously. In the case of the SC, this will mean that the material is set to a state with a percolative SC state, surrounded by insulating islands. Such a state, will behave as an array of Josephson junctions, and can lead to the appearance of clear Fraunhofer patterns, as were seen in the first few MATBG devices [39**?** , 43]. However as the devices have become cleaner, it is possible to have a more homogeneous SC state. In this case we don't expect a clear oscillatory pattern, but rather a sharp closing of the SC state with field [90]. Such a measurement is shown in Fig. 5.2d, where a diamond-like feature is observed, showing the cleanliness of the SC state.

5.1.5 Superconducting dome characterization

To fully characterize the SC dome, the dV_{xx}/dI is measured at different dopings of the SC. The dV_{xx}/dI vs. V_{BG} data is plotted in Fig. 5.3. The MATBG SC state has a very distinct shape, in which the right (closer to the CI) and left side of the optimal doping are clearly different. When moving towards the CI, the SC closes in a dome-like manner, while when moving towards largest dopings it develops a tail-like feature in which non-

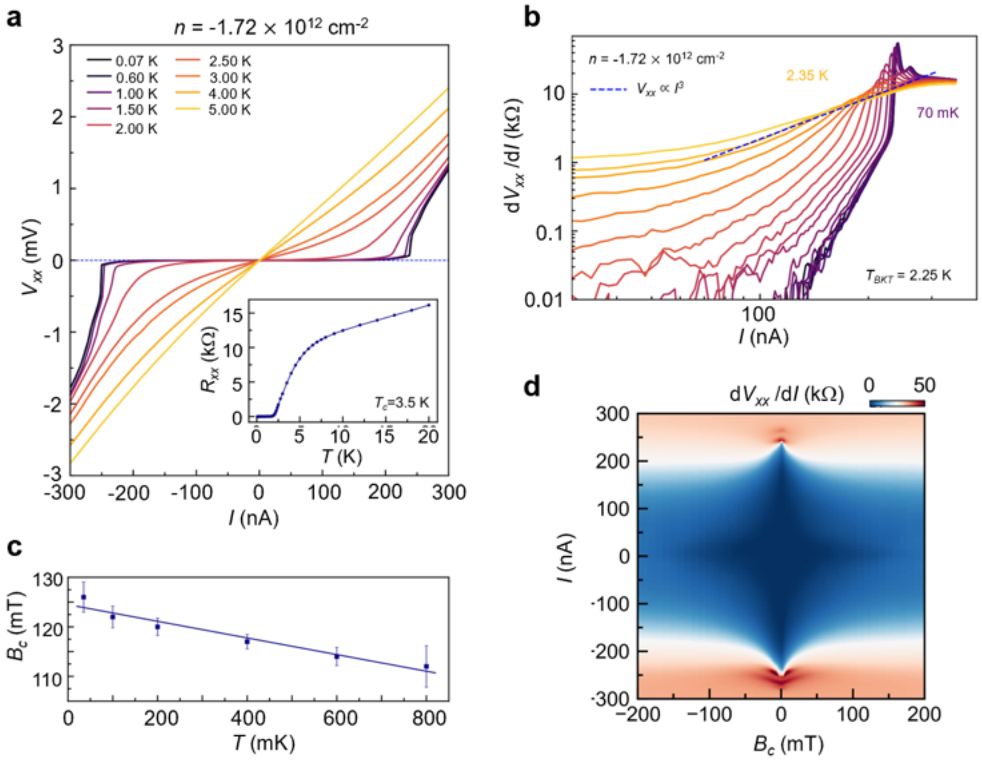

Figure 5.2: SC state characterization, $n = n_{SC} = -1.72 \times 10^{12}$ cm^{-2} **a,** Current-voltage ($I - V$) characteristic for a wide range of temperatures. From the lowest temperature data, we extract a critical current of $I_c = 240$ nA. (Inset) R_{xx} vs. T transition, with a critical temperature $T_c = 3.5$ K. **b,** Differential resistance dV/dI vs. d. c. current I at various T. Fitting $V_{xx} \propto I^3$ yields a BKT transition temperature $T_{BKT} = 2.25$ K. **c,** Perpendicular critical field B_c vs. T taken as half of the normal state resistance values, used to extract the Ginzburg-Landau superconducting coherence length $\xi_{GL} = 106 \pm 8$ nm at $T = 0$. **d,** Fraunhofer pattern (dV_{xx}/dI vs. I vs. B), showing a clean diamond shape decay of the supercurrent.

linearities remain outside of the SC state. Recently such non-linearities have been assigned to be coming from a Zener-Klein tunneling or Schwinger-like mechanism [139, 140], which have been used to link the superconductivity in MATBG with having a quantum geometric origin [139].

5.2 MATBG JJ characterization

After the superconductivity in the device is confirmed and fully characterized, the JJ experiments are performed. Due to the gate tunability of the

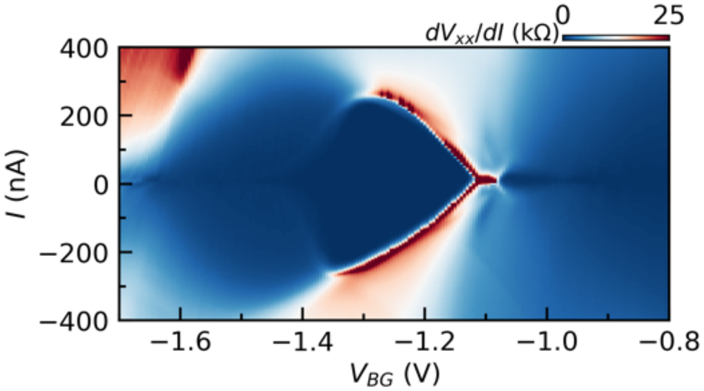

Figure 5.3: Superconducting dome characterization. $\mathrm{d}V_{xx}/\mathrm{d}I$ vs. I and V_{BG}.

material, the first step is to understand how the gating of the junction acts and build a "map" in which we know the states that correspond to every voltage applied on both gates. In the junction devices we define two distinct regions: the region which depend on both gates and the region which depend only (mostly) on the top gate. A schematic of the device and a simulation of the carrier density in these two distinct regions is shown in Fig. 5.4. We refer to the carrier density outside the junction as n to signal the general carrier density, and to the carrier density in the junction as n_J. Once the double gate maps are known we can set $n = n_{SC}$, and tune only n_J to characterize the evolution of the JJ. Finally, we will study the Fraunhofer patterns at different n_J positions to fully confirm the formation of a JJ.

5.2.1 Dual-gate maps

The dual-gate map R_{xx} vs. V_{BG} vs. V_{TG} provides information about the position of the different states in the $gate - space$ and it also provides the capacitance ratios between the gates, which are needed to safely navigate this space. The dual-gate map corresponding to the current device at 1.8 K is shown in Fig. 5.5**a**. The map is composed of two distinct features, which correspond to the n and n_J parts of the device. The diagonal features marked as gray dashed lines, which depend on both gates correspond to the region gated by both the back gate and the top gate, such that $n = C_{BG}V_{BG} + C_{TG}V_{TG}$, where C_{TG} and C_{BG} are the capacitances corresponding to the top gate and back gate respectively. The features corresponding to the junction are displayed as green dashed lines. These features are not perfectly vertical due to stray fields from the top gates [136], such that

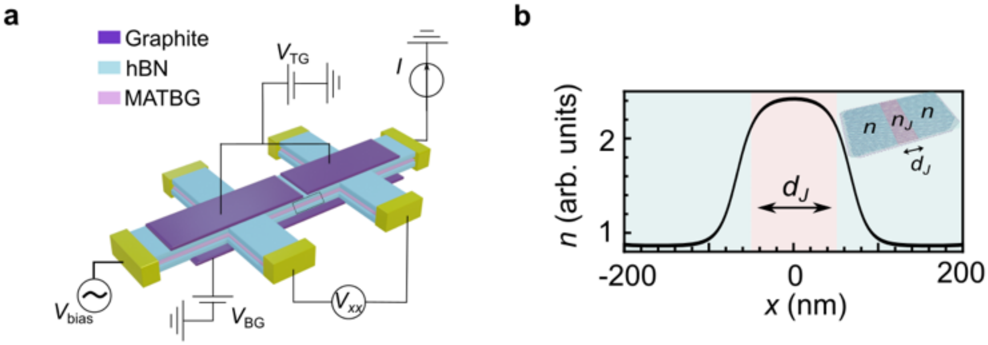

Figure 5.4: Double gate device structure and its corresponding gating profile. a, Schematic of the measured device and measuring circuit, where V_{bias} is the source voltage, I is the current through the device, V_{xx} the voltage drop between the measurement probes and V_{BG} (V_{TG}) correspond to the back (top) gate voltage. The top graphite gates are separated by 150 nm. **b,** Electrostatic simulation profile of carrier density n vs. position x, setting $n \neq n_J$. d_J is the actual length of the junction, defined by the electrostatic profile. The inset shows a schematic of the MATBG JJ with two distinct regions created by the gating structure.

.

$n_J = C_{BG}V_{BG} + \alpha C_{TG}V_{TG}$ where $\alpha << 1$. By following the different lines corresponding to constant n we can change only n_J, effectively creating a junction. Fig. 5.5b, shows a zoom-in of the same data at 35 mK, to highlight the SC region. When the gates are set in a position along a diagonal line following the SC region (keeping $n = n_{SC}$), the JJ is formed.

5.2.1.1 Considerations when performing the double gate maps

The most important thing we want to avoid when performing these experiments is to have sudden leakage currents in the gates, signaling the hBN dielectric breakdown. The most dangerous cases occur when measuring at high opposing voltages on both gates i.e. $V_{BG} >> 0$ and $V_{TG} << 0$. During all these measurements the leakage current on both gates needs to be recorded and special attention is paid to any sudden changes in the slope of the leakage current or a sudden increase on its value. A useful thing to consider during the measurement is that when sweeping one gate, the position of the different features in the other gate will change accordingly. The ratio at which they change will be given by the ratio between the capacitance of the gates C_{TG}/C_{BG}. By knowing this ratio we can limit our experiment to the area of interest. For example, if V_{BG} is the fast changing variable and V_{TG} the slow one, we can set the experiment such that V_{BG} is different

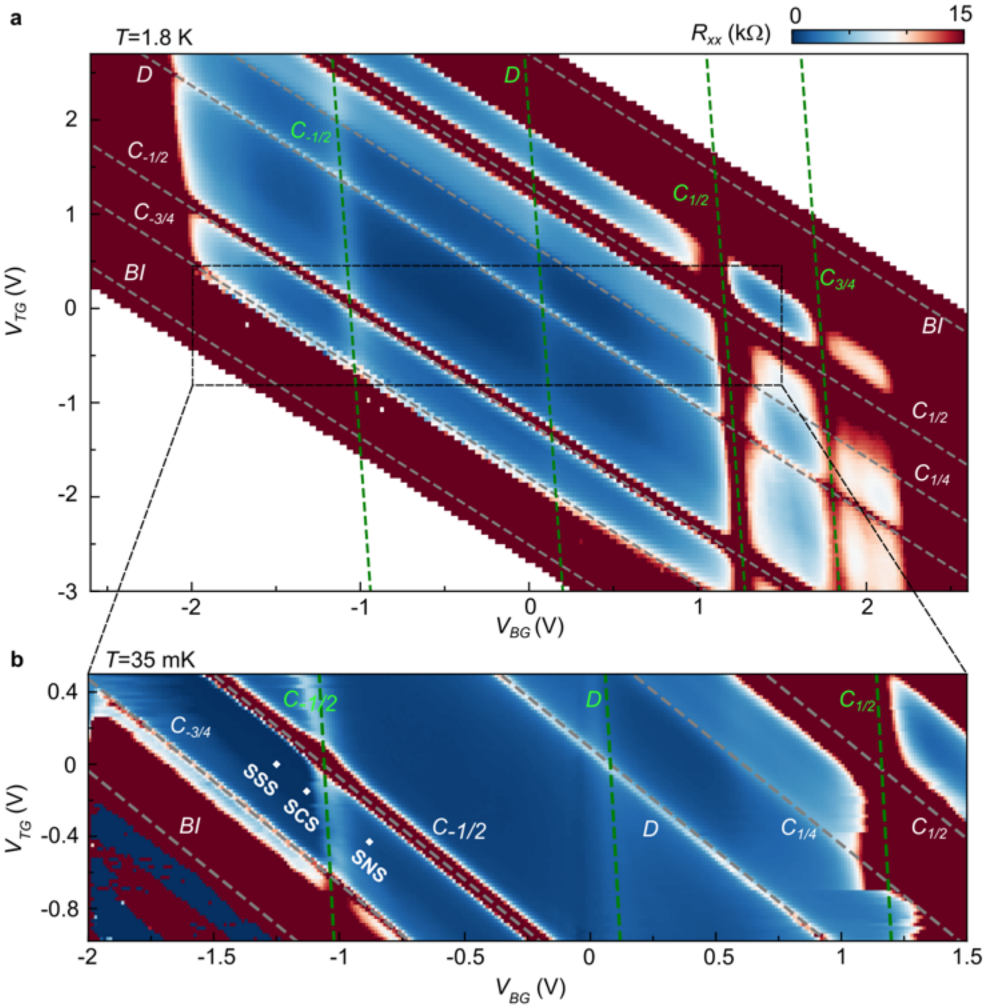

Figure 5.5: Dual-gate maps. a, R_{xx} vs. V_{BG} vs. V_{TG} at $T = 1.8$ K. The diagonal features marked with gray dashed lines are the integer fillings of the main regions (n in Fig. 5.4a), depending on both V_{BG} and V_{TG}. Slightly tilted vertical features, fitted with green dotted lines, are the integer fillings of the junction region (n_J in Fig. 5.4a), mainly gated by the back gate. Labels of the integer filling factors marked by dashed lines correspond to: band insulator (BI) at full filling, correlated insulator at plus/minus three-quarter filling ($C_{\pm 3/4}$), plus/minus half filling ($C_{\pm 1/2}$) and one quarter filling ($C_{1/4}$) and Dirac point (D). **b,** Zoom-in of black-delimited area taken at $T = 35$ mK, where the superconducting state is fully developed. White squares mark the diagonal line in the map at which both main regions are kept in the superconducting state, and the junction region is set at different doping.

for every value in V_{TG}. As we know that at $V_{TG} = 0$, we need to sweep V_{BG} between $-2V < V_{BG} < 2V$, to capture all the MATBG features, we then apply a certain V_{TG} and measure how these features move. By doing this, we can extract the gates ratio C_{TG}/C_{BG}. Next, we need to know the limits required in each gate to capture all the experimental features of of interest. There are two options when performing the measurement: we can sweep V_{BG} constantly between these two extreme values or we can use our ratio to sweep V_{BG} such that it only records the relevant data. In the latter case, our back gate will sweep such that $V_{BG} = V_{BG(V_{TG}=0)} - C_{TG}/C_{BG}V_{TG}$, where $V_{BG(V_{TG}=0)}$ is the value of back gate at zero V_{TG}. The former case can be useful if we are interested in data outside the flat band at intermediate displacement fields, but it will be a much slower measurement and it will force the gate more in every sweep, which could lead to a faster degrading of the dielectric leading up to a leak. The latter case limits the acquired data to inside the flatband, but it is a faster and safer measurement.

5.2.2 JJ-line: dV/dI vs. I vs. n_J

In order to create a JJ, we keep $n = n_{SC} = -1.72 \times 10^{12}$ cm^{-2}, and tune n_J as shown in Fig. 5.6a. When the whole material is in the superconducting state SC/SC/SC, as marked in the figure, we observe a single set of coherence peaks. This corresponds to the optimal doping of the SC in the whole device. However, as we move either to the left or the right of this doping, we observe how a second set of coherence peaks develop. This second set of coherence peaks appear because the doping in the junction is no longer SC, and it is being proximitized by the SC region, effectively creating a JJ. In the figure we see how after crossing the $\nu = -2$ CI, we soon loose the JJ behavior, since the junction is not perfectly proximitized. We still observe non-linearities, corresponding to Andreev reflection but the JJ effect is lost [24]. As we dope even further into the conduction band, and therefore further from the SC doping in the hole band, we eventually see how the junction becomes highly resistive. We believe that the effect of loosing the proximity when doping n_J further from the SC state is in a large part related to the gate-defined nature of the junction. As we dope further, more states will be included in the gated region due to the slow decaying profile, and the junction will be effectively too long to support superconductivity [58].

This is better understood by looking at the electrostatic model. For this device the hBN thicknesses are rather similar, having the simulations with $t_{hBN,top} = 20$ nm and $t_{hBN,bot} = 18$ nm, the etched junction is 150 nm and the values of the potentials in the electrodes are taken from the real values of the device (from Fig. 5.5). Fig. 5.6b show the response of the case where the weak link is set very close to the $\nu = -2$ CI (SC/CI'/SC configuration). The electrostatic potential is converted to n by a factor related to the capacitance of the top and back gates. From the simulations it is possible to estimate the effective size of the JJ (d_J), which does not match the length of the etched region, $d \approx 150$ nm. Since n has a slow transition from the SC to the CI state, the effective length of the JJ is $d_J \approx 100$ nm. This effective length is determined by the n values of the superconducting state. Fig. 5.6c, show the same results for a configuration in which the weak link is set past the CI at $\nu = -1.5$. In this case the effective length of the JJ is ≈ 170 nm, larger than the etched graphite region. This shows how the value of V_{TG} and V_{BG} directly influence the shape of the actual junction. Furthermore due to the complexity of the phase space in MATBG, different phases will appear when gating further from the SC position. For example, in Fig. 5.6c part of the weak link is set at the CI and part at the normal metal N. This adds an extra complexity to the system, since the supercurrent will go through different phases in the material, and some of these phases can become highly resistive. This can explain why proximitizing the weak link across the whole flat band can be complicated in these kind of gate-defined junctions.

Finally, we note how there are some interesting features mostly in the region around $\nu = -2$, where it seems that there are not just two sets of coherence peaks, but that rather several peaks appear. Such behavior can be related to the appearance of multiple Andreev reflections (MAR) in the junctions [141, 142, 143].

5.2.3 Fraunhofer patterns vs. n_J

To further analyze the gate-induced junctions, we set the gates at different values of n_J and apply an out-out-of plane magnetic field B. In the case of a clean MATBG SC we expect a diamond shape decay as shown in Fig. 5.2d. In the case of having a JJ, the field should decay in an exponentially oscillatory manner, as explained in Ch. 2. Such data is shown in Fig. 5.7, where Fraunhofer patterns at different n_J values are shown. We observe how when doping away from the SC/SC/SC position towards the normal metal SC/N/SC or the correlated insulator SC/CI/SC, clear oscillations start to appear. This finally proves the appearance of a gate-defined JJ in the device.

However the three patterns are clearly distinct. In the case of the SC/SC/SC and the SC/N/SC, we observe how the patterns are symmetric w.r.t. the inversion of the current and the field $I_c^+(B^+) = I_c^-(B^+)$ and $I_c^+(B^+) = I_c^+(B^-)$, as is expected for a regular JJ. In stark contrast, the Fraunhofer

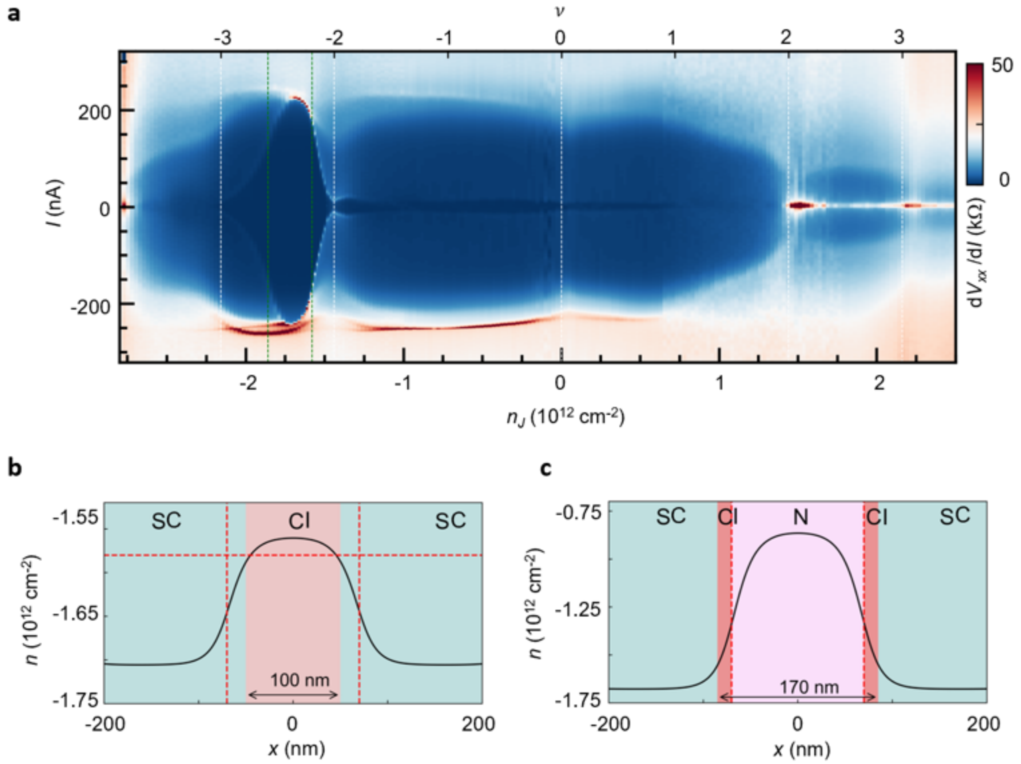

Figure 5.6: JJ-line measurement: dV_{xx}/dI vs. n_J vs. I with $n = n_{SC}$ **a,** Changing n_J while keeping $n = n_{SC}$ changes the junction over all the different features of the MATBG device. As n_J gets very different from n, the proximity effect is lost. White dashed vertical lines show the position of the different CIs and CNP, while green dashed lines mark the limit of the SC state. **b-c,** Electrostatic simulation with the weak link at $\nu \approx -2$ and at $\nu \approx -1.5$, respectively.

pattern at the SC/CI'/SC position shows a very unusual pattern, which is not symmetric with inversion of the current $I_c^+(B^+) \neq I_c^-(B^+)$ and the field directions $I_c^+(B^+) \neq I_c^+(B^-)$. These asymmetries are combined with more unusual properties, such a hysteresis with the inversion of the field and the current directions and a revival of the oscillations at larger B fields. The study of this Fraunhofer pattern at the SC/CI'/SC position will be the topic of the next chapter.

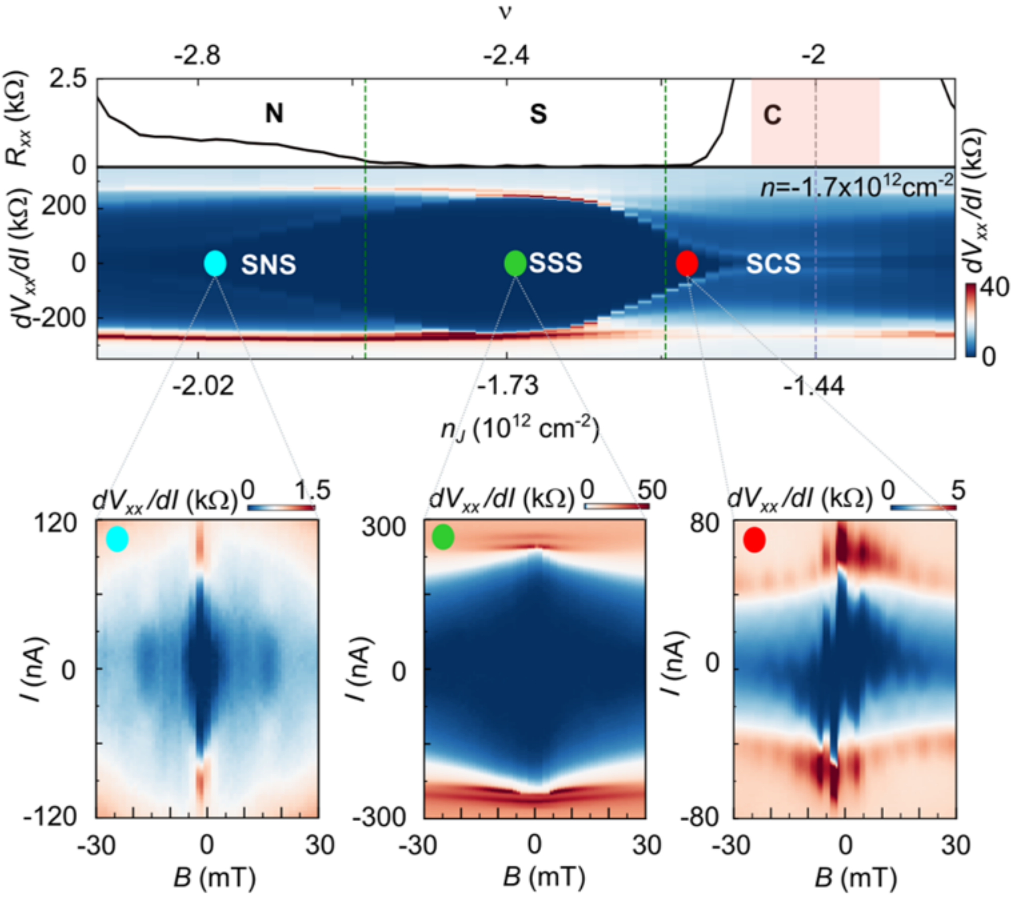

Figure 5.7: Fraunhofer pattern characterization of the JJ. a, (Top) Magnification of R_{xx} vs. ν (Fig. 5.1a) around the superconducting state $-3 < \nu - 1.8$, where we define three distinct regions with metallic (N), superconducting (SC) and correlated insulator (CI) behavior. (Bottom) Zoom-in of Fig. 5.6 around the SC state. $\mathrm{d}V_{xx}/\mathrm{d}I$ vs. I at different n_J, keeping $n = n_{SC} = -1.72 \times 10^{12}$ cm^{-2} in the SC state. Dashed green vertical lines mark the position where n_J is no longer in the SC state. **b**, Fraunhofer patterns measured at (left) $n_J = -2 \times 10^{12}$ cm^{-2} (SC/N/SC), (center) -1.72×10^{12} cm^{-2} (SC/SC/SC) and (right) -1.56×10^{12} cm^{-2} (close to SC/CI/SC), respectively. The color dots show the corresponding n_J positions in the $\mathrm{d}V_{xx}/\mathrm{d}I$ vs. I map in a bottom.

6 Symmetry-broken Josephson junctions and superconducting diodes in MATBG

This chapter is dedicated to understanding the unconventional Fraunhofer pattern of the SC/CI'/SC JJ configuration which was shown in Fig. 5.7. This unconventional Fraunhofer pattern shows asymmetry both in the direction of the current and field directions, which indicate a breaking of inversion and time reversal symmetry [144]. To further understand the origin of these signals we first make a phenomenological model based on the current density distribution of the junction. Secondly, we study the magnetism by measuring the T evolution of the pattern and making a tight binding model to see which possible state of MATBG could explain the observed signals. Finally, we prove how the broken inversion and time reversal symmetry allows us to have a reversible zero-field superconducting diode.

In order to better observe the current and field direction asymmetries, we extract the critical current I_c vs. B and plot the linecut of $\mathrm{d}V_{xx}/\mathrm{d}I$ vs. I at $B = 0$ mT of the pattern (Fig. 6.1b and c). Most strikingly, for both measurements we observe a hysteresis with the B-field direction. For the I_c measurement we measure the Fraunhofer pattern in opposing B-field directions and extract the corresponding I_c values, defined by the contour of zero-resistance state in the data. For the $\mathrm{d}V_{xx}/\mathrm{d}I$ plot, we extract the zero-field value $\mathrm{d}V_{xx}/\mathrm{d}I$ trace after having applied two different pre-magnetizing fields B_M. We observe a clear hysteresis showing a reversible non-reciprocal transport behavior, with the SC being increased for a certain current direction depending on the previously applied B_M.

6.1 Asymmetries and edge states

The Fraunhofer pattern at this n_J measured up to higher magnetic fields (Fig. 6.1a) shows a revival of the oscillations and the SC state after a field of ±30 mT, where the oscillations have completely decay and then reappear again. The double periodicity suggests the presence of edge states giving rise to a SQUID-like type of behavior [145]. In order to better understand the origin of the signals (the revival of the oscillations and the asymmetry of the data), we make a phenomenological model in which we calculate a Fraunhofer pattern corresponding to a given current density distribution in real space.

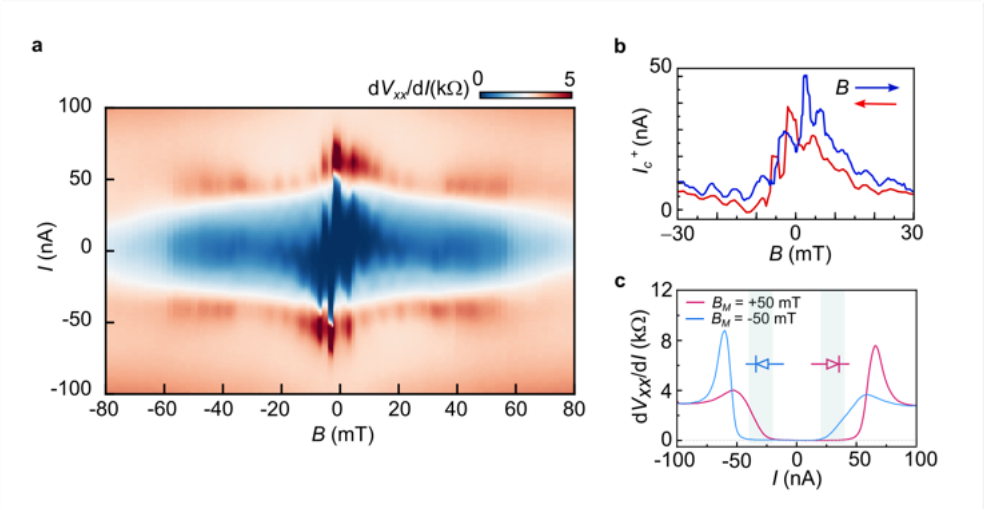

Figure 6.1: Fraunhofer pattern at SC/CI'/SC with n_J close to $\nu = -2$. a, Same Fraunhofer pattern as in Fig. 5.7b extended to higher magnetic fields. **b,** Positive critical current I_c^+ vs. B with B sweeping up (blue) and down (red). **c,** dV_{xx}/dI vs. I at $B = 0$ mT after applying a pre-magnetizing field $B_M = +50$ and -50 mT for the red and blue curve.

6.1.1 Modeling Fraunhofer patterns from current density distribution

The critical current I_c of a JJ in a perpendicular magnetic field is represented by the modulus of the Fourier transform of the current density distribution in real space $J_s(x)$ [146]. Therefore one can extract $J_s(x)$ of a JJ by calculating the inverse Fourier transform of the measured Fraunhofer pattern. The process to calculate the Fraunhofer pattern from $J_s(x)$ is done following the procedure developed by Dynes and Fulton [146]. Given a certain $J_s(x)$, its complex Fourier transform will yield a complex critical current function:

$$\mathrm{Im}_c(\beta) = \int_{-\infty}^{\infty} J_s(x) e^{i\beta x}\, dx \tag{6.1}$$

where $\beta = (d_J + 2\lambda)B/\Phi_0$ is a normalized field in units of µm, d_J is the length of the JJ and λ is the penetration depth into the superconducting electrodes. The extra λ component is used to take into account the fact that the real length will be extended due to the field penetration into the SC electrodes. The experimentally measured I_c is then given by the modulus of this complex current density distribution:

$$I_c(\beta) = |\mathrm{Im}_c(\beta)|. \tag{6.2}$$

In our case, an additional adjustment is made, since we are dealing with JJs in a two-dimensional material. As explained in Ch. 2, the Fraunhofer pattern will then be dominated by the relation $\Delta B_{2D} \approx 1.8\Phi_0/w^2$, instead of the more conventional $\Delta B_{3D} \approx \Phi_0/wL$, where L is the length of the junction (considered $d_J + 2\lambda$ here). Therefore we modify the parameter L inside the β parameter for the approximation $w/1.8$ to account for the fact that the material will not screen the magnetic field.

A homogeneous $J_s(x)$ will give the regularly studied Fraunhofer pattern, while more complex current density profiles lead to more complex diagrams. Here, we focus on the presence of possible edge states which contribute to the supercurrent. The calculated Fraunhofer patterns with different combination of bulk and edge conduction channels are shown in Fig. 6.2. We observe how by having a combination of edge and bulk contribution we can model the revival of the oscillations observed in experiments (Fig. 6.2c,f). Compared with the only-edge-states case, another difference is the decaying of the central lobe. When only having edge states, the central lobe has a very slow decay while in the case combining edge and bulk supercurrent, the fast decay corresponding to the bulk Fraunhofer pattern is conserved.

After having seen that the revival can be modeled by a combination of edge and bulk supercurrent (Fig. 6.2), we want to focus and try to simulate the observed asymmetries, mainly the fact that $I_c^+(B^+) \neq I_c^-(B^+)$ and $I_c^+(B^+) \neq I_c^+(B^-)$. In order to simulate these asymmetries we introduce some phase shifts into the patterns to simulate the magnetic origin of the signals. The phase shifts are introduced as an extra field in the β parameter by substituting $B = B_{ext} + \varphi$, where B_{ext} is the external field and φ will be the extra phase. This phase could have different origins [147], but in this model we just study it as a component which changes the effective field experienced by the sample. The next step is to separate these phases for the different components of the pattern by introducing φ_{edge1}, φ_{edge2} and φ_{bulk}, corresponding to the different edges and the bulk of the JJ (these parts are highlighted in the cartoon in Fig. 6.3a). When $\varphi_{edge_1} = \varphi_{edge_2}$, we refer to it simply as φ_{edges}.

The obtained Fraunhofer patterns corresponding to different combinations of these phases are shown in Fig. 6.3. In general we keep $\varphi_{bulk} = 0$, because we are interested in the asymmetries of the data. The bulk phase would

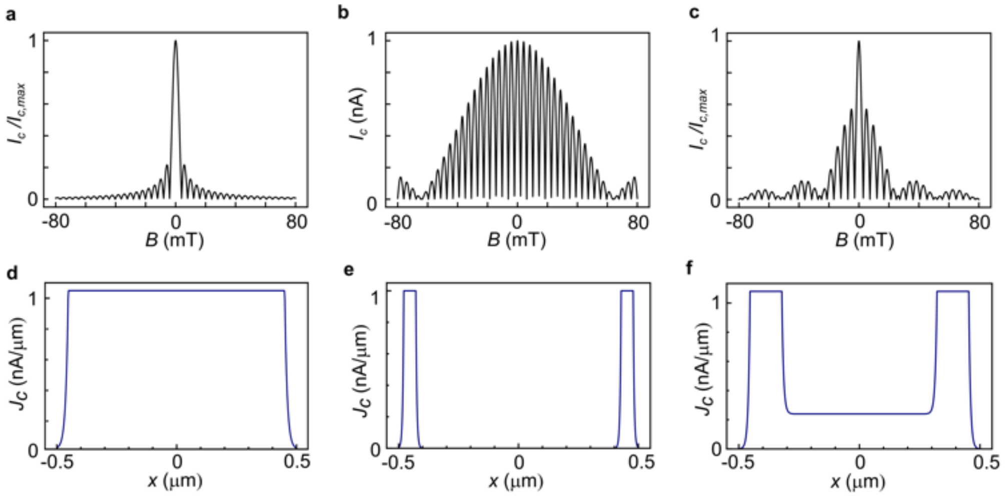

Figure 6.2: Fraunhofer patterns corresponding to different $J_s(x)$. a-c, Normalized critical current $I_c/I_{c,max}$ vs. perpendicular magnetic field B corresponding to the current density J_c distributions shown in **d-f,** where x is the direction in the length of the JJ.

contribute to a total shift of the pattern, but it does not produce any asymmetries. We find that the asymmetries in $I_c(B)$ arise when $\varphi_{bulk} \neq \varphi_{edges}$, yielding a signal in which $I_c^{\pm}(B^+) \neq I_c^{\pm}(B^-)$, as we observe in the experiment. In order to obtain the current-field coupling leading to the tilt of the signal, the phase of the edges needs to change sign with the current direction: $sgn(\varphi_{edges}(I^+)) = -sgn(\varphi_{edges}(I^-))$. By introducing this current induced phase, we obtain all the broken symmetries observed in the pattern at the SC/CI'/SC position, that is: $I_c^+(B^+) \neq I_c^-(B^+)$ and $I_c^+(B^+) \neq I_c^+(B^-)$, while keeping the symmetry along the $I-B$ coupled direction: $I_c^{\pm}(B^+) = I_c^{\mp}(B^-)$. These correspond to having a broken inversion symmetry [144]. In the experiment $I_c^{\pm}(B^+) \neq I_c^{\mp}(B^-)$ due to the magnetic hysteresis, which breaks time reversal symmetry $\mathcal{T}$. The breaking of $\mathcal{T}$ could be introduced in our model as well just by adding an extra phase to the whole device, which would shift the pattern to the positive or negative direction. Finally, the pattern that resembled most the data (Fig. 6.3d) is obtained by also making $\varphi_{edge_1} \neq \varphi_{edge_2}$, such that both edges carry a different phase.

From this model we can conclude that the measured Fraunhofer pattern requires the presence of edge states which carry an additional phase with respect to the bulk $\varphi_{edges} \neq \varphi_{bulk}$, this phase changes sign for a given current direction $\varphi_{edge_i}(I^+) = -\varphi_{edge_i}(I^-)$ and, in addition, there is a general

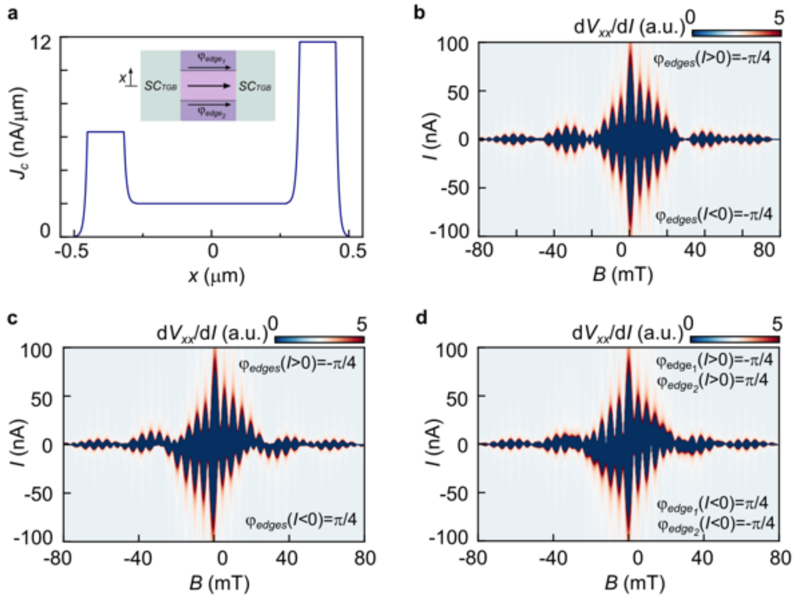

Figure 6.3: Asymmetric Fraunhofer patterns corresponding to different symmetry broken current densities. a, Current density profile to calculate the Fraunhofer patterns including both bulk and edge contribution. The inset shows a cartoon displaying the superconducting TBG forming the JJ (SC_{TBG}) in light green and the weak link with bulk and edge contribution in purple and violet, as well as the different phases carried by the edges $\phi_{edge,n}$, where $n = 1, 2$ for the top and bottom edge respectively **b,** Modeled Fraunhofer pattern based on the current density profile of **a** having a different phase between edge and bulk but with the same phase between edges. **c,** Same as **b**, but the phase of the edges changes when inverting the current direction. **d,** The phases of the two edges are opposite and they change sign upon changing the current direction.

magnetism in the junction which is responsible for the global phase shift and the hysteresis at low T. Fig. 6.4a-c plots the original data next to the Fraunhofer from Fig. 6.3d, which better reproduces the data

A second sample with twist angle 1.04 ± 0.02° has also been measured (device B). The $I_c(B)$ behavior of the new sample at the SC/CI'/SC position is shown in Fig. 6.4d. In this case we do not observe any asymmetries or hysteretic behavior, but the sample displays clear SQUID-like oscillations. We can again model the pattern, in this case having a supercurrent which is purely carried by the edge states (Fig. 6.4e), hinting that in device B the CI state has a more insulating bulk than for device A. For both devices we observe how in the SC/CI'/SC configuration edge states play an important

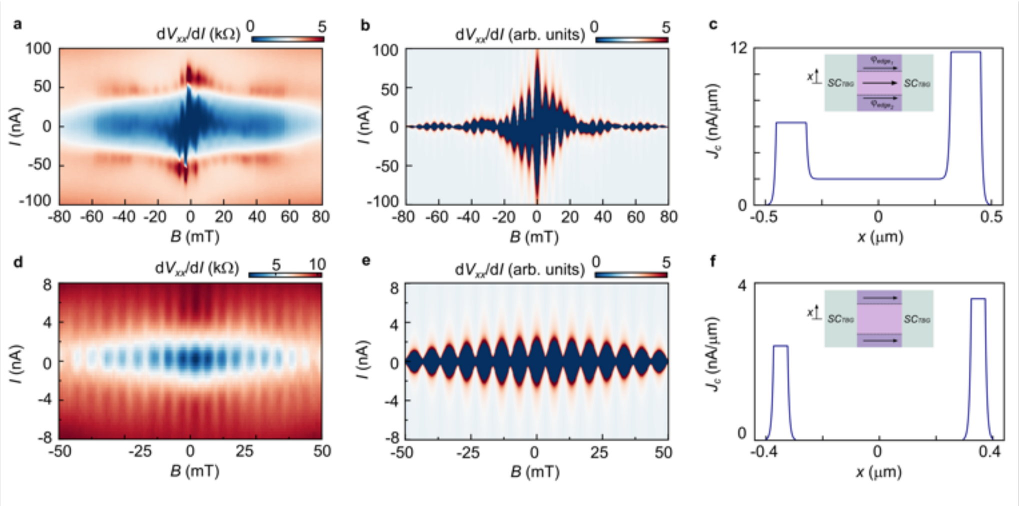

Figure 6.4: Fraunhofer patterns emerging from edge state supercurrent of device A and B. a, Fraunhofer pattern at the SC/CI'/SC position of sample A. **b,** Calculated $I_c(B)$ behavior based on the current density distribution shown in **c**. A combination of edge and bulk supercurrent with non-symmetric edges give rise to a qualitatively similar pattern as measured in experiment. **c,** Current density distribution combining edge and bulk supercurrent. **d,** Fraunhofer pattern at the SC/CI'/SC position of sample B. The pattern resembles a pattern coming from purely edge supercurrent. **e,** Calculated $I_c(B)$ behavior based on the current density distribution shown in **f,** in which all the supercurrent is carried by the edges. **f,** Current density distribution with only edge conduction. The inset shows a cartoon in which the current is only carried by edge states, without acquiring any extra phase.

role carrying the supercurrent.

6.2 Magnetic Josephson junction

Next, we analyze the magnetic signatures observed in device A. First, we analyze the Fraunhofer pattern at an elevated temperature of $T = 800$ mK, where the hysteretic behavior at low field (shown in Fig. 6.1b) has not yet developed and describe a tight-binding model in which we can simulate the observed signatures by having a valley polarized state with Chern number $C = -2$ as the weak link of the junction. Then, we study the temperature evolution of the Fraunhofer pattern as the sample is cooled down to the base temperature of $T = 35$ mK. Finally, we close this section by discussing the possible origins of the different signals.

6.2.1 800 mK results

The Fraunhofer pattern at 800 mK is shown in Fig. 6.5b. The pattern at this T has the following unconventional features: 1. The central peak of the pattern is shifted from $B = 0$ to a value of ≈ 2.5 mT; 2. The Fraunhofer pattern is highly asymmetric with respect to the central peak; 3. The critical current I_c does not vanish as a function of field at each Φ/Φ_0 as in regular Fraunhofer patterns; 4. Upon inversion of the current direction a different pattern is observed and the central peak is shifted as shown in Fig. 6.5d. At $B = 0$ for example the critical current is dramatically different for current flowing in opposite directions $I_c^+(B = 0) \neq I_c^-(B = 0)$; 5. The critical current shows a hysteresis and the directional dependence of the critical current appears only when the system is pre-magnetized by an external magnetic field larger than a coercive field of ≈ 300 mT (purple and orange line in Fig. 6.5a). The fact that none of these features are observed in the SC/SC/SC and the SC/N/SC junctions, we suggest that the CI state in the middle of the JJ is an unconventional insulating state responsible for the observed Fraunhofer pattern.

Qualitatively, the shift of the central peak, the breaking of the time-reversal symmetry condition $I_c^+(B^+) = I_c^+(B^-)$ and the hysteresis behavior all suggest that time-reversal symmetry is broken and there is a spontaneous net magnetic flux which is responsible to move the position of the central peak away from the $B = 0$ position. Furthermore, the observed behavior in Fig. 6.4 indicates that edge states play an important role in carrying the supercurrent. It is important to note that the observed unconventional Fraunhofer patterns are highly reproducible, i.e. we do not observe significant changes in the patterns after several thermodynamic cycles of warming up and cooling down the sample. We also note that this phenomenon is observed for a limited range of doping when the weak link is set at $\nu = -2 - \delta$, very close to the CI at $\nu = -2$ but not exactly at the insulating state.

The question to ask is: which microscopic state of MATBG near of $\nu = -2$ can explain the observed features? We propose below that the observed experimental features are consistent with the assumption that the CI is an interaction induced valley polarized state with net orbital magnetization.

6.2.2 Valley polarization in the JJ

The energy bands of MATBG consist of 4 flavors due to the spin and valley symmetries, whose degeneracy is protected by the $C_2\mathcal{T}$ symmetry of the system. It has been shown however that this symmetry can be broken by

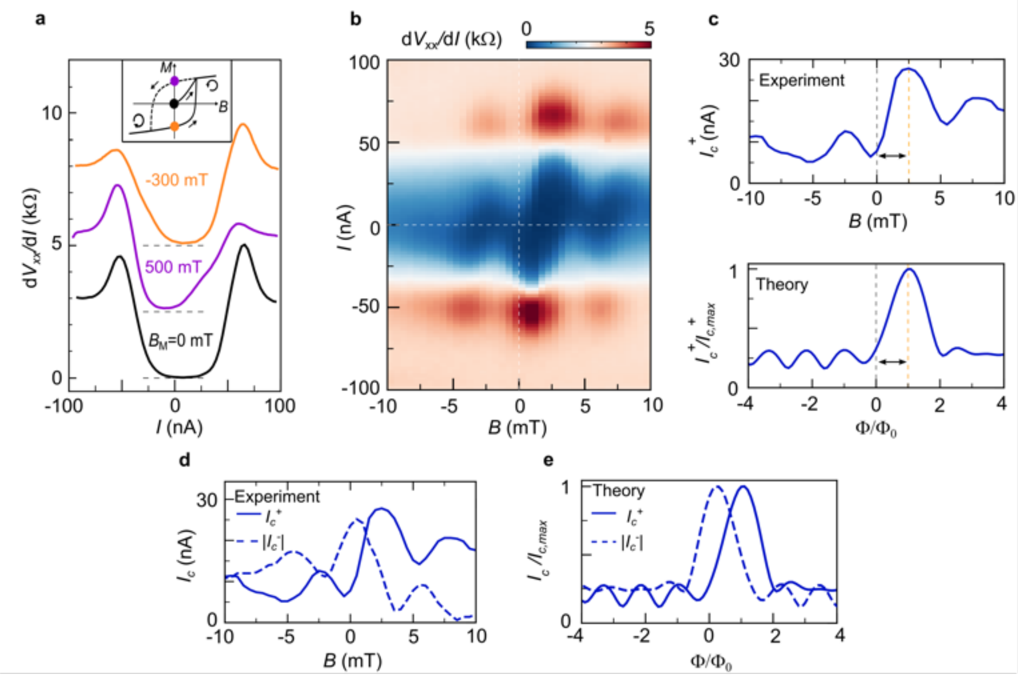

Figure 6.5: JJ with orbital magnetism. **a,** $\mathrm{d}V_{xx}/\mathrm{d}I$ vs. I measured at $B = 0$ mT and $T = 800$ mK right after cooldown (black) and after the sample has been subjected to two opposing pre-magnetizing fields B_M. The curves are vertically shifted by 2.5 kΩ each for clarity. The inset shows a schematic of magnetization M vs. B. The colored dots correspond to the magnetic states in which the different $\mathrm{d}V_{xx}/\mathrm{d}I$ vs. I curves were taken and the arrows describe the direction in which the field is swept. **b,** Fraunhofer pattern with $n_J = -1.56 \times 10^{12}$ cm^{-2} measured at 800 mK. The white dashed lines mark the 0 current and 0 field positions. **c,** (Top) Positive critical current I_c^+ vs. B at 800 mK. The vertical dashed lines remark the shift of the I_c^+ maximum from zero field. (Bottom) Theoretical I_c^+ vs. magnetic flux (Φ) normalized by the flux quantum (Φ_0) calculated for a MATBG JJ with a valley-polarized $\nu = -2$ state as the weak link. The pattern has been shifted by $+\Phi_0$ to compare with the experiment. **d,** Experimental I_c^+ and $|I_c^-|$ vs. B, extracted from **b**. Reversing the current direction inverts the line-shape of the curve and changes the shift in magnetic field. **e,** Theoretical I_c^+ and $|I_c^-|$ vs. Φ for a MATBG JJ with a valley polarized $\nu = -2$ state as the weak link. To compare with the experiment, a shift of $+\Phi_0$ and $+0.2\Phi_0$ were added to I_c^+ and $|I_c^-|$, respectively.

breaking either C_2 or $\mathcal{T}$ symmetry, for example aligning to hBN breaks the former and applying a magnetic field breaks the latter [148, 53]. It has been argued how the strong interactions can be enough to break the symmetry, leading to the appearance of different topological bands with certain Chern number [41]. A possible state that might arise in the case of the $\nu = -2$ CI is a valley polarized state with Chern number $C = -2$.

Several experimental signatures support this hypothesis. Such a state has been previously identified at slightly elevated magnetic fields $B > 300$ mT [90], which is in good agreement with the observed coercive field of the JJ. Moreover, the orbital magnetic moment of this state is very large ≈ 6 μB (Bohr magneton) [88] and results in an out-of-plane magnetic field of $B \approx 3$ mT. This is consistent with the experimentally obtained phase shift of $\Delta B \approx 2.5$ mT. The phase shift of the Fraunhofer pattern survives up to the critical temperature of the JJ of $Tc \approx 1$ K, and is comparable to the Curie temperature of previously observed orbital magnetic states in hBN aligned [51, 50] and non-aligned MATBG [44, 48] as well as in twisted mono-bi graphene [149, 150]. Finally, the valley polarized state with orbital magnetization is characterized by the presence of edge states, which would arise as observed in the Fraunhofer patterns of Fig. 6.4.

To further support this hypothesis, we construct a MATBG based JJ model by assuming the CI in the central region to be a valley polarized state with net Chern number $C = -2$ at filling factor $\nu = -2$, while the Chern bands are partially filled (see the SI of [71] for details and the main text of [147] for a follow-up theoretical work). The superconducting part of the JJ is assumed to be a fully gapped superconductor with s-wave pairing. The theory clearly reproduces the asymmetry with respect to the central peak of the unconventional Fraunhofer pattern (Fig. 6.5c). Unlike in the case of a conventional Fraunhofer pattern, it is asymmetric with respect to the B-field direction, where $I_c(B^+) > I_c(B^-)$. We found that removing the $C_2\mathcal{T}$ breaking terms will make the bands topologically trivial with no Berry curvatures nor net orbital magnetic moments. In this case, a standard Fraunhofer pattern is obtained (Fig. 6.6). This suggests that this behavior is a direct consequence of the electronic ground state near $\nu = -2$ carrying orbital magnetization. We can also simulate the behavior of device B by setting the chemical potential into the gap of the CI, equivalent to having a more insulating bulk, in which case the current is solely carried by edge states, consistent with the results shown in Fig. 6.4. Therefore, the main features of both devices can be captured within the same model.

To explain the directional dependence of the critical current in Fig. 6.5d,

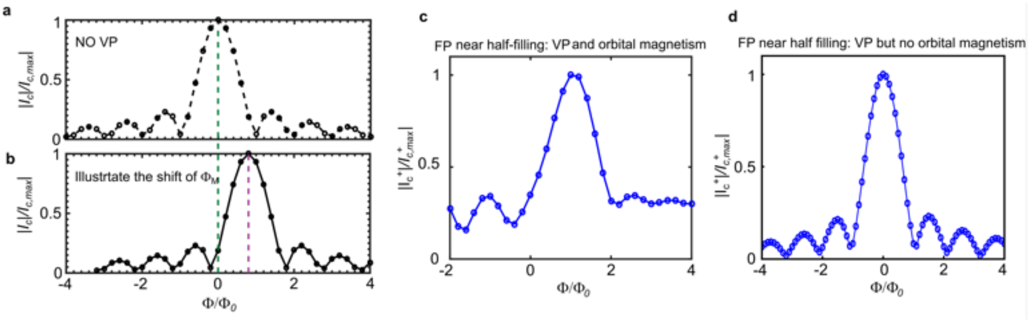

Figure 6.6: Fraunhofer pattern in the presence of valley polarization and orbital magnetism. a, Standard Fraunhofer pattern when the weak link is a metal. **b,** Same Fraunhofer pattern having a shift of Φ_M in the Fraunhofer pattern due to the orbital magnetism. **c,** Typical Fraunhofer pattern near half-filling, which supports an insulating gap. The asymmetry is induced by the valley polarization. **d,** Fraunhofer pattern near half-filling with no $C_2\mathcal{T}$ symmetry breaking terms. The asymmetry is not present in this case as there is no orbital magnetization.

one extra assumption is needed. Namely, that the current $I \approx 10$ nA can induce orbital magnetization switching similar to the current induced orbital magnetization switching, which is observed at a filling of $\nu = 3$ in MATBG [51, 50, 149, 151, 152, 153]. In other words, a small current can overcome the free energy barrier between two degenerate orbital magnetization states of the CI. With this assumption, which is further motivated by the phenomenological model of Fig. 6.4, the directional dependence of the critical current is well explained (Fig. 6.5e). In the case of device B, the fact that there is no bulk current and the I_c is an order of magnitude smaller (~ 5 nA vs. 80 nA), could be the reason why no asymmetry is observed. However, further theoretical study is needed to understand the current induced orbital magnetization switching in this $C = -2$ state.

6.2.3 Low Temperature Magnetism

The Fraunhofer pattern of device A at low temperatures is even more intriguing. Figure 6.7a and b show it for $T = 500$ mK, where it is measured by sweeping the B-field up (a) and down (b). Strikingly, both Fraunhofer patterns show a phase jump (marked by an arrow), which was not observed at higher temperatures. Comparing the two Fraunhofer patterns, one notices that they are phase shifted, and overall symmetric with respect to the reversal of the current and B-field directions, $I_c^+(B^{+,\rightarrow}) \approx I_c^-(B^{-,\leftarrow})$. Its phase jump is hysteretic and occurs at different B-fields for the up ($B^{\rightarrow}$) and

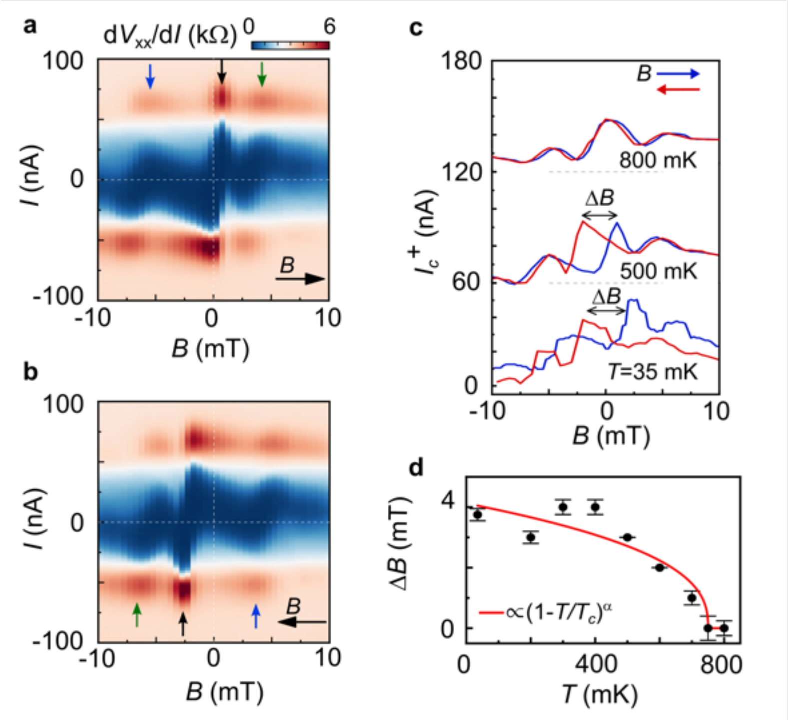

Figure 6.7: Evolution of magnetic hysteresis with temperature. a-b, Fraunhofer patterns measured at 500 mK with field sweeping up (**a**) and down (**b**) as marked with the black arrows. The white dashed lines mark the 0 current and 0 field positions. The colored arrows highlight a period change in the pattern and the fact that by rotating **a** by 180° one would get the periodicity of **b**. **c,** I_c^+ extracted from the Fraunhofer patterns with the magnetic field sweeping up (blue) and down (red) at 800, 500 and 35 mK. The curves are vertically shifted by 60 nA each for clarity. **d,** Extracted ΔB vs. T for I_c^+. The red curve is a fit to the Curie-Bloch equation $(1 - T/T_c)^\alpha$ with fitting parameters $T_c \approx 750 \pm 25$ mK and $\alpha \approx 0.4 \pm 0.05$. The error bars are defined as the standard deviation of the extracted I_c values.

down ($B^{\leftarrow}$) sweeps. Such B-field hysteresis is better seen in the line-cuts in Fig. 6.7c, which shows the $I_c^+(B)$ for both field sweeping directions at $T = 800$, 500 and 35 mK. Here we define ΔB as the difference between the maxima of the $I_c^+(B^+)$ and $I_c^+(B^-)$ sweeps. If we understand this hysteresis as the magnetization of the sample and plot its temperature dependence, we can fit it with a Curie-Bloch equation [154] $\Delta B \approx (1 - T/T_c)^\alpha$ (Fig. 6.7d) obtaining a Curie temperature $T_c \approx 750 \pm 25$ mK and $\alpha \approx 0.4 \pm 0.05$. The different Fraunhofer patterns taken at increasing T from 35 to 800 mK from which the data is obtained are plotted in Fig. 6.8.

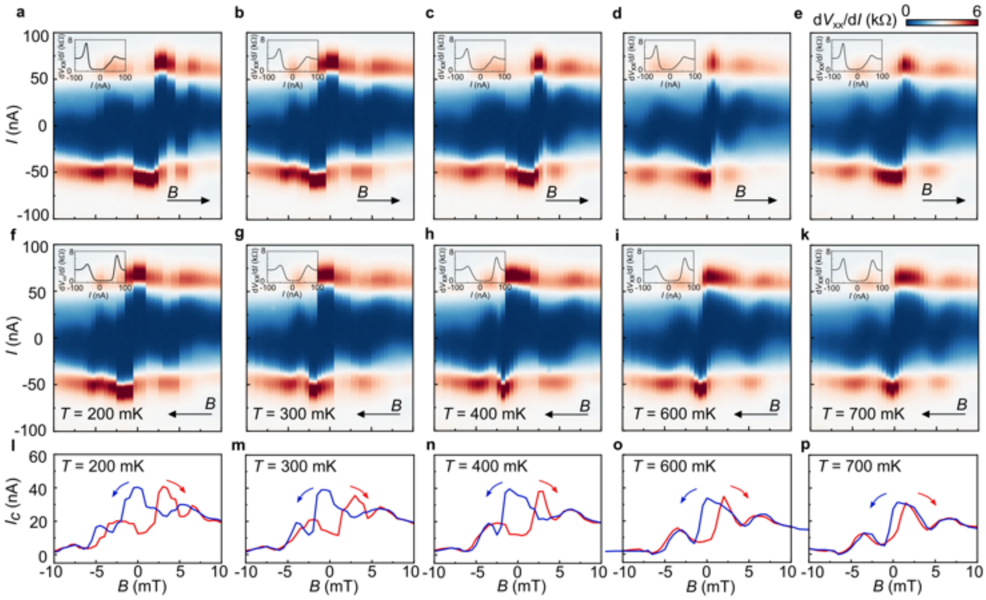

Figure 6.8: Temperature dependence of the SC/CI'/SC Fraunhofer pattern and its hysteresis. **a-e**, Fraunhofer patterns measured at $n_J = -1.56 \times 10^{12}$ cm^{-2}, at increasing T from 200 mK to 700 mK and by sweeping the magnetic field up, as marked with the black arrow. Insets of each plot show a dV_{xx}/dI vs.I linecut at $B = 0$ T. **f-k,** Corresponding Fraunhofer patterns to **a-e** respectively, at the same temperature but opposite magnetic field sweep direction. **l-p,** Extracted I_c^+ from the corresponding temperatures and with field sweeping up (blue) or down (red).

6.3 Discussion

Both the hysteresis of $I_c(B)$ and the phase jumps are prominent characteristics of ferromagnetic JJs [155, 156, 157]. The hysteresis is induced by the switching of the magnetic moments and the phase jumps are due to the presence of domains switching at different field values. In Fig. 6.8 it is clear that when lowering the T more phase jumps appear, which is consistent with the development of more magnetic domains in the sample. While the $I - B$ asymmetry, indicative of orbital magnetism, continues to be present in the Fraunhofer pattern at lower temperatures, the low T hysteretic features cannot be fully explained by it. These appear at a lower temperature and require switching field $|B_M| \geq 3$ mT that is two order of magnitude lower than observed for the valley polarized state (see Fig. 6.9). Therefore, a further theoretical explanation is needed to explain these lower T features which have a clear distinct behavior.

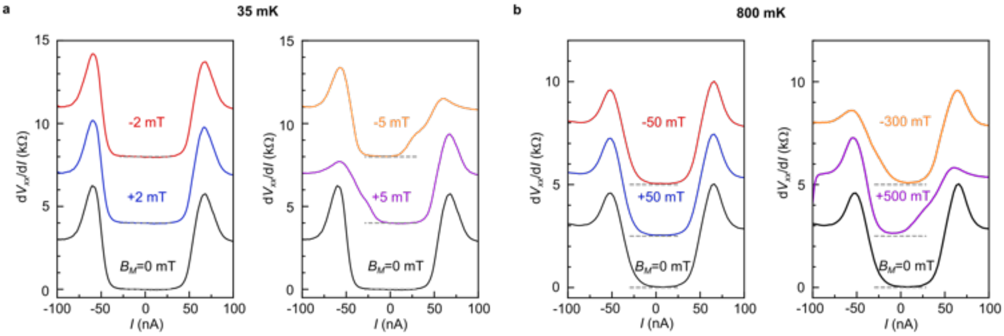

Figure 6.9: Distinguishing between high and low field hysteresis. $\mathrm{d}V_{xx}/\mathrm{d}I$ measured right after cooling down (black curves) or after applying different pre-magnetizing fields B_M at $T = 35$ mK **a,** and $T = 800$ mK **b,** While at 35 mK, fields above 3 mT are enough to switch the magnetic state, at 800 mK, fields above 300 mT are needed, proving the presence of two distinct effects.

Without further theoretical insights, we can just propose possible scenarios based on the data. A first scenario would be to have both spin and valley polarization, for example, by having a partially valley-polarized state, in which both the spin and valley flavors have a population imbalance. Such states have been studied recently as possibilities to explain magnetic signals observed at $\nu = -2$ [158] and had been previously discussed in literature [89]. In this scenario the valley and spin polarization could have different energy scales, being responsible for the observed signals. Another alternative would be to have domains of different magnetic behavior as has been recently observed in a SQUID on tip experiment by Grover *et al.* [159]. In the domain picture, there could be domains all of orbital origin or a combination of domains of orbital and spin origin. In the latter case the spin and orbital domains could behave differently while, in the former case, the different behavior could be coming from domains of different sizes or domains having a different type of magnetic behavior as was observed in [159]. Considering the phase jumps in the data at low T and the modeling of the current density with opposing phases on both edges, the domain picture might be a more likely scenario. However, a definite proof of the origin of these signals cannot be drawn from the present study.

6.4 Superconducting diode effect

A direct consequence of the remnant magnetization and its current induced magnetization switching in the MATBG JJ, is its non-reciprocal transport. This is demonstrated in the $\mathrm{d}V_{xx}/\mathrm{d}I$ vs. I curves taken at $B = 0$, which show highly non-symmetric behavior with respect to the current direction. As can be clearly seen in Fig. 6.10a, for a fixed current value $|I| \approx 10-50$ nA the device can be superconducting in one current direction, while highly resistive in the other. This behavior enables the creation of a superconducting diode, which is the superconducting analog of a $p-n$ junction, and is highly sought after as a building block for superconducting electronics. Since the magnetization direction can be switched by a small field B_M (red and blue lines in Fig. 6.10a), the polarity of the current asymmetry can be switched, and the direction of the diode reversed, making it so programmable. We demonstrate the superconducting diode behavior in Fig. 6.10b, where we apply $|I| \approx 25$ nA and continuously switch the current direction. Simultaneous measurements of the device resistance show that the device is clearly resistive in one current direction and superconducting in the other, depending on the magnetization direction.

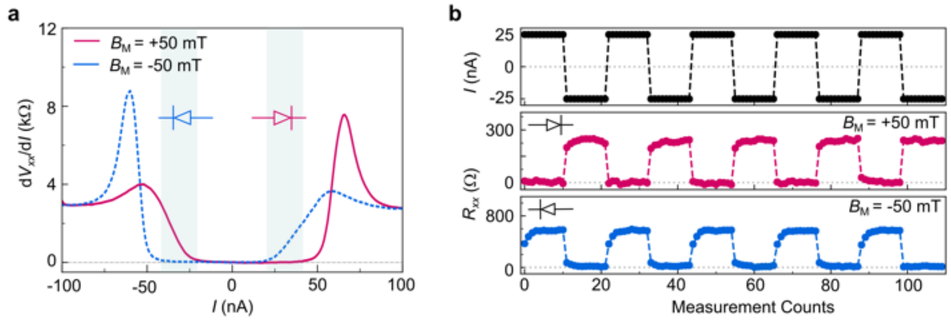

Figure 6.10: Zero-field switchable superconducting Josephson diode. **a,** $\mathrm{d}V_{xx}/\mathrm{d}I$ vs. I measured at 35 mK. All curves are taken at $B = 0$ mT after pre-magnetizing the sample at $B_M = +50$ mT (red) or $B_M = -50$ mT (blue). The shaded gray regions mark the values of current at which the diode behavior is observed. **b,** Switching between resistive and superconducting state by changing the direction of I as shown in the top panel. By applying opposite B_M, the diode behavior is inverted (red and blue curves).

While the superconducting diode effect has been previously realized in Rashba superconductors due to the magnetochiral anisotropy effect [160, 161], as well as in van der Waals JJs [162], the present device offers new capabilities as it is fully tunable and can be operated at zero magnetic field. The study of the superconducting diode can provide more information about the system. In particular, observing the superconducting diode at zero B field is a further proof of the broken inversion and time reversal symmetries [163]. After this work, there has been an experiment in twisted trilayer graphene which has also reported the observation of a superconducting diode effect at zero field. In that the case, they argued that the origin is most likely to come from an imbalance in the valley polarization of the bands [164]. Lastly, there has been follow up theoretical work on our experiment, where the observed superconducting diode effect can be explained by the valley polarization of the weak link [165].

6.5 Conclusion

To summarize, we have proved that time reversal symmetry broken states can coexist with superconductivity in a single MATBG device. The zero-field coexistence and gate tunability of the magnetic and topological phases with superconductors in MATBG presents a remarkable opportunity to electronically hybridize these phases through engineering of complex gate induced junctions. This will lead to the creation of ever more complex quantum phases based on the MATBG platform. Also, the so created JJs can shed new light on the underlying ground states of MATBG, as the JJ probes much smaller areas than traditional transport experiments and are highly sensitive to magnetic fields.

7 pn-junctions in MATBG

The main aim of this thesis is to develop gate-defined Josephson junctions in MATBG. In order to create the double gated structures the chosen metal for the gates was graphite. The main reason to choose graphite over an evaporated electrode such as Au was the fact that we can make an entire device composed of van der Waals layers which has been shown to give better cleanliness than having to evaporate an external metal [20]. From the possible ways to make a JJ, we decided to use a three gate approach (where the top gate is split in two), since this would allow for more flexibility in the experiments, allowing us to change the two sides of the junction independently. By keeping the back gate grounded $V_{BG} = 0$ V and tuning the two top gates independently, one can for example create a pn-junction. By studying the light induced response of the pn-junction, one can obtain information about the light-matter interaction in the material, which has not been widely studied so far [166, 167]. The advantages of using a pn-junction instead of just measuring the global Hall bar include that it allows to study the optoelectronic properties locally, it increases the response immensely and controlling the gates allows to understand the mechanism responsible of the response [168].

In this section we study the light-matter interaction of MATBG by looking at the cooling dynamics of the electrons upon light illumination. This allows us to extract information about the electron-phonon interactions in MATBG. We observe how the cooling rate at low T is faster in the twisted devices ($\theta = 1.24°$ and $\theta = 1.06°$) than in a non-twisted Bernal graphene sample by several orders of magnitudes [72]. While at low T the cooling time in the bilayer graphene takes nanoseconds due to the reduced acoustic phonons at low T, the measured times in the twisted samples remain in the picosecond range, even at 5 K. We argue that the increased cooling times are due to Umklapp scattering enabled by the mini-Brillouin zone, which allows to overcome the electron-phonon momentum mismatch.

First I will show the transport characterization of the pn-junction devices which are used for both experiments and then summarize the main results of the first experiment.

7.1 Transport characterization of the pn-junctions

The studied devices are all made in the same way as the ones used for the JJ experiments, consisting of hBN encapsulated double gated MATBG, which are fabricated into a Hall bar structure. In this chapter three different devices are used: one non-twisted device, one near magic angle device $\theta = 1.24°$ (device A) and a magic angle device $\theta = 1.06°$ (device B). Prior to performing the optoelectronic measurements, the devices are pre-characterized in transport at low T to extract the angle and study the transport pn-junction behavior by independently tuning the two top gates while keeping the back gate grounded $V_{BG} = 0$ V.

Fig. 7.1 shows the images of the two twisted devices and their R_{xx} vs. V_{BG} temperature and B field dependence. Both devices show typical features of a MATBG device, showing a sharp CNP, the BIs at full filling of the flat band and different CIs states at partial fillings of the band. Knowing which CIs are present in the devices is important to later understand the double gate maps when making the pn-junctions. In order to extract the twist angle the devices are measured vs. perpendicular magnetic field B at 1.8 K (Fig. 7.1e and f). From fitting the Landau levels as explained in Ch. 3 we can extract the twist angle of the devices.

7.1.1 Dual gated maps: pn-junction

In the previous chapter, we used the back gate and the two top gates together to define the JJ. In this case, we measure across the junction while individually sweeping each of the top gates while keeping the back gate grounded. By sweeping both gates, namely V_{TG1} and V_{TG2}, corresponding to each of the top gates, we can obtain the full phase space of the pn-junction device. Such maps are shown for Device A and B in Fig. 7.2, where the vertical features correspond to top gate 1 and the horizontal features to top gate two. The fact that the features are perpendicular to each other means that the gates are effectively decoupled. In both cases we observe a slight asymmetry between the two gates that is due to small twist angle differences between the left and right side of the junction, leading to not having exactly the same features on both sides. For device A, the map measures all the way to the BIs of both gates, which is shown as the red “frame” of the map. The features corresponding to CNP, $\nu = \pm 2$ and full filling are visible in both gates. However $\nu = \pm 3$ is only visible for V_{TG2}. For device B, the measurement is shown until just before the BIs, except for $\nu = +4$ of the

V_{TG1}. The features corresponding to CNP and $\nu = \pm 2$ are visible for both gate configurations, while $\nu = +3$ is shown only for V_{TG2} and $\nu = +1$ only appear for V_{TG1}.

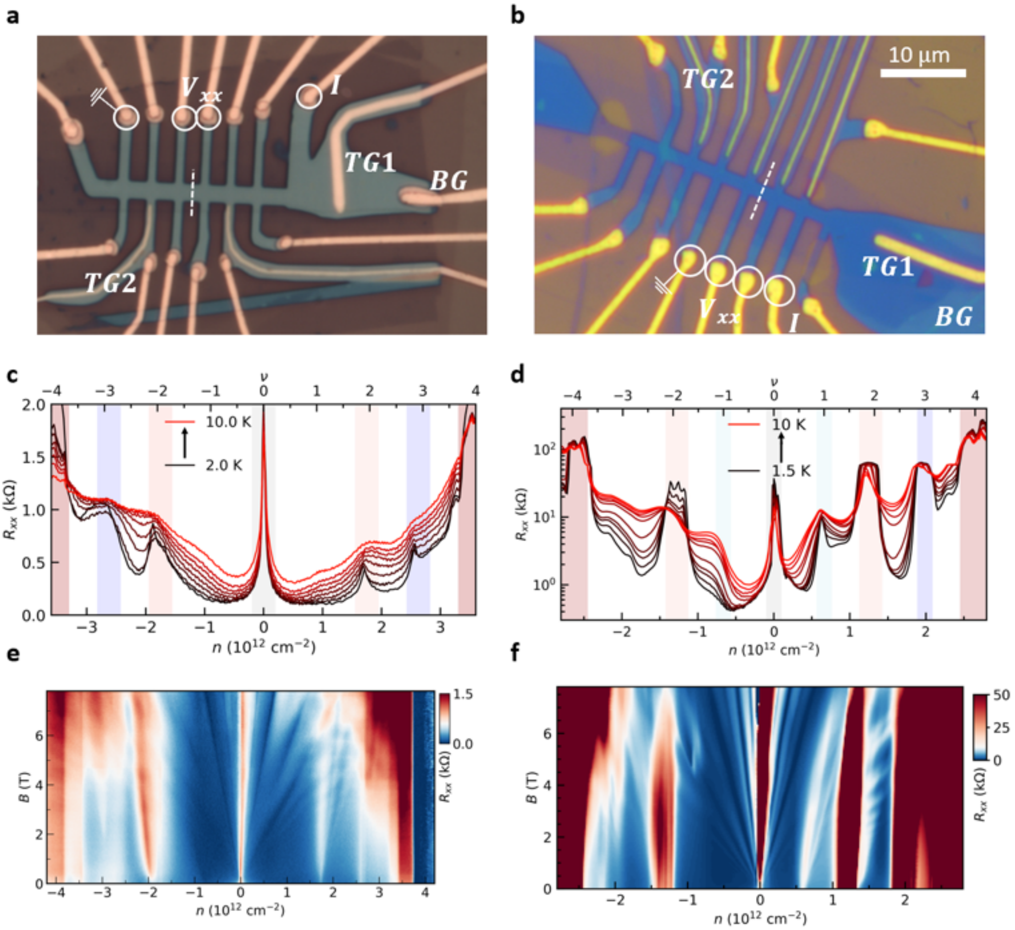

Figure 7.1: Device pictures and longitudinal resistance R_{xx} plots. **a,** Device a image. Measurement scheme is shown with the current bias I, longitudinal resistance contacts R_{xx}, the ground and the used gates V_{TG1} and V_{TG2}. **b,** Same scheme but for device B. **c, d,** Temperature dependence of R_{xx} vs. n for device A and B, respectively. The colored ranges mark the position of the different CIs in the sample. **e, f** Landau fan at 1.8 K for device A and B, respectively.

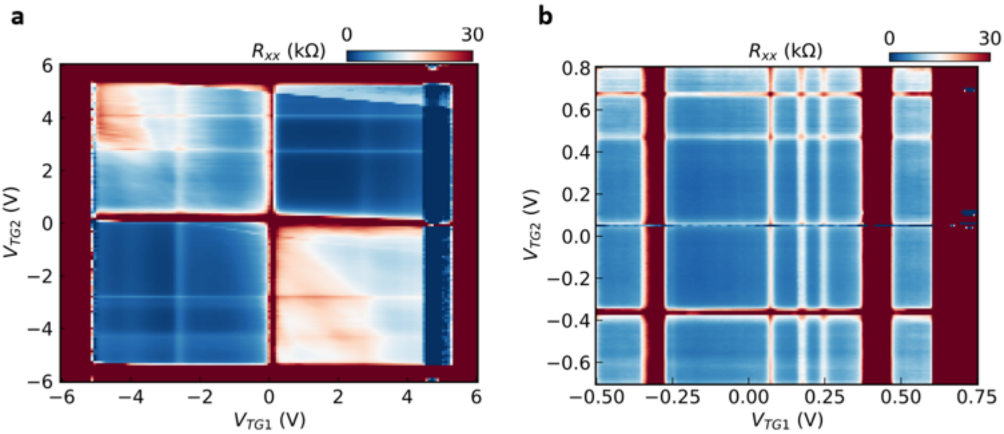

Figure 7.2: Dual top gate maps corresponding to Device A (a) and Device B (b). The vertical and horizontal features correspond to V_{TG1} and V_{TG2}, respectively. In device A we observe CNP ,$\nu = \pm 2$ and $pm4$ for both gates and ± 3 for V_{TG2}. In device B, we observe CNP and $\nu = \pm 2$ for both gates, while we observe $\nu = +3$ for V_{TG2} and $\nu = +1$ for V_{TG2}

.

7.2 Ultrafast Umklapp-assisted electron-phonon cooling in MATBG

After pre-characterizing the devices and extracting the twist angles, we can proceed to perform the optoelectronic experiments. The experiment is described here as presented in the work by Mehew *et al.* [72].

Electron-phonon coupling can be studied by using excited-state relaxation measurements, in which a laser is used to thermally excite the electrons. First, the electrons get thermally excited to a high energy state. The excited electrons will then thermalize to a hot carrier distribution (a Fermi-Dirac distribution at higher T than the original state) by electron-electron scattering. Finally, the hot electrons will cool down via electron-phonon interactions (acoustic, optical or substrate phonons) (see Fig. 7.3). Here we follow the convention of [169] where high-energy carriers are carrier without a well defined T (are not thermalized) and hot-carriers are the thermalized carriers. Importantly, all the cooling pathways happen in the order of ps at T_{room} but become less efficient and thus slower, as the T is lowered due to the de-population of phonons which effectively carry the heat away [169].

Here the cooling dynamics of MATBG are studied by exciting the electrons via illumination of a pn-junction (see Fig. 7.4a). When illuminating the

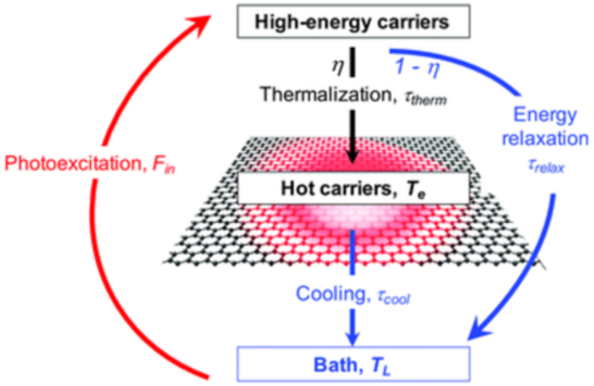

Figure 7.3: Schematic of cooling dynamics in graphene. a, Diagram explaining the different steps in the excitation-relaxation dynamics of electrons in graphene. η represents the heating efficiency and τ the timescale. **b,** Possible cooling pathway mechanism for hot carriers in graphene. Each process has a time constant τ. Figure adapted from [169].

MATBG pn-junctions, a photovoltage is developed via the phothermoelectric effect, which is proportional to the electron temperature T_e. The cooling dynamics of the MATBG electrons are studied using two independent techniques: time-resolved photovoltage (TrPV) microscopy [170, 171] and continuous wave photomixing (CW-PM) [172, 173]. In both techniques, the detuning between two laser beams, either in real time or in the frequency domain, is used to directly probe the cooling dynamics of the sample. In the TrPV technique, the delay time between two ultrashort pulses (ns pulses) is varied. Due to the sub-linear response between carrier temperature and optical heating, a dip in the photovoltage is observed when the two pulses arrive at the same time ($dt = 0$). At longer delay times, the signal recovers to its maximal value. The cooling time is obtained by describing the observed dynamics with an exponential function. In the CW-PM, the wavelength detuning between two CW lasers creates an optical beating, which makes the photovoltage oscillate at the beating frequency Ω. Due to the competition between the beat frequency and the characteristic cooling time τ_e, a peak is observed for $\Omega = 0$ whereas the oscillations are damped when $\Omega^{-1} << \tau_e$. The frequency response takes the form of a Lorentzian function of width Γ, from which the cooling time is extracted as: $\Gamma = 1/\pi\tau_e$. If the system is not able to cool down in between the laser pulses, it will heat up less in each pulse due to the reduced heat capacity, therefore a damping is observed. Combining both techniques is very interesting, because TrPV is more accurate for longer time delays, while the CW-PM is more accurate

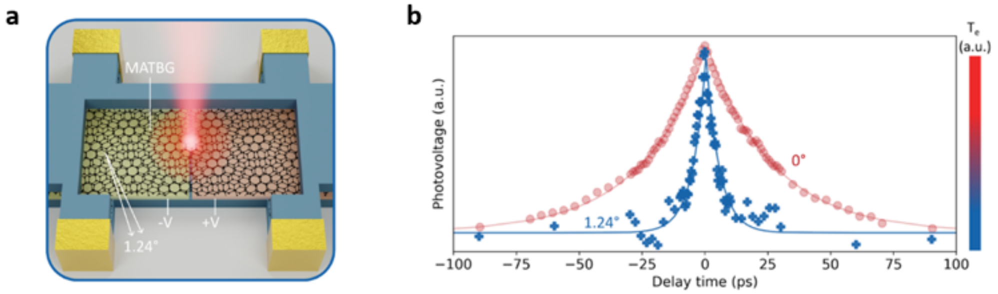

Figure 7.4: MATBG vs. BLG pn-junction response under light illumination. a, Schematic showing a MATBG device equipped with split gates. **b,** Comparison of the cooling dynamics (measured as photovoltage) of a Bernal bilayer sample (0°) and a close to magic angle sample (1.24°) at $T = 25$ K. Figure adapted from [72].

for very short delays (since it works in the frequency domain).

The main experiments are done comparing Device A with a non-twisted Bernal bilayer graphene (BLG) sample. Both experiments show a much faster cooling in the MATBG at low T (down to 5 K) as shown in Fig. 7.4. In the BLG sample the cooling time is reduced from 3 to 25 ps when going from 300 to 5 K, as is expected due to reduced phonon occupation at low T [174, 175]. However, the MATBG samples shows an almost constant response in the 3 ps regime (see Fig. 7.5a), which suggest the involvement of low energy phonons which are still occupied at low T. Such phonons could be induced by the breaking of the phonon dispersion into minibands due to the moiré superlattice [176].

In order to better understand the origin of the ultrafast cooling, the spot size, laser power and filling factors are varied (see Fig. 7.5b-d).

- The first test is whether the cooling could be happening via a diffusive cooling mechanism [169, 177]. Such diffusive cooling would show increasing cooling times for larger laser spot sizes and an increase of the cooling times with lowering T. In the experiments, the MATBG has no dependence on the laser spot size, while the BLG sample has a clear spot size dependence, pointing towards a diffusive cooling mechanism (Fig. 7.5c). This observation that cooling in MATBG is independent of lattice temperature implies that a more efficient mechanism than diffusive cooling is responsible for the cooling dynamics.
- Next, we check whether the cooling depends on the initial T of the electrons. A higher laser power equates to having a higher initial

electron temperature, such that there is more population in the higher energy bands, the dispersive bands in the case of MATBG. In BLG it has been seen how higher power ends up giving slower cooling times, due to bottlenecks of acoustic and optical phonons limiting the cooling process [178]. However the cooling times in MATBG are rather non-dependent on the power, meaning that the limiting factors found in BLG do not apply to it (Fig. 7.5b). The faster cooling rate in MATBG and its independence on electron T means that a different mechanism is dominating the cooling, compared to the known mechanisms found in non-twisted graphene.

- Finally, the cooling in MATBG is measured across the whole band to explore the effect of the superlattice (Fig. 7.5d). The MATBG shows an almost constant cooling time of 3 ps across the entire flat band which experiences a large increase around the full filling of the band, at $\nu = \pm 4$. Such an increase indicates how the moiré pattern and its low energy phonons are crucial to explain the ultrafast cooling in MATBG.

7.2.1 Discussion

To better understand the origin of the ultra-fast cooling, the microscopic electron-phonon scattering processes are studied in a four-band model consisting of two nearly-flat and two dispersive bands. The model considers two main types of scattering processes: intraband and interband. It is shown (see [72] for details) how when considering Umklapp and normal scattering contributions, electron-phonon Umklapp scattering consistently dominates at the low T regime of interest ($T < 10$ K). Furthermore, the calculated Umklapp-assisted cooling times as a function of filling factor are in agreement with the experimental results.

The appearance of this novel Umklapp scattering mechanism relies on the moiré pattern of the superlattice in the twisted graphene. That is because in order for this Umklapp scattering to occur, it requires a small superlattice Brillouin zone, spatially-compressed Wannier orbitals and low energy moiré phonons. The fact that electron-phonon Umklapp scattering dominates the ultrafast electron-phonon cooling, can help understand better the MATBG physics, since electron-phonon scattering plays an important role in charge transport. Understanding this mechanism could help understand some of the open question in MATBG field such as the strange metal phase or the role of phonons in the superconductivity.

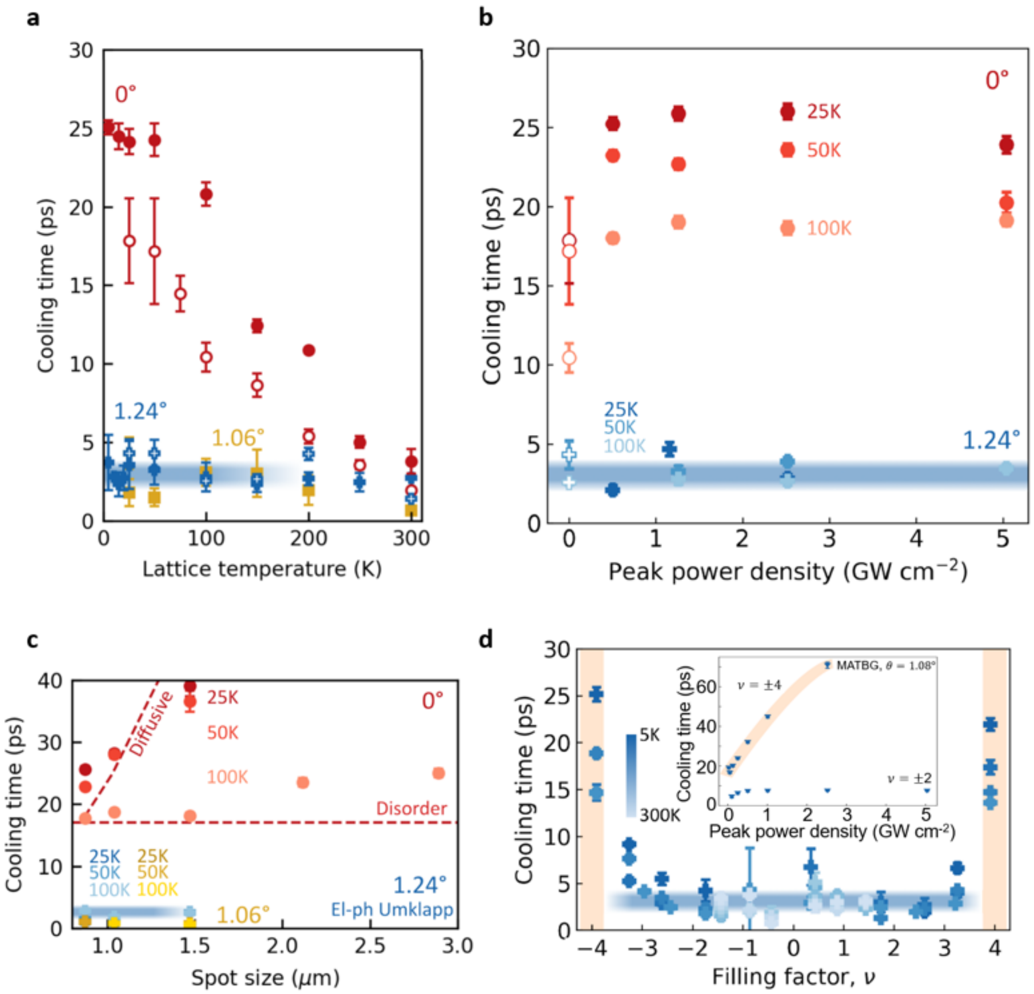

Figure 7.5: Optical measurements of the MATBG pn junctions. a, Cooling time as a function of lattice temperature. In MATBG (1.24°in blue and 1.06°, in yellow), the cooling time is constant between 5 K and 300 K (3 ps, blue line). For BLG (0°, red circles), it is greater at lower temperatures. **b,** Dependence of cooling time on peak power density for BLG (red circles) and MATBG (blue pluses, device A). The filled (open) shapes are measured using the TrPV (CW-PM) technique. The error bars signify the one sigma confidence interval from the fitting algorithm. **c,** Laser spot size dependence of the cooling time for the three devices. **d,** Gate dependence of cooling time of device A. The inset shows the increasing cooling time with power density at full filling of the band for device B. The thick blue line in all the figures represents the cooling time obtained from the-low temperature model of Umklapp-assisted cooling. Figure adapted from [72].

8 Conclusions and outlook

In this thesis, we have developed gate-defined JJs in MATBG by taking advantage of its rich phase space and using all van der Waals materials. We have found that the MATBG JJs offer great tunability with carrier density. We have shown how small changes in gate voltage allows to tune from a conventional JJ to a highly unconventional one, showing broken inversion and time reversal symmetries. This tunability can offer a large potential to develop superconducting circuits, in which different components could be made of a single material. Furthermore, by changing the conditions of the device (namely T and gate voltage) we can even create completely different types of devices, such as a pn-junction.

In Ch. 3 and 4 we successfully developed and optimized the recipes to fabricate high quality MATBG gate-defined JJs. We found some key parameters which improve the fabrication of the devices. These include, for example, the use of thin hBN ($<$ 15 nm) during the stacking or the “clamping” of the graphene layers. In the case of double-graphite-gated junction devices, we have also showed the importance of the relative sizes between the hBN and graphene, as well as, the relative widths between the top and bottom gates.

Then, in Ch. 5 we explored the behavior and gate-tunability of the created JJs. In Ch. 6 we focused on the case of having the weak link of the junction close to the correlated state at $\nu = -2$ filling factor, showing a symmetry-broken JJ with a highly unconventional behavior under the application of magnetic field. We have observed a magnetic hysteresis, which allows to have a magnetic JJ, as well as define a tunable superconducting diode at zero-field. These results have let us conclude that this state has a broken inversion and time-reversal symmetry, which helps to frame its possible ground states. Furthermore this result suggests the potential of MATBG for quantum technologies, as it allows to create complex JJs within a single material. For example, the development of a tunable superconducting diode at zero-field in a single material has great potential for low power electronics.

Finally, in Ch. 7, we showed how due to the richness of the MATBG system and the way the junctions were made, it was possible to directly create gate-defined pn-junctions. We have used the pn-junctions to study the light-matter interaction of the system. By exploring the cooling dynamics of the MATBG compared to Bernal bilayer graphene, we have found that a new mechanism, namely electron-phonon Umklapp scattering, dominates the cooling at low T (∼5 K). This mechanism is directly related to the moire superlattice and it may help understand the role of phonons in the appearance of certain phases such as the strange metal or the superconductivity.

During the development of these thesis there have been similar experiments exploring gate-defined structures in the MATBG system. While we were working towards the fabrication of the JJs, Rodan-Legrain *et al.* [135] and De Vries [179] *et al.* published the first results in gate-defined JJs in MATBG. These works definitely proved the phase coherence of the superconducting state and the possibility to create gate-defined devices in the system. In the work of Rodan-Legrain *et al.* [135] they also showed how the junctions could be used to perform tunneling spectroscopy of the SC state or to create a quantum dot, showing the large tunability of the system. However, none of these works thoroughly studied the proximity effect on the correlated insulating states.

Other gate-defined experiments which have been made in these years are the measurement of a gate-defined SQUID [180] and measurements of Little-Parks effect in a gated ring architecture [181]. Both of these experiments had the goal to directly study the superconducting state and managed to prove long phase coherence lengths (reaching several µm [181]) of the electrons in the MATBG system. However, they also showed the complexity that arises in interpreting these complex gate-defined devices, as the size and exact states in the weak link are dependent on the gating structure (as we also showed in Fig. 5.6). Finally, all of these works have used Au electrodes to define the junctions, leaving our approach the only graphite gate-defined junctions in MATBG so far.

Apart from the gate-defined experiments, in the past few years the twisted graphene field has undergone an incredible growth, both on the experimental and theoretical side. In particular, superconductivity has not only been discovered in a wider twisted graphene family, including twisted trilayer (MATTG), quatrilayer (MATQG) and pentalayer graphene (MATPG) [182, 183, 184, 185, 186]. but also in non-moiré systems like ABC rhombohedral [99] and even regular Bernal bilayer graphene [187, 188].

Despite all these developments, the underlying mechanisms governing the SC state in the graphene family remain elusive. While scanning tunneling microscopy (STM) experiments have suggested an unconventional superconducting state in TBG [189] and TTG [190], and there are several theories proposing different scenarios [191, 192], no consensus has been reached yet. The emergence of superconductivity in non-moiré systems, reopens the question of which is the main parameter responsible for it. The common characteristic between these materials, apart from their carbon composition, is the presence of flatbands. Consequently, there is a growing interest in understanding the superconductivity within the flatband regime [193, 194, 195]. This interest, is further emphasized due to the presence of flatbands at the Fermi level in other twisted vdW materials, which might also host superconducting states [196]. Although here we focus mostly on the superconductivity, the same applies for the other correlated states in MATBG, whose ground states and origin is still under debate. Finally, the recently developed quantum twisting microscope (QTM) [197], which allows to in-situ change the twist angle between the layers of 2D materials, may play a key role in the understanding of twisted systems in the following years.

8.1 JJs follow-up

One of the realizations during this thesis was that making the JJs was not only a tool which could be used towards understanding the superconductor, but that it could also be used to study the other correlated states. Although we only measured the state at $\nu = -2$, in principle one could study all the other CI states, such as the magnetic states found at $\nu = +1, +3$. A limitation we found with the gate-defined architecture, was the growth of the junction size as the difference in the carrier density between the junction and electrodes ($|n_J - n|$) increases. This, combined with the appearance of small regions with different states inside the junction, diminishes the proximity effect (Fig. 5.6). This effect is detrimental to measure the correlated insulator states far from the superconducting state. A solution to this issue could be to use another s-wave SC to create the junctions. In that case, the superconductivity would be originating from the deposited electrodes and the gate would only change the carrier density of the junction n_J.

Within this same context, simply understanding the interface between the s-wave SC and the MATBG SC, could also be quite interesting as there are yet not many studies on the interface between 2D and 3D superconductors [198]. Understanding this interface would be a necessary step for some key experiments, those which would aim to measure the order parameter. Measuring the order parameter of the MATBG SC would be one of the key milestones to better understand the origin of its SC [192]. Knowing the symmetries of the order parameter, both in magnitude and phase, can put boundaries into the electrons involved in the formation of the Cooper-pairs, yielding light into the mechanisms responsible for the superconductivity.

The most promising architecture for such experiments is to measure a corner junction [97] in which the unknown SC is contacted from different directions with a known s-wave SC. However, these experiments might be extremely complicated in the case of MATBG, due to the angle inhomogeneity intrinsic to the samples [116, 159]. In the order parameter experiments it is essential that the direction of the tunneling is perfectly known. For example, in the case of high-T_c SCs the experiments were performed along crystallographic axis of a single crystal of the unknown material [96]. Although this does not exclude the possibility of such experiments, it would mean that several devices would be needed in order to have proper statistics of the measured signatures. For these experiments, the QTM might be a valuable tool. It could make easier some proposals to measure the order parameter, such as the vertical JJs between two rotated MATBG devices proposed by Lake *et al.*[192], which are extremely challenging to do in transport .

Finally, we propose some improvements on the graphite-gated devices. As we found in this thesis, properly defining the junction area is a key parameter to have high quality JJs in the MATBG system. In the past few years, an interesting technique to etch graphite has been developed: local anodic oxidation lithography [199, 200]. In the anodic oxidation, the graphite is electrochemically etched using a conductive atomic force microscope (AFM) cantilever, obtaining features down to 50 nm width. It has been recently shown, how using graphite gates shaped with local anodic oxidation can further improve the quality of the graphene devices, compared to using dry etching techniques [201]. Therefore, using the local anodic oxidation technique to create gate-defined JJs or other structures, may allow to observe new physics that might be obscured by the fabrication process. At the same time, the graphite flakes etched this way remain clean of residues and can be easily picked up with a polymer stamp, thus easing the fabrication process. Furthermore, the fact that the etched graphite is clean and can be easily picked up with a stamp [201] would mean that it does not need to be the top layer of the stack. This offers the interesting possibility of creating structures in which both the displacement field D and the carrier density n can be tuned (semi-) independently even in a junction architecture. This is an essential requirement in order to fabricate JJs in any of the other members of the superconducting graphene family, since they all have a dependence with D field. This opens up interesting avenues, since, for example, topological JJs hosting Majorana fermions have been predicted to form in the case of gate-defined bilayer graphene stabilized with WSe_2 [202].

8.2 Final notes on vdW heterostructures

While the field of van der Waals materials and twistronics offers immense opportunities to study new materials and their properties, the fabrication of complex high-quality reproducible devices is still limiting the advancement of the field [203]. Although efforts are being made towards improving the reliability in the fabrication, for example by the automatization of the stacking process [204, 205] or developing assembly processes in high vacuum for improving the cleanliness [206], a deeper understanding of the subtleties of the stacking process is needed to progress further in that direction. The thorough investigation and understanding of which parameters are key in the fabrication process of high quality devices (as was the aim of the detailed explanations of Ch. 3) is a necessary step towards the understanding of which properties are intrinsic to the material or extrinsic from the fabrication process. This understanding could allow to eventually achieve a standardization of devices. The advances in the stacking process would be a great leap forwards in the investigation not only of MATBG, but of any other complex heterostructures which might otherwise present large variability in their phase diagrams. In this way, gaining full control over the fabrication would provide the opportunity to explore and understand a, potentially, infinite combination of materials.

References

[1] Novoselov, K. S. *et al.* Electric field effect in atomically thin carbon films. *Science* **306**, 666–669 (2004).

[2] Mermin, N. D. Crystalline order in two dimensions. *Physical Review* **176** (1968).

[3] Lee, C., Wei, X., Kysar, J. W. & Hone, J. Measurement of the elastic properties and intrinsic strength of monolayer graphene. *Science* **321**, 385–388 (2008).

[4] Balandin, A. A. *et al.* Superior thermal conductivity of single-layer graphene. *Nano Letters* **8**, 902–907 (2008).

[5] Novoselov, K. S. *et al.* Room-temperature quantum hall effect in graphene. *Science* **315**, 1379 (2007).

[6] Novoselov, K. S. *et al.* Two-dimensional gas of massless dirac fermions in graphene. *Nature* **438**, 197–200 (2005).

[7] Zhang, Y., Tan, Y. W., Stormer, H. L. & Kim, P. Experimental observation of the quantum hall effect and berry's phase in graphene. *Nature* **438**, 201–204 (2005).

[8] Katsnelson, M. I., Novoselov, K. S. & Geim, A. K. Chiral tunnelling and the klein paradox in graphene. *Nature Physics* **2**, 620–625 (2006).

[9] Novoselov, K. S. *et al.* Two-dimensional atomic crystals. *Proceedings of the National Academy of Sciences* **102**, 10451–10453 (2005).

[10] Geim, A. K. & Grigorieva, I. V. Van der waals heterostructures. *Nature* **499**, 419–425 (2013).

[11] Dean, C. R. *et al.* Boron nitride substrates for high-quality graphene electronics. *Nature Nanotechnology* **5**, 722–726 (2010).

[12] Radisavljevic, B., Radenovic, A., Brivio, J., Giacometti, V. & Kis, A. Single-layer mos_2 transistors. *Nature Nanotechnology* **6**, 147–150 (2011).

[13] Fei, Z. *et al.* Edge conduction in monolayer wte_2. *Nature Physics* **13**, 677–682 (2017).

[14] Xi, X. *et al.* Ising pairing in superconducting nbse2 atomic layers. *Nature Physics* **12**, 139–143 (2015).

[15] Huang, B. *et al.* Layer-dependent ferromagnetism in a van der waals crystal down to the monolayer limit. *Nature* **546**, 270–273 (2017).

[16] Novoselov, K. S., Mishchenko, A., Carvalho, A. & Neto, A. H. C. 2d materials and van der waals heterostructures. *Science* **353** (2016).

[17] Mayorov, A. S. *et al.* Micrometer-scale ballistic transport in encapsulated graphene at room temperature. *Nano Letters* **11**, 2396–2399 (2011).

[18] Ponomarenko, L. A. *et al.* Tunable metal–insulator transition in double-layer graphene heterostructures. *Nature Physics* **7** (2011).

[19] Kretinin, A. V. *et al.* Electronic properties of graphene encapsulated with different two-dimensional atomic crystals. *Nano Letters* **14**, 3270–3276 (2014).

[20] Hunt, B., Taniguchi, T., Moon, P., Koshino, M. & Ashoori, R. C. Massive dirac fermions and. *Science* **340**, 1427–1431 (2013).

[21] Wang, L. *et al.* One-dimensional electrical contact to a two-dimensional material. *Science* **342**, 614–617 (2013).

[22] Bolotin, K. I. *et al.* Ultrahigh electron mobility in suspended graphene. *Solid State Communications* **146**, 351–355 (2008).

[23] Avsar, A. *et al.* Spin-orbit proximity effect in graphene. *Nature Communications* **5** (2014).

[24] Efetov, D. K. *et al.* Specular interband andreev reflections at van der waals interfaces between graphene and $NbSe_2$. *Nature Physics* **12**, 328–332 (2016).

[25] Richard, F. There's plenty of room at the bottom. *Engineering and Science* **23**, 22–26 (1960).

[26] Carr, S., Fang, S., Jarillo-Herrero, P. & Kaxiras, E. Pressure dependence of the magic twist angle in graphene superlattices. *Physical Review B* **98**, 85144 (2018).

[27] Park, C. H., Yang, L., Son, Y. W., Cohen, M. L. & Louie, S. G. Anisotropic behaviours of massless dirac fermions in graphene under periodic potentials0. *Nature Physics* **4**, 213–217 (2008).

[28] Li, G. *et al.* Observation of van hove singularities in twisted graphene layers. *Nature Physics* **6**, 109–113 (2010).

[29] Yankowitz, M. *et al.* Emergence of superlattice dirac points in graphene on hexagonal boron nitride. *Nature Physics* **8**, 382–386 (2012).

[30] Ponomarenko, L. A. *et al.* Cloning of dirac fermions in graphene superlattices. *Nature* **497**, 594–597 (2013).

[31] Dean, C. R. *et al.* Hofstadter's butterfly and the fractal quantum hall effect in moiré superlattices. *Nature* **497**, 598–602 (2013).

[32] Yu, G. L. *et al.* Hierarchy of hofstadter states and replica quantum hall ferromagnetism in graphene superlattices. *Nature Physics* **10**, 525–529 (2014).

[33] Santos, J. M. B. L. D., Peres, N. M. R. & Neto, A. H. C. Graphene bilayer with a twist: Electronic structure. *Physical Review Letters* **99** (2007).

[34] Bistritzer, R. & MacDonald, A. H. Moiré bands in twisted double-layer graphene. *Proceedings of the National Academy of Sciences of the United States of America* **108**, 12233–12237 (2011).

[35] Shima, N. & Aoki, H. Electronic structure of superhoneycomb systems: A peculiar realization of semimetal/semiconductor classes and ferromagnetism. *Physical Review Letters* **71**, 4389–4392 (1993).

[36] Lee, P. A., Nagaosa, N. & Wen, X. G. Doping a mott insulator: Physics of high-temperature superconductivity. *Reviews of Modern Physics* **78** (2006).

[37] Cao, Y. *et al.* Superlattice-induced insulating states and valley-protected orbits in twisted bilayer graphene. *Physical Review Letters* **117** (2016).

[38] Kim, K. *et al.* Van der waals heterostructures with high accuracy rotational alignment. *Nano Letters* **16**, 1989–1995 (2016).

[39] Cao, Y. *et al.* Correlated insulator behaviour at half-filling in magic-angle graphene superlattices. *Nature* **556**, 80–84 (2018).

[40] Cao, Y. *et al.* Unconventional superconductivity in magic-angle graphene superlattices. *Nature* **556**, 43–50 (2018).

[41] Das, I. *et al.* Symmetry-broken chern insulators and rashba-like landau-level crossings in magic-angle bilayer graphene. *Nature Physics* **17**, 710–714 (2021).

[42] Sharpe, A. L. *et al.* Evidence of orbital ferromagnetism in twisted bilayer graphene aligned to hexagonal boron nitride. *Nano Lett* **21**, 4299–4304 (2021).

[43] Yankowitz, M. *et al.* Tuning superconductivity in twisted bilayer graphene. *Science* **363**, 1059–1064 (2019).

[44] Lu, X. *et al.* Superconductors, orbital magnets, and correlated states in magic angle bilayer graphene. *Nature* **574**, 653 (2019).

[45] Codecido, E. *et al.* Correlated insulating and superconducting states in twisted bilayer graphene below the magic angle. *Science Advances* **5** (2019).

[46] Zondiner, U. *et al.* Cascade of phase transitions and dirac revivals in magic-angle graphene. *Nature* **582**, 203–208 (2020).

[47] Wong, D. *et al.* Cascade of electronic transitions in magic-angle twisted bilayer graphene. *Nature* **582**, 198–202 (2020).

[48] Stepanov, P. *et al.* Untying the insulating and superconducting orders in magic-angle graphene. *Nature* **583**, 375–378 (2020).

[49] Saito, Y., Ge, J., Watanabe, K., Taniguchi, T. & Young, A. F. Independent superconductors and correlated insulators in twisted bilayer graphene. *Nature Physics* **16**, 926–930 (2020).

[50] Serlin, M. *et al.* Intrinsic quantized anomalous hall effect in a moiré heterostructure. *Science* **367**, 900–903 (2020).

[51] Sharpe, A. L. *et al.* Emergent ferromagnetism near three-quarters filling in twisted bilayer graphene. *Science* **365**, 605–608 (2019).

[52] Nuckolls, K. P. *et al.* Strongly correlated chern insulators in magic-angle twisted bilayer graphene. *Nature* **588**, 610–615 (2020).

[53] Wu, S., Zhang, Z., Watanabe, K., Taniguchi, T. & Andrei, E. Y. Chern insulators, van hove singularities and topological flat bands in magic-angle twisted bilayer graphene. *Nature Materials* **20**, 488–494 (2021).

[54] Saito, Y. *et al.* Hofstadter subband ferromagnetism and symmetry-broken chern insulators in twisted bilayer graphene. *Nature Physics* **17**, 478–481 (2021).

[55] Cao, Y. *et al.* Strange metal in magic-angle graphene with near planckian dissipation. *Phys. Rev. Lett.* **124**, 076801 (2020).

[56] Polshyn, H. *et al.* Large linear-in-temperature resistivity in twisted bilayer graphene. *Nature Physics* **15**, 1011–1016 (2019).

[57] Jaoui, A. *et al.* Quantum critical behaviour in magic-angle twisted bilayer graphene. *Nature* 1–6 (2022).

[58] Thinkham, M. *Introduction to Superconductivity* (McGraw-Hill, Inc., 1996), second edn.

[59] Balents, L., Dean, C. R., Efetov, D. K. & Young, A. F. Superconductivity and strong correlations in moiré flat bands. *Nature Physics* **16**, 725–733 (2020).

[60] Bergeret, F. S., Volkov, A. F. & Efetov, K. B. Odd triplet superconductivity and related phenomena in superconductor-ferromagnet structures. *Reviews of Modern Physics* **77**, 1321–1373 (2005).

[61] Keizer, R. S. *et al.* A spin triplet supercurrent through the half-metallic ferromagnet cro 2. *Nature* **439**, 825–827 (2006).

[62] Robinson, J. W. A., Witt, J. D. S. & Blamirem, M. G. Controlled injection of spin-triple supercurrents into a strong ferromagnet. *Science* **329**, 1348–1352 (2008).

[63] Ryazanov, V. V. *et al.* Coupling of two superconductors through a ferromagnet: Evidence for a π junction. *Physical Review Letters* **86**, 2427–2430 (2001).

[64] Oboznov, V. A., Bol'ginov, V. V., Feofanov, A. K., Ryazanov, V. V. & Buzdin, A. I. Thickness dependence of the josephson ground states of superconductor- ferromagnet-superconductor junctions. *Physical Review Letters* **96** (2006).

[65] Robinson, J. W., Piano, S., Burnell, G., Bell, C. & Blamire, M. G. Zero to π transition in superconductor-ferromagnet-superconductor junctions. *Physical Review B - Condensed Matter and Materials Physics* **76** (2007).

[66] Wiedenmann, J. *et al.* 4π-periodic josephson supercurrent in hgte-based topological josephson junctions. *Nature Communications* **7** (2016).

[67] Bocquillon, E. *et al.* Gapless andreev bound states in the quantum spin hall insulator hgte. *Nature Nanotechnology* **12**, 137–143 (2017).

[68] Li, C. *et al.* 4π-periodic andreev bound states in a dirac semimetal. *Nature Materials* **17**, 875–880 (2018).

[69] Linder, J. & Robinson, J. W. Superconducting spintronics. *Nature Physics* **11**, 307–315 (2015).

[70] Alicea, J. New directions in the pursuit of majorana fermions in solid state systems. *Reports on Progress in Physics* **75**, 76501–36 (2012).

[71] Díez-Mérida, J. *et al.* Symmetry-broken josephson junctions and superconducting diodes in magic-angle twisted bilayer graphene. *Nature Communications* **14**, 1–7 (2023).

[72] Mehew, J. D. *et al.* Ultrafast umklapp-assisted electron-phonon cooling in magic-angle twisted bilayer graphene. *Preprint: arXiv2301.13742.* (2023).

[73] Randviir, E. P., Brownson, D. A. & Banks, C. E. A decade of graphene research: production, applications and outlook. *Materials Today* **17**, 426–432 (2014).

[74] Wallace, P. R. The band theory of graphite. *Physical Review* **71**, 622–634 (1947).

[75] Neto, A. H. C., Guinea, F., Peres, N. M., Novoselov, K. S. & Geim, A. K. The electronic properties of graphene. *Reviews of Modern Physics* **81**, 109–162 (2009).

[76] Sarma, S. D., Adam, S., Hwang, E. H. & Rossi, E. Electronic transport in two-dimensional graphene. *Reviews of Modern Physics* **83**, 407–470 (2011).

[77] Haldane, F. D. Model for a quantum hall effect without landau levels: Condensed-matter realization of the ”parity anomaly”. *Physical Review Letters* **61**, 2015–2018 (1988).

[78] McCann, E. & Koshino, M. The electronic properties of bilayer graphene. *Reports on Progress in Physics* **76**, 056503 (2013).

[79] Zhang, Y. *et al.* Direct observation of a widely tunable bandgap in bilayer graphene. *Nature* **459**, 820–823 (2009).

[80] Trauzettel, B., Bulaev, D. V., Loss, D. & Burkard, G. Spin qubits in graphene quantum dots. *Nature Physics* **3**, 192–196 (2007).

[81] Zou, L., Po, H. C., Vishwanath, A. & Senthil, T. Band structure of twisted bilayer graphene: Emergent symmetries, commensurate approximants, and wannier obstructions. *Physical Review B* **98**, 85435 (2018).

[82] Tarnopolsky, G., Kruchkov, A. J. & Vishwanath, A. Origin of magic angles in twisted bilayer graphene. *Physical Review Letters* **122** (2019).

[83] Mele, E. J. Commensuration and interlayer coherence in twisted bilayer graphene. *Physical Review B - Condensed Matter and Materials Physics* **81** (2010).

[84] Moon, P. & Koshino, M. Energy spectrum and quantum hall effect in twisted bilayer graphene. *Physical Review B - Condensed Matter and Materials Physics* **85**, 195458 (2012).

[85] Lopes, J. M. B., Santos, D., Peres, N. M. R. & Neto, A. H. C. Continuum model of the twisted graphene bilayer. *Physical review B* **86**, 155449 (2012).

[86] Morell, E. S., Correa, J. D., Vargas, P., Pacheco, M. & Barticevic, Z. Flat bands in slightly twisted bilayer graphene: Tight-binding calculations. *Physical Review B - Condensed Matter and Materials Physics* **82** (2010).

[87] Choi, Y. *et al.* Electronic correlations in twisted bilayer graphene near the magic angle. *Nature Physics 2019 15:11* **15**, 1174–1180 (2019).

[88] Liu, J., Ma, Z., Gao, J. & Dai, X. Quantum valley hall effect, orbital magnetism, and anomalous hall effect in twisted multilayer graphene systems. *Physical Review X* **9** (2019).

[89] Bultinck, N. *et al.* Ground state and hidden symmetry of magic-angle graphene at even integer filling. *Physical Review X* **10** (2020).

[90] Stepanov, P. *et al.* Competing zero-field chern insulators in superconducting twisted bilayer graphene. *Physical Review Letters* **127** (2021).

[91] Park, J. M., Cao, Y., Watanabe, K., Taniguchi, T. & Jarillo-Herrero, P. Flavour hund's coupling, chern gaps and charge diffusivity in moiré graphene. *Nature* **592**, 43–48 (2021).

[92] Bardeen, J., Cooper, L. N. & Schrieffer, J. Theory of superconductivity. *Physical Review* **108**, 1175–1204 (1957).

[93] Sigrist, M. Introduction to unconventional superconductivity. *AIP Conference Proceedings* **789**, 165–243 (2005).

[94] Scalapino, D. J. A common thread: The pairing interaction for unconventional superconductors. *Reviewsn of Modern Physics* **84**, 1383 (2012).

[95] Harlingen, D. J. V. Phase-sensitive tests of the symmetry of the pairing state in the high-temperature superconductors evidence for $d_{x^2-y^2}$ symmetry. *Review of Moden Physics* **67** (1995).

[96] Wollman, D. A., Harlingen, D. J. V., Giapintzakis, J. & Ginsberg, D. M. Evidence for $d_{x^2-y^2}$ pairing from the magnetic field modulation of $YBa_2Cu_3O_7 - Pb$ josephson junctions. *Physical Review Letters* **74**, 797–800 (1995).

[97] Tsuei, C. C. & Kirtley, J. R. Pairing symmetry in cuprate superconductors. *Reviews of Modern Physics* **72** (2000).

[98] Bednorz, J. G. & Müller, K. A. Possible high tc superconductivity in the ba-la-cu-o system. *Zeitschrift für Physik B Condensed Matter* **64**, 189–193 (1986).

[99] Zhou, H., Xie, T., Taniguchi, T., Watanabe, K. & Young, A. F. Superconductivity in rhombohedral trilayer graphene. *Nature* **598**, 434–438 (2021).

[100] Basov, D. N. & Chubukov, A. V. Manifesto for a higher t_c. *Nature Physics* **7**, 272–276 (2011).

[101] Xu, C. & Balents, L. Topological superconductivity in twisted multilayer graphene. *Physical Review Letters* **121** (2018).

[102] Josephson, B. Possible new effects in superconductive tunnelling. *Physics Letters* **1** (1962).

[103] Pearl, J. Current distribution in superconducting films carrying quantized fluxoids. *Applied Physics Letters* **5**, 65–66 (1964).

[104] Berezinskit, V. L. Destruction of long-range order in one-dimensional and two-dimensional systems having a continuous symmetry group: Ii quantum systems. *Soviet Physics JETP* **34** (1972).

[105] Kosterlitz, J. M. & Thouless, D. J. Long range order and metastability in two dimensional solids and superfluids. (application of dislocation theory). *J. Phys. C: Solid State Phys.* **5** (1972).

[106] Brun, C., Cren, T. & Roditchev, D. Review of 2d superconductivity: The ultimate case of epitaxial monolayers. *Superconductor Science and Technology* **30**, 1–32 (2017).

[107] Moshe, M., Kogan, V. G. & Mints, R. G. Edge-type josephson junctions in narrow thin-film strips. *Physical Review B - Condensed Matter and Materials Physics* **78** (2008).

[108] Clem, J. R. Josephson junctions in thin and narrow rectangular superconducting strips. *Physical Review B - Condensed Matter and Materials Physics* **81** (2010).

[109] Boris, A. A. *et al.* Evidence for nonlocal electrodynamics in planar josephson junctions. *Physical Review Letters* **111** (2013).

[110] Castellanos-Gomez, A. *et al.* Deterministic transfer of two-dimensional materials by all-dry viscoelastic stamping. *2D Materials* **1**, 011002 (2014).

[111] Zomer, P. J., Guimarães, M. H., Brant, J. C., Tombros, N. & Wees, B. J. V. Fast pick up technique for high quality heterostructures of bilayer graphene and hexagonal boron nitride. *Applied Physics Letters* **105** (2014).

[112] Purdie, D. G. *et al.* Cleaning interfaces in layered materials heterostructures. *Nature Communications* **9**, 1–12 (2018).

[113] Blake, P. *et al.* Making graphene visible. *Applied Physics Letters* **91** (2007).

[114] Huang, Y. *et al.* Reliable exfoliation of large-area high-quality flakes of graphene and other two-dimensional materials. *ACS Nano* **9**, 10612–10620 (2015).

[115] Pizzocchero, F. *et al.* The hot pick-up technique for batch assembly of van der waals heterostructures. *Nature Communications 2016 7:1* **7**, 1–10 (2016).

[116] Uri, A. *et al.* Mapping the twist-angle disorder and landau levels in magic-angle graphene. *Nature* **581**, 47–52 (2020).

[117] Miyazaki, H. *et al.* Inter-layer screening length to electric field in thin graphite film. *Applied Physics Express* **1**, 0340071–0340073 (2008).

[118] Han, W., Maekawa, S. & Xie, X.-C. Spin current as a probe of quantum materials. *Nature Materials 2019 19:2* **19**, 139–152 (2019).

[119] Ribeiro-Palau, R. *et al.* Twistable electronics with dynamically rotatable heterostructures. *Science* **361**, 690–693 (2018).

[120] Kapfer, M. *et al.* Programming twist angle and strain profiles in 2d materials. *Science* **381**, 677–681 (2023).

[121] Haigh, S. J. *et al.* Cross-sectional imaging of individual layers and

buried interfaces of graphene-based heterostructures and superlattices. *Nature Materials* **11**, 764–767 (2012).

[122] Zhang, Y.-H., Po, C. & Senthil, T. Landau level degeneracy in twisted bilayer graphene: Role of symmetry breaking. *Physical Review B* **100**, 125104 (2019).

[123] Franssila, S. *Introduction to microfabrication* (Wiley-Blackwell, 2010), 2nd edition edn.

[124] Simonet, P. *et al.* Reactive-ion-etched graphene nanoribbons on a hexagonal boron nitride substrate. *Citation: Journal of Applied Physics* **117**, 33707 (2015).

[125] Shi, Z. *et al.* Patterning graphene with zigzag edges by self-aligned anisotropic etching. *Advanced Materials* **23**, 3061–3065 (2011).

[126] Principles of lock-in detection and the state of the art zurich instruments. *Zurich Instruments White Paper* 1–10 (2016).

[127] About lock-in amplifiers. *SRS Application Note* 1–9 (2011).

[128] User's manual bf-ld-series. *BlueFors* .

[129] Thalmann, M., Pernau, H.-F., Strunk, C., Scheer, E. & Pietsch, T. Comparison of cryogenic low-pass filters. *Review of scientific instruments* **88**, 114703 (2017).

[130] Ashcroft, N. W. & Mermin, N. D. *Solid State Physics*, vol. 9 (Brooks/Cole Cengage Learning, 1978).

[131] Xie, Y. *et al.* Spectroscopic signatures of many-body correlations in magic-angle twisted bilayer graphene. *Nature* **572**, 101–105 (2019).

[132] Sadiku, M. N. O. *Numerical Techniques in Electromagnetics* (CRC Press LLC, 2001), second edn.

[133] Nagel, J. R. Solving the generalized poisson equation using the finite-difference method (fdm) (2012).

[134] Young, D. Iterative methods for solving partial difference equations of elliptic type. *Transactions of the American Mathematical Society* **76**, 92 (1954).

[135] Rodan-Legrain, D. *et al.* Highly tunable junctions and non-local josephson effect in magic-angle graphene tunnelling devices. *Nature Nanotechnology* **16**, 769–775 (2021).

[136] Wang, Y. T., Hu, Y. C., Chu, W. C. & Chang, P. Z. The fringe-capacitance of etching holes for cmos-mems. *Micromachines* **6**, 1617–1628 (2015).

[137] Ribeiro-Palau, R. *et al.* High-quality electrostatically defined hall bars in monolayer graphene. *Nano Letters* **19**, 2583–2587 (2019).

[138] Icking, E. *et al.* Transport spectroscopy of ultraclean tunable band gaps in bilayer graphene. *Advanced Electronic Materials* **8** (2022).

[139] Tian, H. *et al.* Evidence for dirac flat band superconductivity enabled by quantum geometry. *Nature* **614**, 440–444 (2023).

[140] Berdyugin, A. I. *et al.* Out-of-equilibrium criticalities in graphene superlattices. *Science* **375**, 430–433 (2022).

[141] Heersche, H. B., Jarillo-Herrero, P., Oostinga, J. B., Vandersypen, L. M. & Morpurgo, A. F. Bipolar supercurrent in graphene. *Nature* **446**, 56–59 (2007).

[142] Lee, G.-H., Kim, S., Jhi, S.-H. & Lee, H.-J. Article ultimately short ballistic vertical graphene josephson junctions. *Nature Communications* (2015).

[143] Du, X., Skachko, I. & Andrei, E. Y. Josephson current and multiple andreev reflections in graphene sns junctions. *Physical Review B - Condensed Matter and Materials Physics* **77** (2008).

[144] Chen, C. Z. *et al.* Asymmetric josephson effect in inversion symmetry breaking topological materials. *Physical Review B* **98**, 75430 (2018).

[145] Hart, S. *et al.* Induced superconductivity in the quantum spin hall edge. *Nature Physics* **10**, 638–643 (2014).

[146] Dynes, R. C. & Fulton, T. A. Supercurrent density distribution in josephson junctions. *Physical Review B* **3**, 3015–3023 (1971).

[147] Xie, Y.-M., Efetov, D. K. & Law, K. T. φ_0-josephson junction in twisted bilayer graphene induced by a valley-polarized state. *Phys. Rev. Res.* **5**, 023029 (2023).

[148] Nuckolls, K. P. *et al.* Strongly correlated chern insulators in magic-angle twisted bilayer graphene. *Nature* **588**, 610–615 (2020).

[149] Polshyn, H. *et al.* Electrical switching of magnetic order in an orbital chern insulator. *Nature* **588**, 66–70 (2020).

[150] He, M. *et al.* Competing correlated states and abundant orbital magnetism in twisted monolayer-bilayer graphene. *Nature Communications* **12**, 1–8 (2021).

[151] He, W. Y., Goldhaber-Gordon, D. & Law, K. T. Giant orbital magnetoelectric effect and current-induced magnetization switching in twisted bilayer graphene. *Nature Communications* **11**, 1–8 (2020).

[152] Huang, C., Wei, N. & Macdonald, A. H. Current-driven magnetization reversal in orbital chern insulators. *Physical Review Letters* **126** (2021).

[153] Su, Y. & Lin, S. Z. Current-induced reversal of anomalous hall conductance in twisted bilayer graphene. *Physical Review Letters* **125** (2020).

[154] Gibertini, M., Koperski, M., Morpurgo, A. F. & Novoselov, K. S. Magnetic 2d materials and heterostructures. *Nature Nanotechnology* **14**, 408–419 (2019).

[155] Baek, B., Rippard, W. H., Benz, S. P., Russek, S. E. & Dresselhaus, P. D. Hybrid superconducting-magnetic memory device using competing order parameters. *Nature Communications* **5**, 1–6 (2014).

[156] Banerjee, N., Robinson, J. & Blamire, M. G. Reversible control of spin-polarized supercurrents in ferromagnetic josephson junctions. *Nature Communications* **5**, 1–6 (2020).

[157] Massarotti, D. *et al.* Macroscopic quantum tunnelling in spin filter ferromagnetic josephson junctions. *Nature Communications* **6**, 1–6 (2015).

[158] Tseng, C.-C. *et al.* Anomalous hall effect at half filling in twisted bilayer graphene. *Nature Physics* **18**, 1038–1042 (2022).

[159] Grover, S. *et al.* Chern mosaic and berry-curvature magnetism in magic-angle graphene. *Nature Physics* **18**, 885–892 (2022).

[160] Ando, F. *et al.* Observation of superconducting diode effect. *Nature* **584**, 373–376 (2020).

[161] Baumgartner, C. *et al.* Supercurrent rectification and magnetochiral effects in symmetric josephson junctions. *Nature Nanotechnology* **17**, 39–44 (2021).

[162] Wu, H. *et al.* The field-free josephson diode in a van der waals heterostructure. *Nature* **604**, 653–656 (2022).

[163] Wakatsuki, R. *et al.* Nonreciprocal charge transport in noncentrosymmetric superconductors. *Science Advances* **3**, e1602390 (2017).

[164] Lin, J. X. *et al.* Spin-orbit-driven ferromagnetism at half moiré filling in magic-angle twisted bilayer graphene. *Science* **375**, 437–441 (2022).

[165] Hu, J.-X., Sun, Z.-T., Xie, Y.-M. & Law, K. T. Josephson diode effect induced by valley polarization in twisted bilayer graphene. *Physical Review Letters* **130** (2023).

[166] Hesp, N. C. *et al.* Observation of interband collective excitations in twisted bilayer graphene. *Nature Physics* **17**, 1162–1168 (2021).

[167] Battista, G. D. *et al.* Revealing the thermal properties of superconducting magic-angle twisted bilayer graphene. *Nano Letters* **22**, 6465–6470 (2022).

[168] Gabor, N. M. *et al.* Hot carrier-assisted intrinsic photoresponse in graphene. *Science* **334**, 648–652 (2011).

[169] Massicotte, M., Soavi, G., Principi, A. & Tielrooij, K. J. Hot carriers in graphene – fundamentals and applications. *Nanoscale* **13**, 8376–8411 (2021).

[170] Urich, A., Unterrainer, K. & Mueller, T. Intrinsic response time of graphene photodetectors. *Nano Letters* **11**, 2804–2808 (2011).

[171] Tielrooij, K. J. *et al.* Generation of photovoltage in graphene on a femtosecond timescale through efficient carrier heating. *Nature Nanotechnology* **10**, 437–443 (2015).

[172] Jadidi, M. M. *et al.* Tunable ultrafast thermal relaxation in graphene measured by continuous-wave photomixing. *Phys. Rev. Lett.* **117** (2016).

[173] Aamir, M. A. *et al.* Ultrasensitive calorimetric measurements of the electronic heat capacity of graphene. *Nano Letters* **21**, 5330–5337 (2021).

[174] Bistritzer, R. & Macdonald, A. H. Electronic cooling in graphene. *Phys. Rev. Lett.* **102** (2009).

[175] Song, J. C. W., Reizer, M. Y. & Levitov, L. S. Disorder-assisted electron-phonon scattering and cooling pathways in graphene. *Phys. Rev. Lett.* **109** (2012).

[176] Koshino, M. & Son, Y.-W. Moire phonons in twisted bilayer graphene. *Physical Review B* **100**, 75416 (2019).

[177] Song, J. C., Rudner, M. S., Marcus, C. M. & Levitov, L. S. Hot carrier transport and photocurrent response in graphene. *Nano Letters* **11**, 4688–4692 (2011).

[178] Pogna, E. A. *et al.* Hot-carrier cooling in high-quality graphene is intrinsically limited by optical phonons. *ACS Nano* **15**, 11285–11295 (2021).

[179] de Vries, F. K. *et al.* Gate-defined josephson junctions in magic-angle twisted bilayer graphene. *Nature Nanotechnology* **16**, 760–763 (2021).

[180] Portolés, E. *et al.* A tunable monolithic squid in twisted bilayer graphene. *Nature Nanotechnology* **17**, 1159–1164 (2022).

[181] Iwakiri, S. *et al.* Tunable quantum interferometer for correlated moiré electrons. *Nature Communications* **15**, 1–8 (2024).

[182] Park, J. M., Cao, Y., Watanabe, K., Taniguchi, T. & Jarillo-Herrero, P. Tunable strongly coupled superconductivity in magic-angle twisted trilayer graphene. *Nature* **590**, 249–255 (2021).

[183] Hao, Z. *et al.* Electric field–tunable superconductivity in alternating-twist magic-angle trilayer graphene. *Science* **371**, 1133–1138 (2021).

[184] Shen, C. *et al.* Dirac spectroscopy of strongly correlated phases in twisted trilayer graphene. *Nature Materials* **22**, 316–321 (2022).

[185] Zhang, Y. *et al.* Promotion of superconductivity in magic-angle graphene multilayers. *Science* **377**, 1538–1543 (2022).

[186] Park, J. M. *et al.* Robust superconductivity in magic-angle multilayer graphene family. *Nature Materials* **21**, 877–883 (2022).

[187] Zhou, H. *et al.* Isospin magnetism and spin-polarized superconductivity in bernal bilayer graphene. *Science* **375**, 774–778 (2022).

[188] Zhang, Y. *et al.* Enhanced superconductivity in spin–orbit proximitized bilayer graphene. *Nature* **613**, 268–273 (2023).

[189] Oh, M. *et al.* Evidence for unconventional superconductivity in twisted bilayer graphene. *Nature* **600**, 240–245 (2021).

[190] Kim, H. *et al.* Evidence for unconventional superconductivity in twisted trilayer graphene. *Nature* **606**, 494–500 (2022).

[191] Chew, A., Wang, Y., Bernevig, B. A. & Song, Z.-D. Higher-order topological superconductivity in twisted bilayer graphene. *Physical Review B* **107**, 94512 (2023).

[192] Lake, E., Patri, A. S. & Senthil, T. Pairing symmetry of twisted bilayer graphene: A phenomenological synthesis. *Physical Review B* **106**, 104506 (2022).

[193] Julku, A., Peltonen, T. J., Liang, L., Heikkilä, T. T. & Törmä, P. Superfluid weight and berezinskii-kosterlitz-thouless transition temperature of twisted bilayer graphene. *Physical Review B* **101**, 060505 (2020).

[194] Yu, J., Ciccarino, C. J., Bianco, R., Narang, P. & Bernevig, B. A. Nontrivial quantum geometry and the strength of electron-phonon coupling. *Preprint: arXiv:2305.02340* (2023).

[195] Chen, S. A. & Law, K. T. Towards a ginzburg-landau theory of the quantum geometric effect in superconductors. *Preprint: arXiv:2303.15504* (2023).

[196] Wang, L. *et al.* Correlated electronic phases in twisted bilayer transition metal dichalcogenides. *Nature Materials* **19**, 861–866 (2020).

[197] Inbar, A. *et al.* The quantum twisting microscope. *Nature* **614**, 682–687 (2023).

[198] Sinko, M. R. *et al.* Superconducting contact and quantum interference between two-dimensional van der waals and three-dimensional conventional superconductors. *Physical Review Materials* **5**, 014001 (2021).

[199] Masubuchi, S., Ono, M., Yoshida, K., Hirakawa, K. & MacHida, T. Fabrication of graphene nanoribbon by local anodic oxidation lithography using atomic force microscope. *Applied Physics Letters* **94** (2009).

[200] Weng, L., Zhang, L., Chen, Y. P. & Rokhinson, L. P. Atomic force microscope local oxidation nanolithography of graphene. *Applied Physics Letters* **93**, 93107 (2008).

[201] Cohen, L. A. *et al.* Universal chiral luttinger liquid behavior in a graphene fractional quantum hall point contact. *Science* **382**, 542–547 (2023).

[202] Xie, Y.-M., Étienne Lantagne-Hurtubise, Young, A. F., Nadj-Perge,

S. & Alicea, J. Gate-defined topological josephson junctions in bernal bilayer graphene. *Physical Review Letters* **131** (2023).

[203] Lau, C. N., Bockrath, M. W., Mak, K. F. & Zhang, F. Reproducibility in the fabrication and physics of moiré materials. *Nature* **602**, 41–50 (2022).

[204] Masubuchi, S. *et al.* Autonomous robotic searching and assembly of two-dimensional crystals to build van der waals superlattices. *Nature Communications* **9**, 1–12 (2018).

[205] Mannix, A. J. *et al.* Robotic four-dimensional pixel assembly of van der waals solids. *Nature Nanotechnology* 1–6 (2022).

[206] Wang, W. *et al.* Clean assembly of van der waals heterostructures using silicon nitride membranes. *Nature Electronics* **6**, 981–990 (2023).